

---

# Preparation and Investigation of Highly Charged Ions in a Penning Trap for the Determination of Atomic Magnetic Moments

---

**Präparation und Untersuchung von hochgeladenen Ionen in einer Penning-Falle  
zur Bestimmung atomarer magnetischer Momente**

Dissertation approved by the Fachbereich Physik of the Technische Universität  
Darmstadt in fulfillment of the requirements for the degree of Doctor of Natural  
Sciences (Dr. rer. nat.) by Dipl.-Phys. Marco Wiesel from Neustadt an der Weinstraße  
June 2017 – Darmstadt – D 17

---

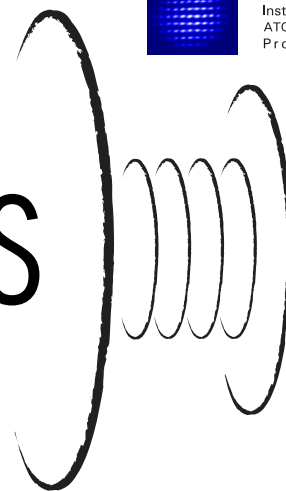


TECHNISCHE  
UNIVERSITÄT  
DARMSTADT



Fachbereich Physik  
Institut für Angewandte Physik  
ATOME - PHOTONEN - QUANTEN  
Prof. Dr. Gerhard Birkel

ARTEMIS





# Preparation and Investigation of Highly Charged Ions in a Penning Trap for the Determination of Atomic Magnetic Moments

Dissertation  
approved by the Fachbereich Physik  
of the Technische Universität Darmstadt  
in fulfillment of the requirements for the degree of  
Doctor of Natural Sciences (Dr. rer. nat.)

by Dipl.-Phys. Marco Wiesel  
from Neustadt an der Weinstraße

1. Referee: Prof. Dr. rer. nat. Gerhard Birkl  
2. Referee: Privatdozent Dr. rer. nat. Wolfgang Quint

Submission date: 18.04.2017  
Examination date: 24.05.2017

Darmstadt 2017  
D 17



---

Title: The logo of ARTEMIS – AsymmetRic Trap for the measurement of Electron Magnetic moments in IonS.

Bitte zitieren Sie dieses Dokument als:  
URN: urn:nbn:de:tuda-tuprints-62803  
URL: <http://tuprints.ulb.tu-darmstadt.de/id/eprint/6280>

Dieses Dokument wird bereitgestellt von tuprints,  
E-Publishing-Service der TU Darmstadt  
<http://tuprints.ulb.tu-darmstadt.de>  
[tuprints@ulb.tu-darmstadt.de](mailto:tuprints@ulb.tu-darmstadt.de)



Die Veröffentlichung steht unter folgender Creative Commons Lizenz:  
Namensnennung – Keine kommerzielle Nutzung – Keine Bearbeitung 4.0 International  
<https://creativecommons.org/licenses/by-nc-nd/4.0/>

---



---

---

## Abstract

---

The ARTEMIS experiment aims at measuring magnetic moments of electrons bound in highly charged ions that are stored in a Penning trap. It will provide access to effects of quantum electrodynamics (QED) in the extreme fields close to an ionic nucleus. Additionally, due to the high magnetic field of the Penning trap, higher-order Zeeman effects can be examined and therefore provide a different access to the theory of QED.

In this work, a cooled cloud of boron-like argon ions,  $\text{Ar}^{13+}$ , was prepared in the creation part of a double Penning trap held at cryogenic temperatures. Systematic measurements were carried out in order to investigate the creation trap and its specific parameters to generate a suitable ion cloud. This ion cloud consisted after further charge breeding of different charge states. It was then cooled and parts of it were excited by the SWIFT-technique and, in combination with fast potential-switching, all ion species except  $\text{Ar}^{13+}$  were removed. Together with the successful transport of an ion cloud from the creation trap into the spectroscopy trap all concepts necessary in order to prepare an  $\text{Ar}^{13+}$  ion cloud for performing laser-microwave double-resonance spectroscopy have been implemented. Additionally, a measurement of the modified cyclotron frequency in the creation trap was carried out by exciting the ions radially while detecting their axial motional frequency. Thus, a value for the magnetic field strength in the creation trap with a 5 parts-per-million accuracy was achieved.

A system for irradiating microwaves with a frequency of 65 gigahertz onto the position of the ions was developed, characterized and implemented into the apparatus. It was conceptualized for meeting the challenging conditions of the experiment, such as the high magnetic field, the cryogenic temperatures and the difficult geometry.

A novel concept of employing an indium tin oxide (ITO)-coated window as an endcap for a closed Penning trap was implemented in the spectroscopy trap and its functionality was proven. The window improves the fluorescence photon efficiency by at least 17% and increases the planarity over the previously used mesh and therefore decreases the trap anharmonicities. Additionally, a test of the ITO-coated window proved its applicability as a Faraday cup for detecting highly charged ions.

During this thesis, experimental studies of the various components of ARTEMIS have been carried out and the full apparatus was assembled and put into operation. The focus of this work was the design of the mechanical parts and their assembly, such as the cryogenic concept and the vibrational decoupling.

In the future, ARTEMIS will be connected to the HITRAP beamline at GSI, so heaviest highly charged ions can be examined. During this work, a fast opening valve, that separates the trap vacuum from the beamline vacuum, was assembled and initial tests were conducted.

---

## Zusammenfassung

---

Das ARTEMIS-Experiment speichert hochgeladene Ionen in einer Penning-Falle und zielt dabei auf die Messung der magnetischen Momente der darin gebundenen Elektronen ab. Dies ermöglicht den Zugang zu den Effekten der Quantenelektrodynamik (QED) unter den extremen Bedingungen in der Nähe des Ionenkerns. Aufgrund des starken magnetischen Feldes der Penning-Falle kann außerdem der Zeeman-Effekt höherer Ordnung untersucht werden, was einen alternativen Zugang zur QED darstellt.

Im Rahmen dieser Arbeit wurde eine gekühlte Wolke borähnlicher Argonionen,  $\text{Ar}^{13+}$ , im Erzeugungsteil einer kryogenen Doppel-Penningfalle präpariert. Es wurden Messungen durchgeführt, um die Erzeugungsfalle und ihre spezifischen Parameter zu untersuchen, sodass eine geeignete Ionenwolke generiert werden konnte. Diese Wolke, welche sich nach dem Ladungsbrüten aus unterschiedlichen Ladungszuständen zusammensetzt, wurde gekühlt und Teile davon mittels der SWIFT-Technik angeregt, um hiernach durch schnelles Schalten des Fallenpotentials alle ungewollten Ionenspezies außer  $\text{Ar}^{13+}$  zu entfernen. Gemeinsam mit dem erfolgreichen Transport einer Ionenwolke von der Erzeugungs- in die Spektroskopiefalle wurden damit alle nötigen Konzepte zur Präparation einer  $\text{Ar}^{13+}$ -Wolke implementiert, um die Laser-Mikrowellen-Doppelresonanzspektroskopie durchzuführen. Außerdem wurde in der Erzeugungsfalle eine Messung der modifizierten Zyklotronfrequenz durch radiale Anregung und Detektion der axialen Bewegungsfrequenz durchgeführt und damit ein Wert für die Magnetfeldstärke mit einer Genauigkeit im ppm-Bereich ermittelt.

Um die Ionen mit Mikrowellen mit einer Frequenz von 65 Gigahertz zu bestrahlen, wurde ein Mikrowellensystem entwickelt, charakterisiert und ins Experiment eingebaut. Es galt dabei, die schwierigen Bedingungen des Experiments (starkes Magnetfeld, kryogene Temperaturen und die schwierige Geometrie) zu erfüllen.

Ein neues Konzept, das ein Indiumzinnoxid (ITO)-beschichtetes Fenster als Endkappe einer geschlossenen Penningfalle nutzt, wurde erfolgreich umgesetzt. Mit diesem Fenster konnte die Fluoreszenzphotoneneffizienz gegenüber des zuvor verwendeten Netzes um 17% gesteigert und durch bessere Planarität die Anharmonizitäten der Falle verringert werden. Zudem wurde das Fenster auch in seiner Tauglichkeit als Faraday-Detektor zur Detektion hochgeladener Ionen getestet.

Während dieser Arbeit wurden experimentelle Studien zu den einzelnen Komponenten durchgeführt und schließlich das komplette Experiment zusammengebaut und in Betrieb genommen. Der Schwerpunkt dieser Arbeit lag dabei im Design der mechanischen Komponenten und deren Installation, erwähnt seien hierbei das Konzept der kryotechnischen Umsetzung und die Vibrationsentkopplung.

In Zukunft soll das Experiment an die HITRAP-Strahllinie der GSI angebunden werden, um höchstgeladene Ionen untersuchen zu können. Für dieses Ziel wurden im Rahmen dieser Arbeit ein schnellöffnendes Ventil, das das Fallenvakuum vom Stahllinienvakuum trennen soll, zusammengebaut und erste Tests durchgeführt.



---

# Contents

<b>1</b>	<b>Motivation and Introduction</b>	<b>1</b>
<b>2</b>	<b>The <math>g</math>-Factor as a Test for Quantum Electrodynamics</b>	<b>5</b>
2.1	The $g$ -Factor of the Free Electron . . . . .	6
2.2	The $g$ -Factor of the Bound Electron . . . . .	7
2.2.1	Bound-State QED . . . . .	8
2.2.2	Ar <sup>13+</sup> as a First Candidate . . . . .	11
2.3	Double-Resonance Spectroscopy . . . . .	13
2.3.1	Measurement Scheme . . . . .	13
2.3.2	Higher-Order Zeeman Effect . . . . .	14
<b>3</b>	<b>The Penning Trap</b>	<b>15</b>
3.1	The Principal Design . . . . .	15
3.2	Ion Motion . . . . .	17
3.2.1	Frequency Shifts . . . . .	20
3.2.2	Quantized Motions . . . . .	21
3.3	Resonant Detection Circuits . . . . .	22
<b>4</b>	<b>Investigation of Argon Ions in the ARTEMIS Apparatus</b>	<b>25</b>
4.1	Magnet in the Wooden Tower . . . . .	27
4.2	Cryogenic Setup . . . . .	29
4.3	Detection Housing and Trap Chamber . . . . .	30
4.3.1	The Non-Destructive Ion-Motion Detection Systems . . . . .	32
4.3.2	Cyclotron Resonator (CRES) . . . . .	37
4.3.3	Laser and the Optical Detection System . . . . .	43
4.4	The 65 GHz Microwave System . . . . .	45
4.4.1	Previous Considerations . . . . .	46
4.4.2	Hybrid Design . . . . .	47
4.4.3	Microwave Source . . . . .	47
4.4.4	Transmission Lines and Waveguide Flanges . . . . .	50
4.4.5	Adapter: Waveguide-to-Coax . . . . .	53
4.4.6	The Vacuum Feedthrough . . . . .	54
4.4.7	Quadrupler . . . . .	55
4.4.8	Amplifier . . . . .	57
4.4.9	Attenuator . . . . .	58
4.4.10	Horn Antenna . . . . .	58

4.4.11	Power Diode . . . . .	60
4.4.12	Tabletop Measurements . . . . .	60
4.5	The Penning Trap . . . . .	63
4.5.1	Indium Tin Oxide-Coated Window . . . . .	67
4.5.2	Mini Electron Beam Ion Source (EBIS), Cryovalve and Gas In- jection . . . . .	69
4.6	Fast Opening Valve . . . . .	73
<b>5</b>	<b>Preparation of an Ion Cloud and Measurements</b>	<b>75</b>
5.1	Data Acquisition . . . . .	76
5.1.1	Introduction to the Measurement Labview System . . . . .	76
5.1.2	Spectrum Read Out . . . . .	77
5.2	Ion Creation . . . . .	80
5.3	Ion Cooling . . . . .	84
5.4	Ions in the Creation Trap . . . . .	90
5.4.1	Residual Gas Pressure Estimation . . . . .	90
5.4.2	Higher-Order Motion Seen by the Detector . . . . .	91
5.4.3	Ions in the Trap with C12 as a Ring Electrode . . . . .	93
5.5	Ion Transport . . . . .	95
5.6	Ions in the Spectroscopy Trap . . . . .	97
5.7	Cyclotron Frequency . . . . .	97
5.8	SWIFT . . . . .	99
<b>6</b>	<b>Summary, Improvements and Outlook</b>	<b>105</b>
<b>A</b>	<b>Appendix</b>	<b>109</b>
A.1	Damping of Cryocooler Vibrations . . . . .	109
A.2	ARTEMIS Wiring . . . . .	110
A.3	Timeline of ARTEMIS . . . . .	114
<b>B</b>	<b>List of Abbreviations</b>	<b>115</b>
	<b>Bibliography</b>	<b>117</b>
	<b>Curriculum Vitae</b>	<b>124</b>
	<b>Erklärung zur Dissertation</b>	<b>125</b>

---

---

# List of Figures

2.1	Original Feynman-diagram for electron-electron interaction. . . . .	5
2.2	Feynman-diagrams contributing to the free electron magnetic moment. . . . .	7
2.3	Schematic: Precession of a bound electron around an external magnetic field due to its magnetic moment. . . . .	8
2.4	Feynman diagrams for calculating the BS-QED. . . . .	9
2.5	Grotrian-diagram for the $^2P_{1/2} - ^2P_{3/2}$ transition in $Ar^{13+}$ . . . . .	11
2.6	Theoretical contributions to the $g$ -factor of boron-like argon. . . . .	12
2.7	Example to explain the double-resonance spectroscopy in $Ar^{13+}$ . . . . .	13
2.8	Fine-structure and Zeeman energy splitting for $Ar^{13+}$ . . . . .	14
3.1	Cross-section of a Penning trap with hyperbolically shaped electrodes. . . . .	16
3.2	Schematic of the three basic cylindrical Penning trap concepts. . . . .	17
3.3	Calculated trajectories of the three independent ion motions for a single $Ar^{13+}$ ion in the creation trap. . . . .	19
3.4	Level scheme for the energy states of the three ion motions. . . . .	22
3.5	Schematic of the resonant ion-motion-frequency detection. . . . .	23
4.1	Overview of the GSI accelerator facility. . . . .	25
4.2	CAD drawings of the ARTEMIS experiment. . . . .	26
4.3	Magnetic field of the superconducting magnet near the field center. . . . .	27
4.4	Photographs of the aluminium hoist on top of the tower. . . . .	28
4.5	Photograph of the stranded copper wires. . . . .	29
4.6	Photograph of the electronics and detection housing. . . . .	31
4.7	Photographs of the three resonators. . . . .	34
4.8	Thermalization of a superconducting resonator. . . . .	35
4.9	Behavior of a superconducting resonator in various magnetic field strengths. . . . .	35
4.10	Resonance spectra of the two axial resonators. . . . .	37
4.11	Cyclotron resonator resonance curve with different varactor diode biases. . . . .	38
4.12	Equivalent Circuit of the varactor diode test board. . . . .	40
4.13	Varactor diode measurements at cryogenic temperatures with strong magnetic fields (1). . . . .	41
4.14	Varactor diode measurements at cryogenic temperatures with strong magnetic fields (2). . . . .	42
4.15	Locking scheme of the laser system and photograph of the optical system. . . . .	43
4.16	Scheme of the laser system and the optical coupling into the trap. . . . .	44

4.17 Overview of the hybrid design microwave system for a frequency of 65 GHz. . . . .	48
4.18 Phase-noise measurement and carrier frequency of the microwave source. . . . .	49
4.19 Schematic of the TE and TEM mode. . . . .	50
4.20 Technical drawing of a WR-12 flange. . . . .	52
4.21 Cross-section of the two cryogenic coaxial cables. . . . .	53
4.22 Schematic of the coax-to-waveguide adapter. . . . .	54
4.23 Schematic of a microwave isolator and photograph of the quadrupler. . . . .	56
4.24 Photograph of the horn antenna and typical horn antenna gain. . . . .	59
4.25 Frequency dependence of the transmitted power for the complete hybrid-design setup. . . . .	62
4.26 Phase-noise measurement of the 65 GHz carrier frequency. . . . .	62
4.27 Photograph and CAD drawing of the double Penning trap. . . . .	64
4.28 Schematic of the different trap designs. . . . .	65
4.29 Schematic potential curve explaining the anti-trap and schematic of the spectroscopy trap. . . . .	66
4.30 Photograph of the ITO-coated window and its optical transmission curve. . . . .	68
4.31 Temperature dependence of the resistance of an ITO-coated window and the ITO-endcap as a Faraday cup. . . . .	69
4.32 Scheme of ion creation by electron beam impact. . . . .	71
4.33 FEP current versus accelerator voltage for different FEP voltages at different times. . . . .	71
4.34 Schematic of the cryovalve. . . . .	72
4.35 Fast opening valve CAD drawings. . . . .	74
5.1 Example of a block diagram LABVIEW routine. . . . .	77
5.2 The three data acquisition schmemes. . . . .	78
5.3 Comparison of the different data taking methods. . . . .	80
5.4 Charge-to-mass spectra of ion clouds created with different parameters. . . . .	83
5.5 Tungsten ions created in the creation trap. . . . .	84
5.6 Calculated effective electrode distance. . . . .	86
5.7 Consecutive cooling ramps, single ramps shown. . . . .	87
5.8 Consecutive cooling ramps, investigation of the total signal strength and the frequency shifts. . . . .	88
5.9 Axial sideband magnetron centering. . . . .	89
5.10 Long term trapping of highly charged ions. . . . .	91
5.11 Higher order ion motions seen by the detector. . . . .	92
5.12 Scheme of the three Penning traps in the CT. . . . .	93
5.13 Schematic of the concentrate procedure and investigation on ions in the trap C12. . . . .	94
5.14 Scheme of one step of the transport of ions between the electrodes. . . . .	95
5.15 Consecutive transports of an ion cloud. . . . .	96

---

5.16 Ion signal in the spectroscopy trap. . . . .	97
5.17 Example measurement of the modified cyclotron frequency. . . . .	98
5.18 Analysis of the excitation method to measure the modified cyclotron frequency. . . . .	99
5.19 SWIFT broadband excitation in the modified cyclotron domain. . . . .	100
5.20 Schematic of the SWIFT procedure with fast switching. . . . .	101
5.21 Measurement to investigate the switching time. . . . .	102
5.22 SWIFT cleaning technique to get a pure Ar <sup>13+</sup> ion cloud. . . . .	103
A.1 Transmissibility plotted to study vibration damping. . . . .	110
A.2 Room-temperature filterboards and HV feedthrough flange. . . . .	110
A.3 Wire diagram 1 – Trap wiring. . . . .	111
A.4 Wire diagram 2 – Overall setup. . . . .	112
A.5 ARTEMIS timeline of the last four years. . . . .	114



---

# List of Tables

3.1	Calculated frequency and amplitude values for creation and spectroscopy trap for $\text{Ar}^{13+}$ . . . . .	19
4.1	Properties of all three resonators. . . . .	33
4.2	VSWR values and their related transmission power losses. . . . .	51
4.3	Specifications of a standard WR-12 waveguide. . . . .	52
4.4	Specifications of the waveguide-to-coax adapter. . . . .	54
4.5	Specifications of the vacuum feedthrough. . . . .	55
4.6	Specifications of the quadrupler. . . . .	57
4.7	Specifications of the power amplifier. . . . .	57
4.8	Specifications of the attenuator. . . . .	58
4.9	Specifications of the horn antenna. . . . .	58
4.10	Loss in different materials for microwaves at a frequency of 65 GHz. . .	59
4.11	Specifications of the power diode. . . . .	60
4.12	Theoretical and measured losses for the different parts of the hybrid design. . . . .	61
4.13	Trap geometries for spectroscopy trap and creation trap. . . . .	63
4.14	Trap parameters for spectroscopy trap and creation trap. . . . .	67
5.1	Ionization energies of argon. . . . .	81
5.2	Ionization energies of tungsten. . . . .	84





---

# 1 Motivation and Introduction

*“Protons give an atom its identity, electrons its personality.”*

– Bill Bryson, *A Short History of Nearly Everything*

The electron is one of the fundamental particles in physics – discovered in 1897 by J. J. Thomson, it is still an important subject of modern science. Due to its fundamental nature, it links to many significant constants in physics. Thus, measuring them with high precision provides a powerful tool to test the standard model of physics. One of the most precise measurements for an elementary particle is performed with an electron by measuring its gyromagnetic ratio (the so-called  $g$ -factor). It is the dimensionless constant  $g_s$  linking the electron’s magnetic moment  $\vec{\mu}_s$  in terms of the Bohr magneton  $\mu_B$  to its spin  $\vec{s}$ :

$$\vec{\mu}_s = -g_s \mu_B \frac{\vec{s}}{\hbar} \quad \text{with} \quad \mu_B = \frac{e \hbar}{2 m_e}, \quad (1.1)$$

where  $e$  is the elementary charge of the electron,  $m_e$  its mass and  $\hbar = \frac{h}{2\pi}$  the reduced Planck constant.

Dirac predicted in 1928 the value of the  $g$ -factor to be exactly 2 by combining quantum mechanics with special relativity. However, in 1947 Kusch and Foley measured small deviations [1, 2]. The discovery of the Lamb shift [3] together with this anomalous magnetic moment served as a stimulus to the development of the (relativistic) quantum field theory of electrodynamics (QED) [4]. Schwinger was the first to calculate this anomaly in the framework of QED theory. In 1965 Richard Feynman, Shin’ichirō Tomonaga, and Julian Schwinger received the Nobel prize ‘for their fundamental work in quantum electrodynamics (QED), with deep-ploughing consequences for the physics of elementary particles’ [5].

In the nineteen-eighties, Dehmelt *et al.* were able to measure the magnetic moment of the free electron with a relative precision of  $4 \times 10^{-12}$  [6]. This experiment was performed in a Penning trap, an apparatus in which a charged particle is confined radially by a magnetic field and axially by an electric quadrupole field. The motion of a charged particle in such a trap can be cooled in order to perform precision spectroscopy. For these high-precision experiments on ‘geonium’<sup>1</sup>, Dehmelt was awarded the Nobel prize for physics in 1989. Progress in measuring techniques and advances in trap designs made it possible to reach even higher precision for the free

---

<sup>1</sup> Geonium is a term introduced by Dehmelt, describing a quasi-atomic system of a single electron ‘bound’ to earth due to the Penning trap.

electron  $g$ -factor. To this day the most precise experimental result has been obtained at Harvard University with an uncertainty of 0.56 parts-per-trillion ( $5.6 \times 10^{-13}$ , ppt) [7], when at the same time QED calculations yielded a value with almost identical precision:

$$g_{\text{exp}} = 2.002\,319\,304\,361\,46(56)$$

$$g_{\text{th}} = 2.002\,319\,304\,363\,56(154)$$

This makes QED one of the best tested theories in science. The success of this theory since then continues unabated, its reliability has been tested many times [8] and by assuming the theoretical predictions to be valid, together with the measurement of  $g$ , a new value for the fine-structure constant  $\alpha^{-1} = 137.035\,999\,173(35)$  can be extracted [9].

An extension to ordinary quantum electrodynamics is the theory of bound-state QED (BS-QED), capable of describing electrons bound to an atomic nucleus. Experiments in the framework of BS-QED give rise to new effects and test QED on completely different scales. As an example, a recent breakthrough of BS-QED was the new determination of the electron mass: a single  $^{12}\text{C}^{5+}$  ion was stored in a Penning trap, by comparing the precession frequency (in the magnetic field) of the remaining electron bound directly to the bare carbon nucleus with the ion's cyclotron frequency and taking the calculations from BS-QED, the electron mass  $m_e$  was determined in atomic mass units to be  $m_e = 0.000\,548\,579\,909\,067(14)(9)(2)\text{u}$  [10], hence, providing the most precise value of the electron mass.

The theoretical predictions of QED can only be used as an input parameter when the theory is still valid on these high levels of accuracy. Therefore, BS-QED has to be tested even in the most extreme conditions, e.g. in highly charged ions (HCI) [11]. By removing almost all electrons from a heavy atom, an ion with a high charge state is produced. The remaining electrons are exposed to field strengths that cannot be produced in other experiments. As an example, for the  $1S_{1/2}$  electron in hydrogen-like<sup>2</sup> uranium the expectation value for the electrical field strength amounts to  $2 \times 10^{18}$  V/m [12], four orders of magnitude higher than the pulse of a high-power laser.

Since the 'GSI Helmholtzzentrum für Schwerionenforschung' in Darmstadt has access to a unique accelerator facility capable of accelerating almost any kind of ion, an experiment was built to test BS-QED in highly charged ions. Currently the 'Heavy Highly Charged Ion Trap' facility (HITRAP) is being commissioned, which, when finished, will be able to slow down ions so they can be passed to high-precision Penning trap experiments [13]. One of these experiments is the 'AsymmetRiC Trap for the measurement of Electron Magnetic moments in IonS', short: ARTEMIS, an experimental setup for precision laser and microwave spectroscopy of trapped highly charged ions. The first experiment aimed for is the measurement of the  $g$ -factor of an electron

<sup>2</sup> Hydrogen-like refers to ions where all but one electron are removed from the atom, for example  $\text{Bi}^{82+}$  or  $\text{U}^{91+}$ .

---

when bound in  $^{40}\text{Ar}^{13+}$ . This has already been measured at the Heidelberg electron beam ion trap (EBIT) at the ‘MPI for nuclear physics’. A 1.5 parts-per-thousand accuracy was reached [14]. ARTEMIS aims at achieving a one-million-fold improvement to the parts-per-billion level [15]. With this precision, few-electron QED calculations can be tested with high sensitivity and higher-order magnetic field shifts in the Zeeman-sublevels can be measured [16]. ARTEMIS produces boron-like  $\text{Ar}^{13+}$  ions in an electron beam ion source (EBIS) inside the creation part of a double Penning trap. The ions are then moved into the so-called spectroscopy trap for further investigation. The  $g$ -factor of the bound electron can then be measured via the technique of double-resonance spectroscopy [17]: a closed cycle between the fine-structure levels  $2^2\text{P}_{1/2} - 2^2\text{P}_{3/2}$  is driven by a laser, whereas microwaves are tuned to get into resonance with the Zeeman transition. In combination with a measurement of the motional frequencies of the trapped ions, the bound-electron  $g$ -factor can be obtained.

This thesis was written during the assembly, commissioning, and first improvement phase of ARTEMIS. Together with the thesis of D. Lindenfels [18], it represents a near-complete description of the whole apparatus. It is organized in three major parts: the theory, the apparatus and its improvements, and measurements and preparation of an ion cloud. Starting with chapter 2, the theory of quantum electrodynamics is explained, first, by comparison between the theoretical and experimental determination of the magnetic moment of the free electron (Sec. 2.1) and then, in section 2.2, the even more complex theory of bound-state quantum electrodynamics is introduced. Afterwards, section 2.3 explains how the  $g$ -factor of a bound electron and higher-order Zeeman shifts in highly charged ions can be measured via double-resonance spectroscopy.

The second theory part, chapter 3, outlines the basics of the most important tool used in the framework of ARTEMIS: the Penning trap. The three motions, that a charged particle performs, are explained and for the first candidate,  $\text{Ar}^{13+}$ , some exemplary parameters are given (Sec. 3.2). Since in ARTEMIS not only a single particle is investigated, but a cloud of ions, and since it is not an ideal Penning trap, additional shifts of the ion motional frequencies have to be taken into account (Sec. 3.2.1).

The most comprehensive fraction of this thesis is chapter 4. Here, most parts of the experimental setup are explained in great detail and preliminary measurements and improvements that were carried out during this thesis are given. First, after an introduction on the environment around ARTEMIS, the cryogenic setup (Sec. 4.2) is depicted, followed by the housing of the electronics and the various detection devices in section 4.3. The non-destructive ion motion detectors, the resonators, are explained in section 4.3.1, with a focus on the measurements of the resonator-frequency shifting varactor diode in high magnetic field strengths and cryogenic temperatures. Section 4.4 is dedicated to the microwave system for generating a frequency of 65 gigahertz and describes the development of the hybrid-design and the

---

test-measurements that were conducted in a tabletop-experiment. Afterwards, the double Penning trap, the heart of ARTEMIS, is presented in section 4.5. An improvement was implemented by using an indium tin oxide coated, conductive window as an endcap (Sec. 4.5.1). Finally, in section 4.5.2, the in-trap production of medium highly charged ions, such as argon, is explained.

Chapter 5 reports about the measurements that were performed in the 2016 measurement time. It starts with an overview of the data acquisition by the LABVIEW experiment-control software and the charge-to-mass spectrum as the most common technique of acquiring data (Sec. 5.1). The ion creation is introduced in section 5.2 and different types of created ion clouds with their corresponding parameter sets are depicted. Cooling of axial motional frequencies is investigated, and also the concept and application of magnetron centering is presented (Sec. 5.3). Together with some peculiarities of the creation trap, a value for the vacuum condition in the Penning trap is estimated in section 5.4 and additionally, the magnetic field in the creation trap is indirectly measured (Sec. 5.7). After describing some investigations that were carried out on the ion transport (Sec. 5.5), the successful transport of an argon ion cloud is reported in section 5.6. The chapter closes with the preparation of a cool, pure  $\text{Ar}^{13+}$  ion cloud by the SWIFT-technique which is used to remove all unwanted species from the trap (Sec. 5.8).

Finally, a summary with proposed improvements and an outlook for the future of the ARTEMIS experiment is given in chapter 6.

## 2 The $g$ -Factor as a Test for Quantum Electrodynamics

One of the fathers of QED, Richard Feynman, invented pictorial representations in the form of diagrams for the mathematical expressions that describe QED effects in the framework of a perturbative expansion in the fine-structure constant  $\alpha$ . These diagrams follow specific rules and with their help complex processes can be illustrated. Figure 2.1 shows one of his first ‘Feynman-diagrams’ from a publication in 1949 [19]. Although they are nowadays drawn in a more stylized way, their basic features are still the same. The figure shows the process of electron-electron interaction (the time elapses from bottom to top): the right electron, drawn as a straight line, emits a virtual photon, shown as a wavy line that is absorbed by the other electron – the two electrons repel each other through Coulomb interaction. Since figure 2.1 contains two vertices (the two points of emission and absorption are called vertices) and each vertex contributes with  $\sqrt{\alpha}$ . This diagram represents the first order in  $\alpha$ . With the help of Feynman-diagrams the basic processes occurring in QED will be demonstrated, first, in the case of the  $g$ -factor of the free electron and then in the framework of BS-QED for an electron in a many-electron system, bound to a nucleus. Nevertheless it should be noted that this is just a brief phenomenological view, much more details can be found in [20, 21].

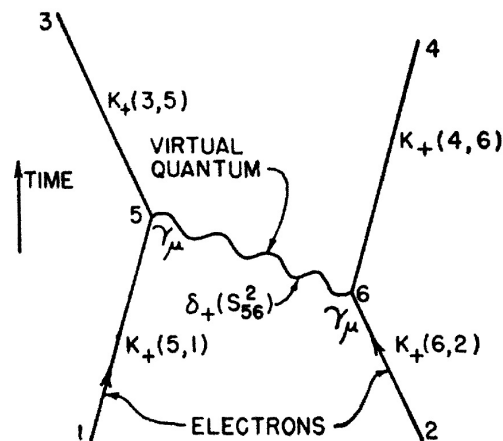


**Figure 2.1:** One of the first ‘Feynman-diagrams’ published by Richard Feynman in 1949, depicting electron-electron interaction. Picture taken from [19]: The time elapses from the bottom to the top. Electrons are drawn as straight lines, photons as wavy lines. The right electron emits a virtual photon that is absorbed by the other electron, thus the electrons repel each other by Coulomb interaction. The diagram contains two vertices, at position ‘5’ and ‘6’, therefore it represents the first order term in the expansion in  $\alpha$ .

---

## 2.1 The $g$ -Factor of the Free Electron

---

The electron magnetic moment in terms of the Bohr magneton  $\mu_s/\mu_B = -g_s/2$  can be expressed by

$$g_s/2 = 1 + a_{\text{QED}}(\alpha) + a_{\text{hadronic}} + a_{\text{weak}}, \quad (2.1)$$

where the leading term 1 comes directly from Dirac's equation;  $a_{\text{QED}}$  results from QED calculations, adding roughly 0.1 %;  $a_{\text{hadronic}}$  comes from the interaction of the electron with hadron-antihadron pairs, giving a 2 ppt contribution;  $a_{\text{weak}}$  takes into account Feynman-diagrams containing at least one virtual W-boson, Z-boson, or Higgs particle, its contribution is even smaller and can be neglected for the precisions achieved [21]. In order to calculate  $a_{\text{QED}}$ , an expansion in orders of the fine-structure constant  $\alpha = e^2/(4\pi\epsilon_0\hbar c) \approx 1/137$  ( $e$  is the elementary electric charge,  $\epsilon_0$  the vacuum permittivity and  $c$  the speed of light) is derived:

$$a_{\text{QED}}(\alpha) = C_2\left(\frac{\alpha}{\pi}\right) + C_4\left(\frac{\alpha}{\pi}\right)^2 + C_6\left(\frac{\alpha}{\pi}\right)^3 + C_8\left(\frac{\alpha}{\pi}\right)^4 + C_{10}\left(\frac{\alpha}{\pi}\right)^5 + \dots \quad (2.2)$$

In this series, since  $\alpha \approx 1/137$ , the contribution of the summands decreases with increasing order. These summands correspond to different orders of Feynman-diagrams. The first coefficient  $C_2$  was calculated by Schwinger in 1948 to be 1/2. The corresponding diagram for this first order can be found in figure 2.2, showing an electron moving through time. Please note that in all following Feynman-diagrams the time axis points from left to right. After emitting a virtual photon, an interaction with an external magnetic field happens, then the virtual photon is reabsorbed. This effect is called vertex-correction and is the only process possible in first order of  $\alpha$  (therefore the only process with only two vertices). The dashed line always shows the interaction of the electron with an external (magnetic) field (of the Penning trap in this case).

For the next higher-order coefficient  $C_4$ , all diagrams with four vertices need to be computed. Figure 2.2 shows the respective seven diagrams. They can be divided into vertex-correction/self-energy and vacuum polarization. It is often called vertex-correction, when the interaction with the magnetic field happens during the time when the photon is emitted and self-energy when it happens before or after the emittance and re-absorption<sup>1</sup>. Vacuum polarization on the other hand describes a process where a virtual electron-positron pair is created for a short period of time (due to Heisenberg's uncertainty principle this is consistent with the conservation of energy). With higher orders, more possible combinations arise, therefore, for the next terms  $C_6$ ,  $C_8$ , and  $C_{10}$ , 72, 891, and 12 672 Feynman-diagrams have to be computed.

---

<sup>1</sup> The literature is not always consistent with these definitions. Since self-energy is the more comprehensive term, it will be used later in this work as a synonym for both effects.

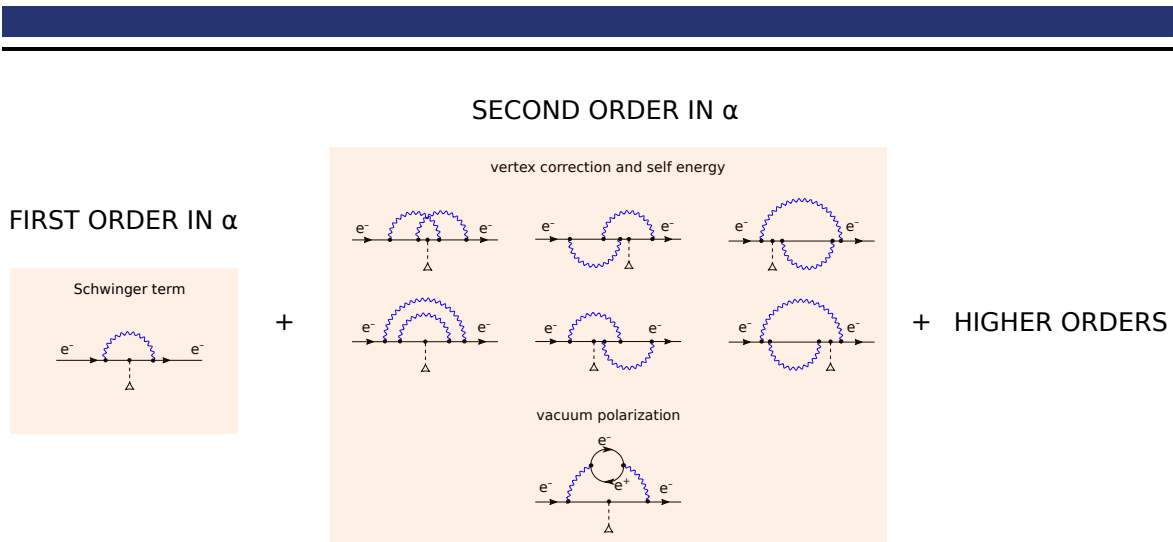


**Figure 2.2:** Feynman-diagrams for the first- and second-order QED contributions of the magnetic moment of the free electron. For the first-order effect, the so-called Schwinger term is shown. For the second order, all possible diagrams with four vertices contribute. The corresponding effects are self-energy and vacuum polarization. Self-energy describes an electron emitting and absorbing a virtual photon. Vacuum polarization is due to the creation of a virtual electron-positron pair for a short period of time. Please note that the time evolution axis is always from the left to the right.

## 2.2 The $g$ -Factor of the Bound Electron

For an electron bound to a nucleus the gyromagnetic factor  $g_j$  is defined similarly to  $g_s$  by [21]:

$$\frac{\vec{\mu}_j}{\mu_B} = -g_j \cdot \frac{\vec{j}}{\hbar} \quad \text{with} \quad \mu_B = \frac{e \hbar}{2 m_e}, \quad (2.3)$$

but with the total angular momentum  $\vec{j} = \vec{l} + \vec{s}$ , which is the coupled orbital angular momentum, and the spin of the electron. In an external magnetic field  $\vec{B} = (0, 0, B)$  this leads to a splitting of energy:

$$\Delta E = \hbar \omega_L = g_j \mu_B B, \quad (2.4)$$

with  $\omega_L = 2 \pi \nu_L$  being the so-called Larmor frequency which originates from the precession of the electron spin due to its magnetic moment around the magnetic field lines. Figure 2.3 shows a schematic of this process.

Additionally, the ion also experiences a force that leads to a circulation around the magnetic field lines with the frequency  $\omega_c$  (called cyclotron frequency):

$$\omega_c = \frac{QB}{M}, \quad (2.5)$$

with the total charge of the ion  $Q$  and its mass  $M$ .

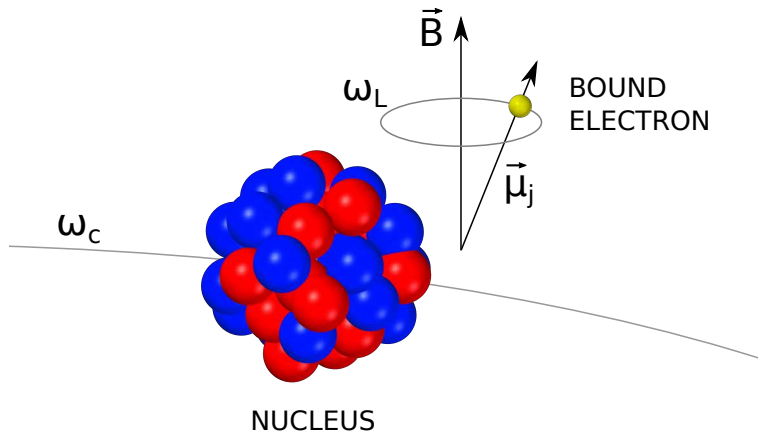


**Figure 2.3:** A highly charged ion with one electron orbiting around the nucleus circulates perpendicularly to the magnetic field  $\vec{B}$  with a frequency  $\omega_c$ . The electron, due to its spin, precesses around the magnetic field lines with the Larmor frequency  $\omega_L$ .

With this cyclotron frequency (which will be explained in more detail in section 3.2) the magnetic field strength can be determined to a high precision and the  $g$ -factor can be expressed by a ratio of the two frequencies  $\omega_L/\omega_c$ :

$$g_j = \frac{\hbar \omega_L}{\mu_B B} = \frac{\hbar \omega_L Q}{\mu_B \omega_c M} = 2 \frac{\omega_L Q m_e}{\omega_c M e}. \quad (2.6)$$

---

### 2.2.1 Bound-State QED

---

The theory of bound-state QED requires some modifications to the QED calculations used for the free electron. Due to its complexity only the basic ideas can be described here; for an overview of the theoretical methods developed in the past years, refer to [22].

Calculations of the  $g$ -factor of the bound electron start again with Dirac's equation, giving the leading-order Dirac-Breit term  $g_D$  in

$$g = g_D + \Delta g_{\text{QED}} + \Delta g_{\text{int}} + \Delta g_{\text{sQED}} + \Delta g_{\text{nuc}}. \quad (2.7)$$

The other terms account for the different effects that have to be taken into consideration and will be explained further. Therefore, figure 2.4 gives a schematic drawing of the different Feynman-diagrams that need to be computed.



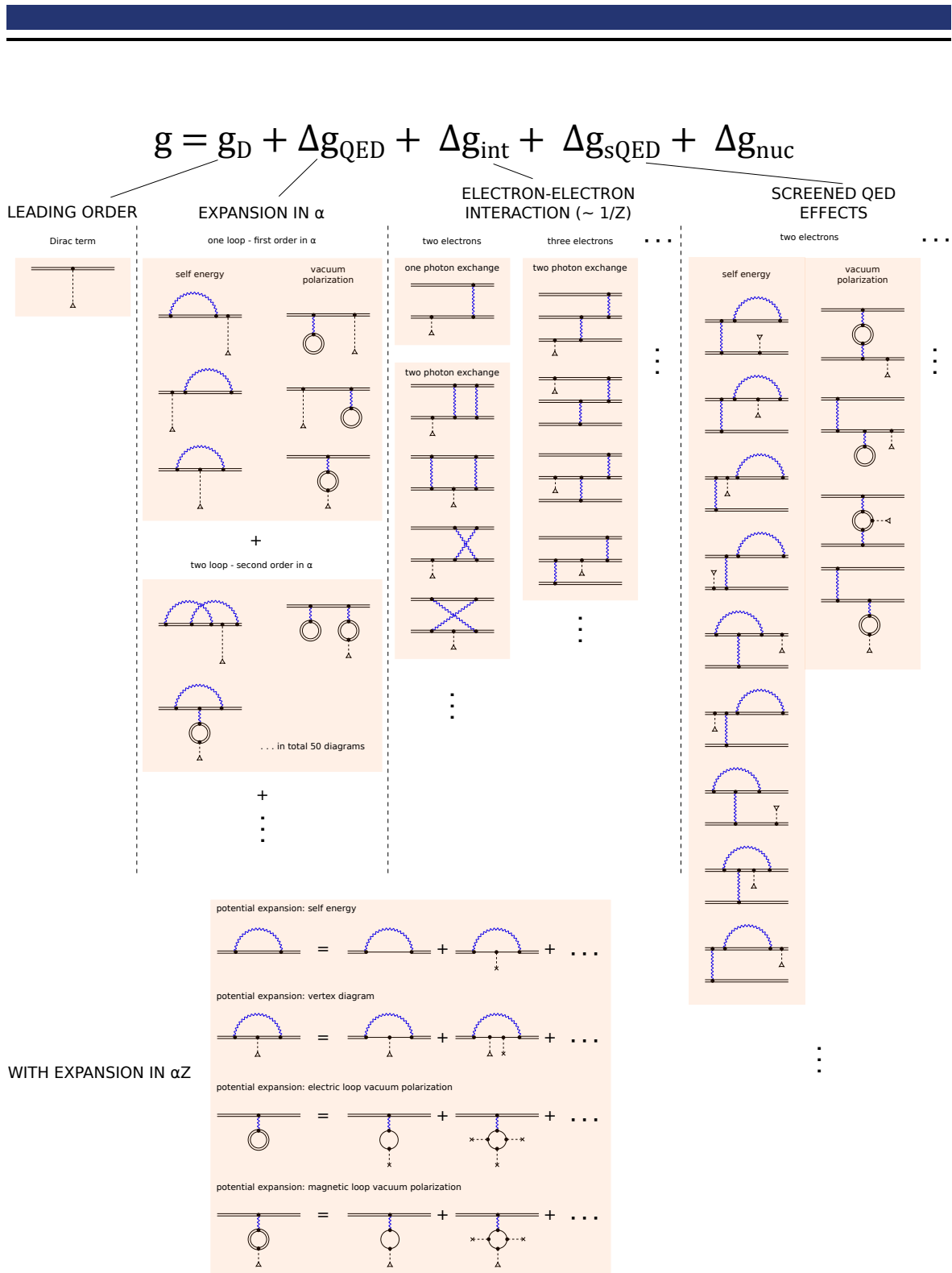


**Figure 2.4:** Schematic for the different contributions to the  $g$ -factor for a many-electron system that is calculated in the framework of bound-state QED. The last summand,  $\Delta g_{\text{nuc}}$  represents the nuclear recoil, finite nuclear size and nuclear polarization corrections. More information about it and about the other summands is found in the text.

In Feynman-diagrams for BS-QED, an electron is drawn with a double solid line, indicating the electron always propagates in the Coulomb field of the nucleus. This is why for every Feynman-diagram *e.g.* self energy, vertex corrections or vacuum polarization, an expansion in  $\alpha Z$  has to be made, where  $\alpha \approx 1/137$  is again the fine-structure constant and  $Z$  is the electric charge state of the ion. This is shown in the lower end of figure 2.4. With  $Z$  roughly in the order of  $1/\alpha$  this expansion cannot be treated by perturbation theory anymore. Nevertheless, it is needed to separate the leading-order terms. These terms are formally ultraviolet-divergent and need to be treated differently in order to get a finite result [21]. The remaining higher-order terms are then, by the formula, summed and can then be calculated.

**$\Delta g_{\text{QED}}$ , the QED corrections:** the QED corrections are quite analogous to the case of the free electron; again an expansion in  $\alpha$  is made. Note that this time, already in the first order, six Feynman-diagrams have to be calculated. For vacuum polarization this can be divided into electric-loop (the upper two) and magnetic-loop (the lower one) contributions. For the second order the complexity also rises more strongly than in the free-electron case; a total of 50 diagrams need to be computed.

**$\Delta g_{\text{int}}$ , the interelectronic-interaction corrections:** the interelectronic-interaction corrections result from the exchange of photons between the electrons. The corrections are in the order of  $(\alpha Z)^2/Z^n$ ; with  $n$  being the number of exchanged photons. They are suppressed by  $\sim 1/Z$  as an effective expansion parameter. If there are more than two electrons, also many-electron photon exchange has to be taken into account.

**$\Delta g_{\text{sQED}}$ , the screened QED corrections:** the screened QED corrections account for the Feynman-diagrams for many-electron systems that contain vacuum polarization and self energy. They contribute to the screening of the one-electron QED effects. Since the accuracy of calculating this effect worsens for lower  $Z$ , for  $\text{Ar}^{13+}$  an alternative ansatz to this rigorous evaluation has to be taken by computing the one-electron QED corrections with a screened potential [21].

**$\Delta g_{\text{nuc}}$ , the nuclear recoil, finite nuclear size and nuclear polarization corrections:** nuclear recoil, finite nuclear size, and nuclear polarization corrections originate from various assumptions that had to be made beforehand: a finite nuclear mass was not considered in the previous calculations, taking it into account leads to nuclear recoil. The finite nuclear-size corrections stem from the modification of the nuclear potential because of the nuclear charge distribution and can only be calculated with a high uncertainty [23]. Nuclear polarization is only a small contribution stemming from the virtual excitation of nuclear energy levels, nevertheless, it can limit the theoretical accuracy [24].

In the case of boron-like argon,  $\text{Ar}^{13+}$ , the methods and values that have been calculated can be found in [25], with an additional emphasis on nuclear recoil in [26]. Their contribution to the total value of the  $g$ -factor in  $\text{Ar}^{13+}$  can be found in figure 2.6.

## 2.2.2 Ar<sup>13+</sup> as a First Candidate

As a first candidate for a measurement in ARTEMIS, boron-like argon, <sup>40</sup>Ar<sup>13+</sup>, is chosen. The term ‘boron-like’ depicts that there are five electrons left, with two closed s shells and a 2p valence electron. Due to spin-orbit coupling (LS-coupling) there is a fine-structure doublet with the levels <sup>2</sup>P<sub>1/2</sub> and <sup>2</sup>P<sub>3/2</sub>. Additionally, due to the magnetic field of the Penning trap, also Zeeman splitting takes place. A Grotrian-diagram of the energy levels in Ar<sup>13+</sup> is given in figure 2.5.

### Laser-Accessible Transitions in HCl

Due to the high electromagnetic fields an electron is exposed to in highly charged ions, the fine-structure (FS) and hyperfine-structure (HFS) transitions are shifted to much higher energies compared to singly-charged ions. For hydrogen-like and other few-electron systems the energy of the HFS scales like  $Z^3$  and the fine-structure splitting like  $Z^4$  [27]. Therefore, potential candidates for optical transitions are in the medium  $Z$  range in case of the fine-structure splitting and in the high  $Z$  range in case of hyperfine-structure splitting. For Ar<sup>13+</sup> the fine-structure splitting between <sup>2</sup>P<sub>1/2</sub> and <sup>2</sup>P<sub>3/2</sub> has an energy of around 2.8 eV with a corresponding wavelength of 441.255 75(17) nm [28]. It is a magnetic-dipole transition and the <sup>2</sup>P<sub>3/2</sub> excited state has a lifetime of 9.573(6) ms [29]. For a more complete list of other publications as well as theoretical values please see [18].

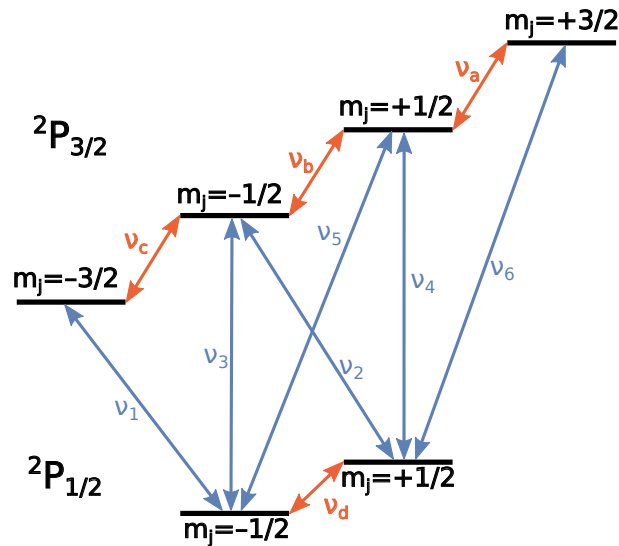


**Figure 2.5:** Grotrian-diagram for the <sup>2</sup>P<sub>1/2</sub> - <sup>2</sup>P<sub>3/2</sub> transition in Ar<sup>13+</sup>, in blue depicted are the optically accessible fine-structure transitions with a wavelength of approximately 441 nanometer. The red arrows mark the Zeeman-splitting transitions due to the 7 tesla field of the Penning trap. The Larmor frequency  $\nu_L$  of the lower transition ( $\nu_d$ ) is around 65 gigahertz, whereas the three upper transitions ( $\nu_a$ ,  $\nu_b$ ,  $\nu_c$ ) have a frequency of around 130 gigahertz.

---

## The $g$ -factor of $\text{Ar}^{13+}$

---

Using Dirac's theory, the leading-order term  $g_D$  that contributes most can be computed for a hydrogen-like ion with a point-like nucleus [11]:

$$g_D = \frac{\kappa(2\kappa - 1)}{2j(j + 1)} \left( 1 - \frac{\kappa}{2\kappa - 1} \frac{(\alpha Z)^2}{n^2} + \dots \right) \quad \text{with} \quad \kappa = (-1)^{j+l+\frac{1}{2}} \left( j + \frac{1}{2} \right), \quad (2.8)$$

where  $n$ ,  $l$  and  $j$  are the principal quantum number, the orbital angular momentum and the total angular momentum, respectively. For hydrogen-like argon with  $Z = 18$ ,  $n=2$ ,  $l=1$  and  $j=1/2$  and  $3/2$  it yields

$$\begin{aligned} g_{1/2} &= \frac{2}{3} - \frac{1}{6} (\alpha Z)^2 + \dots \approx 0.6638, \\ g_{3/2} &= \frac{4}{3} - \frac{2}{15} (\alpha Z)^2 + \dots \approx 1.331. \end{aligned} \quad (2.9)$$

This is already a very good approximation to the values given in [26]. The next corrections start from  $10^{-3}$ . In figure 2.6 the theoretical calculations of different contributions for the combined  $g$ -factor  $g \equiv 3g_{3/2} - g_{1/2}$  are shown. By measuring  $g$  to different levels of accuracy, more and more theoretical aspects of bound-state QED come within reach to be tested.

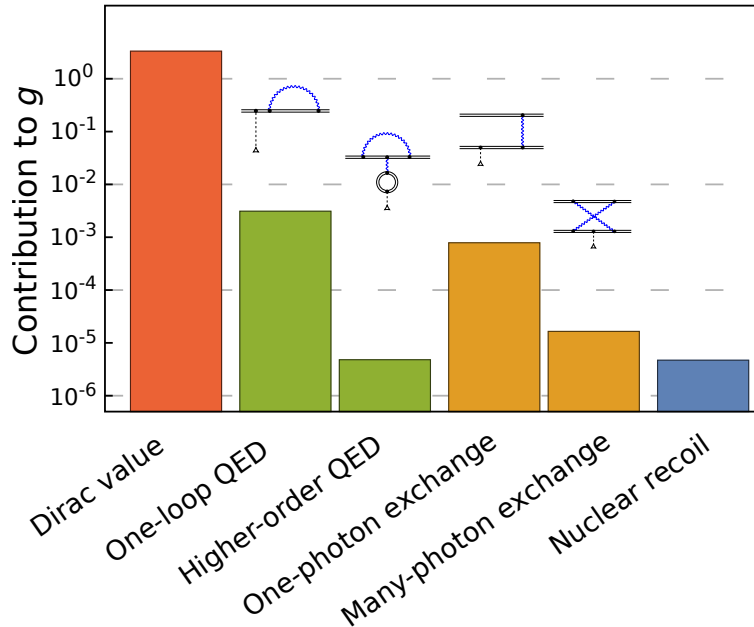


**Figure 2.6:** The absolute theoretical contributions to the  $g$ -factor of boron-like argon. The Dirac value, which can be solved analytically, contributes the most. QED effects and many-electron effects, such as photon exchange only contribute on the level of  $10^{-3}$ . Data taken from [26].

## 2.3 Double-Resonance Spectroscopy

ARTEMIS, complementary to other  $g$ -factor experiments with Penning traps, does not measure the Larmor frequency  $\nu_L$  by the technique of the continuous Stern-Gerlach effect [30], but with the so-called ‘double-resonance spectroscopy’. In this section the basic idea behind this technique is outlined. For a more detailed view, see [16, 17].

The double-resonance technique already has been applied to free atoms in the early fifties [31]. Henceforth, with the availability of lasers the technique made its way as a common tool for spectroscopy with two frequencies available in a three-level system [32].

### 2.3.1 Measurement Scheme

Figure 2.7 gives an example of how to measure the Zeeman-splitting energy via double-resonance spectroscopy in ARTEMIS: a closed optical cycle is probed by a laser with frequency  $\nu_6$ , leaving roughly half of the population in  $|3/2, +3/2\rangle$ . The fluorescence light is detected via a photon counter or a camera (see section 4.3.3). A tunable microwave field is shone into the trap. If the microwave comes into resonance with the upper Larmor frequency  $\nu_a$ ,  $|3/2, +1/2\rangle$  is populated. Two decay channels are possible – either a decay in  $|1/2, +1/2\rangle$  or in  $|1/2, -1/2\rangle$ . The latter is a dark state, populating it will result in a loss of fluorescence and therefore indicating that the microwave is into resonance with  $\nu_a$ .

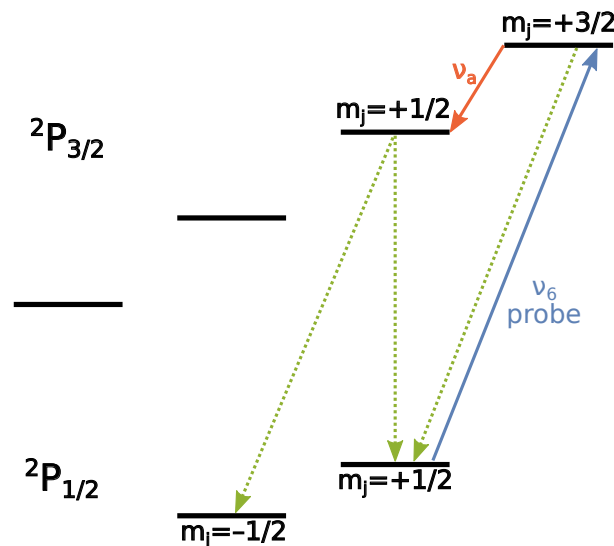


**Figure 2.7:** Level structure showing one example for double-resonance spectroscopy in  $Ar^{13+}$ , by measuring the Zeeman transition  $\nu_a$ : a closed optical cycle is probed by a laser with frequency  $\nu_6$  while the fluorescence light is detected. Meanwhile, a tuned microwave is shone in, which will, when coming into resonance with  $\nu_a$ , result in a population of the dark state  $|1/2, -1/2\rangle$  and therefore in a loss of fluorescence.

### 2.3.2 Higher-Order Zeeman Effect

Since the ions are stored in a magnetic field  $B$  of 7 tesla, Zeeman splitting occurs. This splitting is equidistant in the first-order approximation, but, for higher orders, this symmetry is disturbed by nonlinear magnetic field effects. The shifts of each level can be calculated within perturbation theory by [16]:

$$E_A(B) = E_A^{(0)}(B) + \Delta E_A^{(1)}(B) + \Delta E_A^{(2)}(B) + \Delta E_A^{(3)}(B) + \dots, \quad (2.10)$$

where  $|A\rangle = |j, m_j\rangle$  is the  $2^2P_j$  state with angular momentum  $j$  and its projection  $m_j$ , and  $E_A^{(0)}$  is the energy in absence of magnetic field. The first-order shift already relates the Larmor frequency  $\nu_L$  to the  $g_j$ -factor:

$$\Delta E_A^{(1)}(B) = h \nu_L = g_j m_j \mu_B B. \quad (2.11)$$

Higher order contributions have been calculated for the case of  $\text{Ar}^{13+}$ . Their frequency shifts can be seen in figure 2.8. Exact values for these calculations can be found in [18].

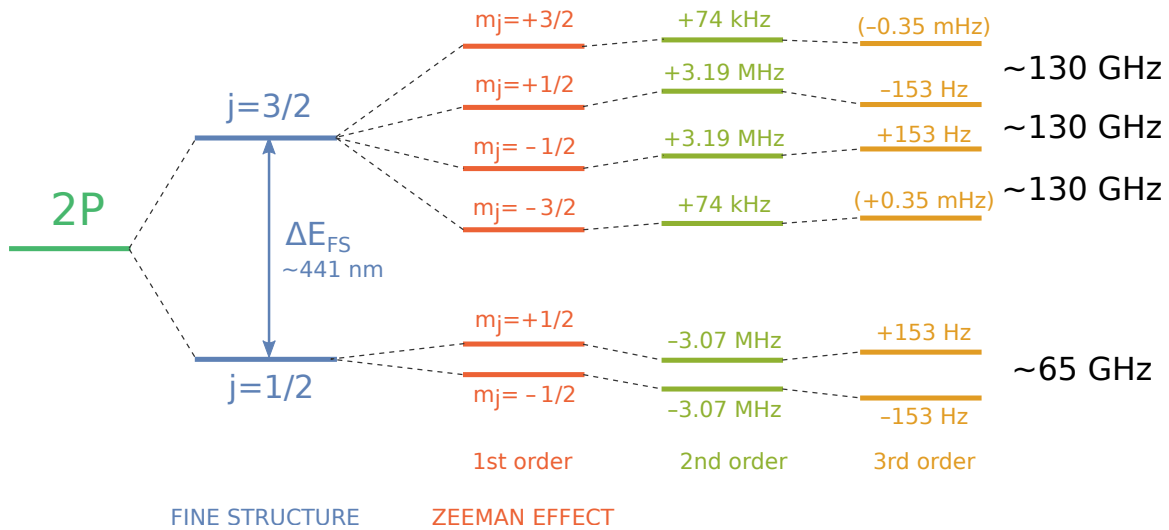


**Figure 2.8:** Higher-order Zeeman level structure for boron-like argon  $\text{Ar}^{13+}$ , not to scale. The fine-structure energy splitting in the optical range (accessible by a blue laser of 441 nm) and the Zeeman splitting with the higher order shifts of the frequency  $\nu_L$  are shown. The splittings are accessible by microwaves. With the expected accuracy of a few hertz for the current setup, even some parts of the third-order Zeeman effect should be measurable.

For a final measurement of the  $g$ -factor of boron-like argon and all higher-order Zeeman shifts, the transition frequencies have to be disentangled by measuring various optical frequencies and Zeeman levels. The possible transitions were shown in figure 2.5. Schemes for this disentanglement and how to measure them are outlined in great detail in [18, 16].

---

## 3 The Penning Trap

To enable  $g$ -factor measurements of highly charged ions via double-resonance spectroscopy, ARTEMIS is using a Penning trap, a tool that allows confinement and manipulation of ion clouds. Externally or internally produced ions can be stored in an ultra-high-vacuum environment for weeks and with different techniques, the cloud can be cooled and purified, such that only desired ion species remain in the trap. The Penning trap is a widely used tool for high-precision experiments, its principal technique of combining a magnetic and an electric field in order to confine charged particles was already developed in the 1930s by F.M. Penning. Nevertheless, using the technique for storing charged particles in order to investigate them was first done by H.G. Dehmelt who was rewarded one quarter of the Nobel Prize in 1989 ‘for the development of the ion trap technique’ [5]. In this chapter the principal theory of Penning traps and their further development is presented. A focus is on the motions that charged particles perform and how these motions shift in frequency due to various effects. This chapter is based on [21] which is recommended for more details about Penning traps and their applications.

---

### 3.1 The Principal Design

---

A charged particle is confined in a Penning trap by the superposition of a homogeneous magnetic field  $\vec{B} = (0, 0, B)$  with an electric quadrupole field  $\vec{E} = -\nabla\Phi$  (with the potential  $\Phi$  given in equation 3.1). When trapped, the charged particle can perform three independent motions. They are described in section 3.2. These motions are only independent for a single charged particle and in the case of a perfect quadrupole electrical potential, a perfectly ‘harmonic’ trap. This condition is satisfied the most by a precisely machined **hyperbolically shaped electrode trap**. But already small errors in machining or also necessary variations, such as holes and slits for optical access or particle loading, will distort the quadrupole potential hence introducing anharmonicities. The electrostatic potential near the trap center can be written by the expansion [33]:

$$\Phi = U_T \sum_{k=0}^{\infty} C_k \left(\frac{\rho}{d}\right)^k P_k(\cos \theta) \quad (3.1)$$

where  $P_k(\cos \theta)$  are Legendre polynomials of the  $k$ -th order,  $\cos \theta = z/\sqrt{\rho^2 + z^2}$ , with  $\rho$  and  $z$  being the radial and the axial distance to the trap center. The character-

istic trap dimension  $d$  is dependent on the parameters  $\rho_0$  and  $z_0$  shown in figure 3.1.

$$d^2 = \frac{1}{4}\rho_0^2 + \frac{1}{2}z_0^2 \quad (3.2)$$

The  $C_k$  coefficients are 0 for odd terms if the trap has electric symmetry with respect to the trap center.  $C_0$  is an overall potential offset and has no effect on the ion motion;  $C_2$  represents the harmonic potential and would be the only non-zero factor for an ideal quadrupole trap. Due to imperfections  $C_4$  and  $C_6$  will distort the harmonicity, keeping them as small as possible is achieved by ‘compensation’. Terms above  $C_6$  may be neglected due to their contribution being below the experimental resolution [21].

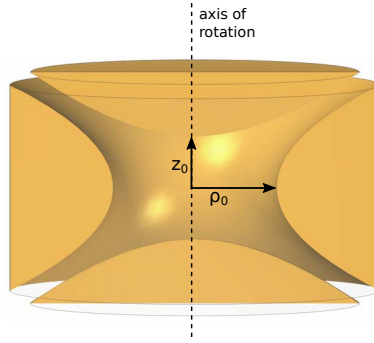


**Figure 3.1:** Cross-section of a Penning trap with hyperbolically shaped electrodes, indicating the radial and axial trap parameters  $\rho_0$  and  $z_0$ .

An alternative to hyperbolically shaped electrodes is a combination of a cylindrical electrode<sup>1</sup> at a potential  $U_0$  with two flat endcaps as shown in figure 3.2(a). With the correct ratio of  $\rho_0 \approx 1.203z_0$  the potential can be shaped such that it mimics a harmonic quadrupole potential ( $C_4 = 0$ ) – it is **mechanically compensated** [34]. In order to further shape the potential and correct anharmonicities, compensation electrodes with tunable potential  $U_c$  can be added (Fig. 3.2(b)) and thus present an **electrically compensated** trap.  $C_2$  and  $C_4$  can therefore be written as:

$$C_2 = C_2^{(0)} + D_2 \frac{U_c}{U_T} \quad \text{and} \quad C_4 = C_4^{(0)} + D_4 \frac{U_c}{U_T} \quad (3.3)$$

with  $C_2^{(0)}$ ,  $C_4^{(0)}$  and  $D_2$ ,  $D_4$  coming from the trap geometry, as explained in [33].  $U_c/U_T$  is called the ‘tuning ratio’. If the frequencies of ion motion are independent of this tuning ratio, one can speak of an ‘orthogonalized’ trap.

In order to get optical access or for proper loading of particles, at least one of the endcap electrodes has to be an **open-endcap tube** [33]. An example of this can be seen in 3.2(c). By choosing the correct geometry ( $z_e \approx 4 \cdot z_0$ , for  $z_0 \approx \rho_0$ ) orthogonalization is also possible. The trap used in the ARTEMIS experiment mixes

<sup>1</sup> This electrode is often referred to as the ‘ring electrode’



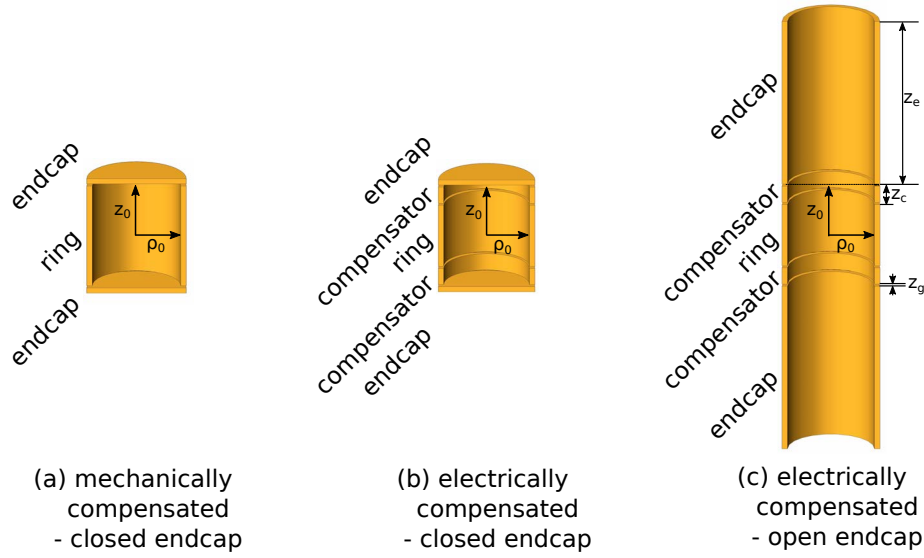


**Figure 3.2:** Cross-section views of different Penning trap types. (a) The mechanically compensated trap is made harmonic by choosing the correct ratio of radius  $\rho_0$  and axial distance  $z_0$ . (b) The electrically compensated trap includes two additional compensation electrodes, shaping the potential for better harmonicity. (c) The closed endcaps are replaced by open endcap tubes, where  $z_c$  denotes the height of the compensation electrodes and  $z_g$  the gaps between the different electrodes. The length of the tubes is given by  $z_e \approx 4z_0$  (for  $z_0 \approx \rho_0$ ).

many of these concepts paired with some novel ideas (for example the ‘asymmetric trap’, Sec. 4.5), forming a ‘double trap’ [35]. It combines two individual Penning traps that serve different purposes, *i.e.* a creation trap (CT) designed for higher energy ion creation and a tunable highly harmonic spectroscopy trap (ST). Further explanation of the specific design of ARTEMIS can be found in section 4.5.

Penning traps have proven to be an important tool in physics and over the past years many variations of the basic idea have been invented, such as small modifications like the hybrid design, a toroidal ring electrode with cylindrical compensation and endcap electrodes [36] or even more extreme, by making the trap completely two dimensional, in the form of a planar trap [37, 38].

---

## 3.2 Ion Motion

---

In a Penning trap, an ion with mass  $M$  and charge  $Q$  can perform three independent oscillatory motions: an **axial motion** with frequency  $\omega_z$  in the potential  $U_0$ ; a **modified cyclotron motion** with frequency  $\omega_+$  and the **magnetron motion** with frequency  $\omega_-$  due to the  $\vec{E} \times \vec{B}$  drift. The theoretical derivation of these motions from

the Lorentz force can be found in many textbooks (for example in [39]), resulting in the three equations for the corresponding frequencies:

$$\omega_z = \sqrt{\frac{Q U_0}{M d^2}} = \sqrt{\frac{Q C_2 U_T}{M d^2}} \quad \text{and} \quad \omega_{\pm} = \frac{\omega_c}{2} \pm \sqrt{\left(\frac{\omega_c}{2}\right)^2 - \frac{\omega_z^2}{2}}, \quad (3.4)$$

where  $U_T$  is the (applied) trap voltage,  $d$  the characteristic trap dimension,  $C_2$  the trap coefficient as introduced in equation 3.1 and  $\omega_c$  is the free cyclotron frequency, directly proportional to the magnetic field  $B$  as introduced in section 2.2:

$$\omega_c = \frac{Q}{M} B, \quad (3.5)$$

Note, that without an electrostatic potential, a charged particle exposed to a magnetic field would spiral with a cyclotron frequency  $\omega_c$ . By superimposing with the electric field the free cyclotron frequency  $\omega_c$  is reduced to the modified cyclotron frequency  $\omega_+$ . Usually, their magnitudes follow the hierarchy  $\omega_c > \omega_+ \gg \omega_z \gg \omega_-$ . The free cyclotron frequency can easily be calculated by  $\omega_c = \omega_+ + \omega_-$ . However, this relation is only correct in an ideal case. A better way to obtain  $\omega_c$  is via the Brown-Gabrielse invariance theorem [40] which is more robust against first-order trap imperfections (for example a slight tilt in the magnetic field as it is described in the see next section). Therefore,  $\omega_c$  can be estimated by:

$$\omega_c = \sqrt{\omega_z^2 + \omega_+^2 + \omega_-^2}. \quad (3.6)$$

In section 5.7 this relation will be used to estimate the cyclotron frequency in one of the traps of ARTEMIS by measuring  $\omega_+$ .

The corresponding amplitudes  $A$  for the three different motions are given by:

$$A_z^2 = \frac{E_z}{Q C_2 U_T} d^2, \quad A_+^2 = \frac{2 E_+}{M (\omega_+^2 - \omega_z^2/2)} \quad \text{and} \quad A_-^2 = \frac{2 E_-}{M (\omega_-^2 - \omega_z^2/2)}, \quad (3.7)$$

where  $E_z$ ,  $E_+$  and  $E_-$  are the kinetic energies of the ion motions, directly related to their temperatures<sup>2</sup> by  $E = \frac{1}{2} k_B T$ . Please note that the magnetron motion is unbound, resulting in a negative energy (Sec. 3.2.2). Table 3.1 gives the theoretical frequencies and amplitudes for a single Ar<sup>13+</sup> ion in the two different traps, calculated with the previous formulas for a given set of parameters. Figure 3.3 depicts the corresponding motion of the ion.

<sup>2</sup> The concept of temperature can be applied for a cloud of ions since the trapped particles are in thermal equilibrium with the environment (an infinite thermal bath) and therefore follow a Boltzmann distribution. For a single particle a temperature can still be defined due to the ergodic hypothesis: the time average of a statistical quantity has the same behavior as the ensemble average of that quantity [41].

**Table 3.1:** Calculated frequencies and amplitudes for an  $\text{Ar}^{13+}$  ion in the creation and the spectroscopy trap, respectively. A temperature of 4 kelvin is assumed. The values are calculated with the actual axial frequencies of the resonators from table 4.1, a trap voltage of  $U_T = 55\text{ V}$  for the CT and  $U_T = 39.3\text{ V}$  for the ST, and the trap parameters from table 4.14.

Creation Trap		Spectroscopy Trap	
Frequency	Amplitude	Frequency	Amplitude
$\omega_z = 2\pi \times 737\text{ kHz}$	$A_z = 6.2\ \mu\text{m}$	$\omega_z = 2\pi \times 694.5\text{ kHz}$	$A_z = 8.7\ \mu\text{m}$
$\omega_+ = 2\pi \times 34.9224\text{ MHz}$	$A_+ = 0.2\ \mu\text{m}$	$\omega_+ = 2\pi \times 34.9283\text{ MHz}$	$A_+ = 0.2\ \mu\text{m}$
$\omega_- = 2\pi \times 7.8\text{ kHz}$	$A_- = 12\ \mu\text{m}$	$\omega_- = 2\pi \times 6.9\text{ kHz}$	$A_- = 13\ \mu\text{m}$
$\omega_c = 2\pi \times 34.9302\text{ MHz}$		$\omega_c = 2\pi \times 34.9352\text{ MHz}$	

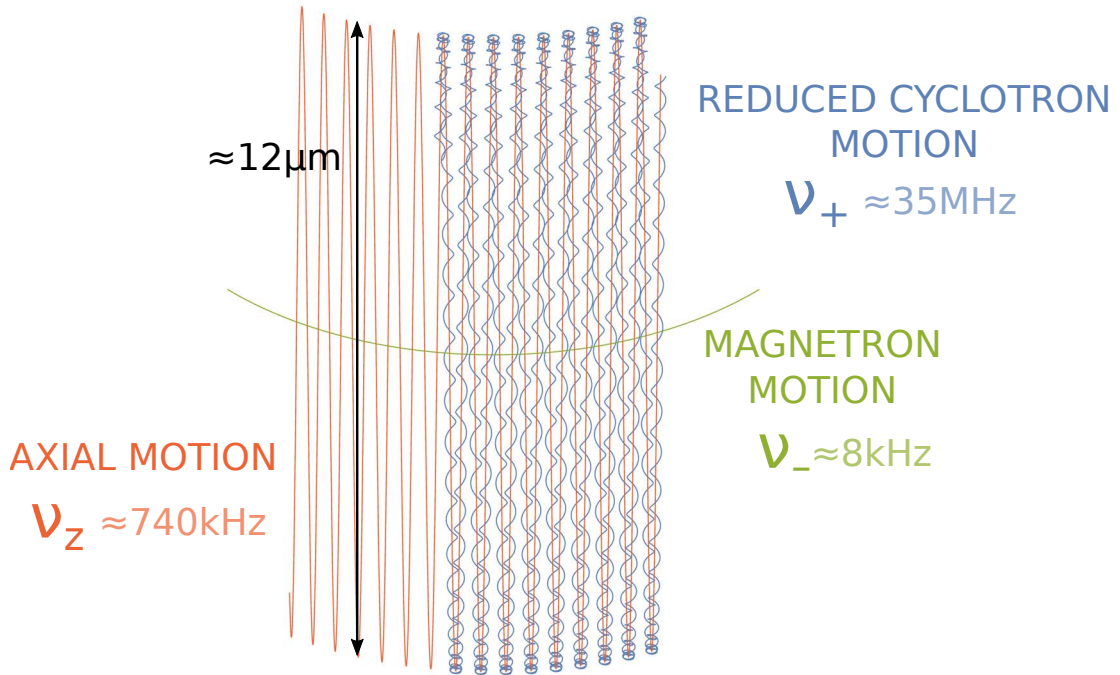


**Figure 3.3:** Trajectories of the three independent ion motions for a single  $\text{Ar}^{13+}$  ion in the creation trap. The frequencies and amplitudes are to scale, according to the values calculated in table 3.1. For every magnetron oscillation around 90 axial oscillations take place and for every axial oscillation, the ion circulates 50 times according to the reduced cyclotron motion.

---

### 3.2.1 Frequency Shifts

---

In a non-ideal Penning trap, shifts of the motional frequencies can occur, for example: higher-order terms in the electric and magnetic field, effects due to relativity, image charges and in many-ion systems also space-charge effects. A theoretical treatment with classical perturbation theory of these shifts in single-ion systems can be found in [42]. For many-ion systems a detailed description of the frequency shifts is given in [21].

---

#### Trapping-Field Imperfections

---

Trapping-field imperfections cause the most relevant frequency shifts, stemming from the deviation of the homogeneous magnetic field by introducing a quadratic component  $B_2$ , and from the quadrupolar electric field by having a non-zero  $C_4$ . For these energy-dependent shifts, twelve dependencies (four frequencies, including  $\omega_L$  and the three motional energies  $E_z, E_+, E_-$ ) can be found in [43]:

$$\begin{pmatrix} \Delta\omega_+/\omega_+ \\ \Delta\omega_z/\omega_z \\ \Delta\omega_-/\omega_- \\ \Delta\omega_L/\omega_L \end{pmatrix} = (M_E + M_B) \begin{pmatrix} E_+ \\ E_z \\ E_- \end{pmatrix} \quad (3.8)$$

$$\text{with } M_E = \frac{6C_4}{QC_2U_T} \begin{pmatrix} \eta^4/4 & -\eta^2/2 & -\eta^2 \\ -\eta^2/2 & 1/4 & 1 \\ -\eta^2 & 1 & 1 \\ 0 & 0 & 0 \end{pmatrix} \quad (3.9)$$

$$\text{and } M_B = \frac{1}{2m\omega_-\omega_+} \frac{B_2}{B} \begin{pmatrix} -\eta^2 & 1 & 2 \\ 1 & 0 & -1 \\ 2 & -1 & -2 \\ -\eta^2 & 1 & 2 \end{pmatrix}, \quad (3.10)$$

where  $\eta = \omega_z/\omega_+$  which is typically in the order  $10^{-2}$ , therefore the contribution of higher order terms of  $\eta$  are negligible. The three most relevant dependencies for the axial frequencies are:

$$\frac{\Delta\omega_z}{\omega_z} = \frac{3}{2} \frac{C_4}{QC_2U_T} E_z, \quad \frac{\Delta\omega_z}{\omega_z} = 6 \frac{C_4}{QC_2U_T} E_- \quad \text{and} \quad \frac{\Delta\omega_z}{\omega_z} = \frac{1}{M} \frac{B_2}{\omega_z^2 B} E_+. \quad (3.11)$$

---

## Field Alignment

---

Other effects that can distort the motional frequencies are either a tilt in the magnetic field axis – the trap axis in the z-direction has an angle  $\theta$  relative to the magnetic field lines; or a non-vanishing ellipticity  $\epsilon$  of the electric field, breaking its rotational symmetry [40]. The modified frequencies then are given by:

$$\omega'_z \approx \omega_z \left( 1 - \frac{1}{4} (3 + \epsilon) \sin^2 \theta \right) \quad \text{and} \quad \omega'_\pm \approx \omega_\pm + \frac{1}{2} \omega_- (3 + \epsilon) \sin^2 \theta. \quad (3.12)$$

Although these imperfections are neither avoidable nor negligible, the Brown-Gabrielse invariance theorem can still be applied.

---

## Space-Charge Effects

---

When trapping more than a single ion, frequency shifts due to the ion cloud have to be taken into account. For example, space-charge effects of the ions alter the effective trapping potential: with an amount of positive charges the negative trap potential is partially compensated – decreasing the trap depth and deforming the trapping potential. This results in a change of the ions' oscillation frequencies. It also gives a maximum amount of charges that can be confined. The equations for the frequency shift by space-charge effects can be found in [44]:

$$\omega'_z = \omega_z \sqrt{1 - \frac{\omega_p^2}{3 \omega_z^2}} \quad \text{and} \quad \omega'_\pm = \frac{\omega_c}{2} \left( 1 \pm \sqrt{1 - \left( 1 + \frac{2 \omega_p^2}{3 \omega_z^2} \right) \frac{2 \omega_z^2}{\omega_c^2}} \right), \quad (3.13)$$

where  $\omega_p$  is the plasma frequency  $\omega_p = (Q^2 n)/(\epsilon_0 M)$ ,  $n$  is the ion number density and  $\epsilon_0$  and  $M$  again the vacuum permittivity and the ion mass, respectively. By examining the square roots, two conditions can be deployed which can be used to get the maximum achievable ion density, called the Brillouin limit [21]:

$$n^{max} = \frac{\epsilon_0 B^2}{2 M}. \quad (3.14)$$

This Brillouin limit can be reached by the confinement condition  $2 \omega_z^2 \leq \omega_c^2$  [45].

---

### 3.2.2 Quantized Motions

---

The three ion motions are essentially harmonic oscillators and can be quantized. This is for example performed in [46] and yields the total energy as a sum of three modes dependent on their occupation numbers  $n_z$ ,  $n_+$  and  $n_-$ :

$$E_{total} = \hbar \omega_z \left( n_z + \frac{1}{2} \right) + \hbar \omega_+ \left( n_+ + \frac{1}{2} \right) - \hbar \omega_- \left( n_- + \frac{1}{2} \right). \quad (3.15)$$

Note that the magnetron motion has a ladder of negative energy states due to the unbound magnetron motion which is an unstable drift in the  $\vec{E} \times \vec{B}$  field – decreasing the energy of the motion will *increase* its amplitude (see equation 3.7). A level scheme for these energies is given in figure 3.4.

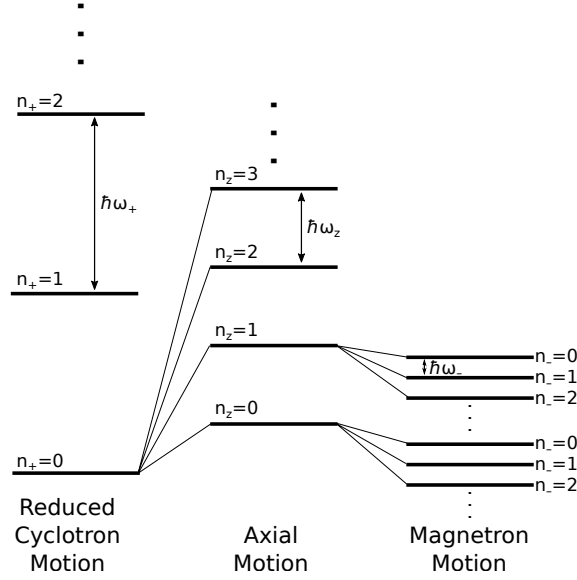


**Figure 3.4:** The level scheme for the quantized energy states of the three ion motions with their quantum numbers  $n_z$ ,  $n_+$ ,  $n_-$  and the related frequencies  $\omega_+ \gg \omega_z \gg \omega_-$ . Since the magnetron motion is unbound, it has a ladder of negative energy states. The different energies are not to scale.

### 3.3 Resonant Detection Circuits

The motion of the ions can be measured non-destructively by highly sensitive detection systems: electrical resonant circuits (RLC-circuits) provide a detectable signal when their eigenfrequency is in resonance with the ions' motional frequency. This section gives an introduction to the basic concept; for a more detailed overview, refer to [47]. The detection systems used in ARTEMIS are presented in section 4.3 and more details about how they can be used for cooling ion motions are presented in section 5.3. In ARTEMIS, two of the three motional frequencies can be measured directly, the axial frequency  $\omega_z$  and the reduced cyclotron frequency  $\omega_+$ .

A moving charged particle between two electrodes induces an image current [48]:

$$I_p = \frac{Q}{D} \dot{z}_i = \omega_z \frac{Q}{D} z_i, \quad (3.16)$$

where  $Q$  is again the ion's charge;  $z_i$  is the ion's coordinate and  $\omega_z$  the corresponding frequency.  $D$  is the effective electrode distance, a measure of the coupling strength

of the detection electronics to the ion and it depends on the trap geometry as well as on the pick up design. It is introduced in [49] and will be further characterized for ARTEMIS in section 5.3. The image current is usually in the range of femto- to picoampere, hence difficult to measure. Therefore, a resonant circuit can be used. If the motion of the ion is in resonance with the eigenfrequency  $\omega_0$  of the circuit, the current is converted to a voltage drop that can be measured with a spectrum analyzer. A schematic of the resonant detection system for ion-motion-frequency detection is given in figure 3.5.

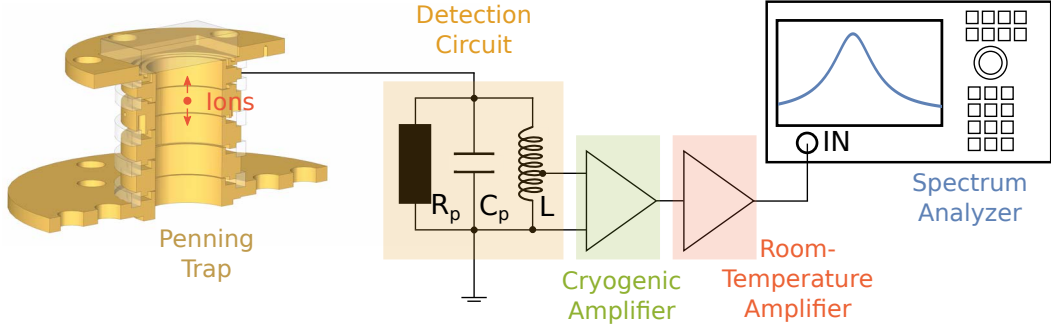


**Figure 3.5:** Schematic of the resonant ion-detection system. Moving ions between the electrodes induce a picked-up image current. If the motional frequency is in resonance with the eigenfrequency of the resonator, the frequency-dependent resistance results in a voltage drop. This voltage is further amplified by low-noise cryogenic and room-temperature amplifiers and then displayed by a spectrum analyzer.

Connecting an inductance  $L$  to an electrode together with the self-capacitance  $C_p$  will act like a parallel LC-resonator with the frequency

$$\omega_0 = \frac{1}{\sqrt{L C_p}}. \quad (3.17)$$

In resonance it also has a parallel ohmic resistance of

$$R_p = Q_{\text{res}} \sqrt{\frac{L}{C_p}} = Q_{\text{res}} \omega_0 L, \quad (3.18)$$

with  $Q_{\text{res}}$  being the ‘quality factor’ of this resonator. It is a ratio of the total energy in the circuit and the resistive energy loss per radian and can be estimated experimentally by:

$$Q_{\text{res}} = \frac{\omega_0}{\Delta\omega}, \quad (3.19)$$

where  $\Delta\omega$  is the  $-3$  dB width of the spectrum.

The frequency-dependent resistance results in a frequency-dependent voltage drop:

$$U_p = R_p I_p = Q_{\text{res}} \omega_0 L I_p, \quad (3.20)$$

which must be further amplified by additional low-noise cryogenic and room-temperature amplifiers, in order to be detectable.





## 4 Investigation of Argon Ions in the ARTEMIS Apparatus

This chapter gives an overview of the apparatus of the ARTEMIS experiment, with specific focus on the microwave implementation, the improvements of the detection electronics, and the new conductive window in the spectroscopy trap. It complements the discussion of the optics setup and the laser system in [50], the filterboards and the Penning trap in [18], the gas injection system in [51], and the cryogenic setup in [52].

The ARTEMIS experiment is located at the facility of heavy-ion research, the ‘GSI Helmholtzzentrum für Schwerionenforschung’ in Darmstadt, Germany (Fig. 4.1). This facility has an exceptional accelerator structure, capable of providing nearly any ion of interest. Since further ionization of heavy highly charged ions needs extremely high energies, they can only be produced in sufficient amounts by shooting ions at high velocities through thin foils, hence stripping off unwanted electrons. In order to conduct high precision experiments in Penning traps, these ions have to be decelerated and cooled again in the HITRAP-deceleration facility [13] to which, in the future, ARTEMIS will be connected (Sec. 4.6). Until this connection is finished, medium-heavy highly charged ions can be produced inside the trap (Sec. 4.5.2).

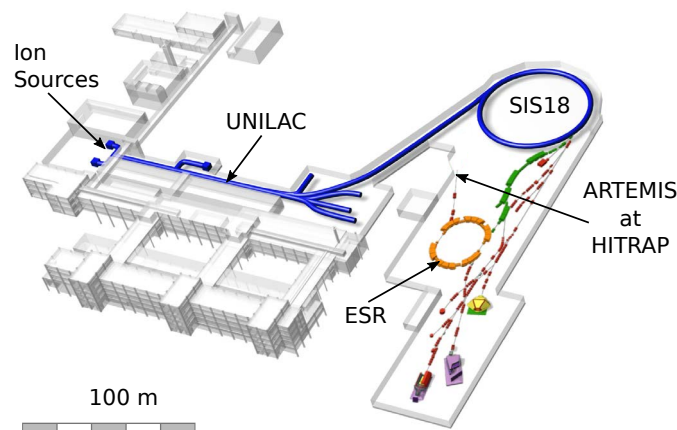


**Figure 4.1:** Overview of the ‘GSI Helmholtzzentrum für Schwerionenforschung’ facility. Ions produced in the ion sources are accelerated in the linear accelerator UNILAC and the synchrotron accelerator SIS18. They are then transferred to the experimental storage ring ESR, where they are cooled and then extracted into the HITRAP decelerator. There the ions are cooled almost to rest until they are transferred to the experiments, for example ARTEMIS. Figure taken from [53].

Since the high precision measurement of magnetic moments described in chapter 2 requires a strong homogeneous magnetic field, ARTEMIS utilizes a 7 tesla superconducting solenoid magnet (Sec. 4.1). Magnetization of surrounding materials might distort this magnetic field, therefore the magnet is mounted on an aluminium frame and in order to provide access to the top, a wooden tower surrounds the experiment. A CAD drawing of the tower built around the superconducting magnet is shown in figure 4.2(a). The magnet contains a vertical ‘warm’ bore into which the cryogenic part of the experiment is inserted. This part can be modified outside and is then inserted into the magnet via a hoist on top of the tower. The cryogenic part of the experiment (Fig. 4.2(b)) can be divided into four main sections: the cryocooler (Sec. 4.2), a two-stage refrigerator from which the experiment is suspended, capable of reaching temperatures down to 4 kelvin; the cryo-electronics housing with the detection units, the excitation parts, and the filterboards (Sec. 4.3); the trap chamber (Sec. 4.5), containing the double Penning trap that consists of the creation trap (CT) and the spectroscopy trap (ST); and finally, the gas injection for in-trap ion production (Sec. 4.5.2) which will be replaced in the future by a connection to the HITRAP beamline (Sec. 4.6).

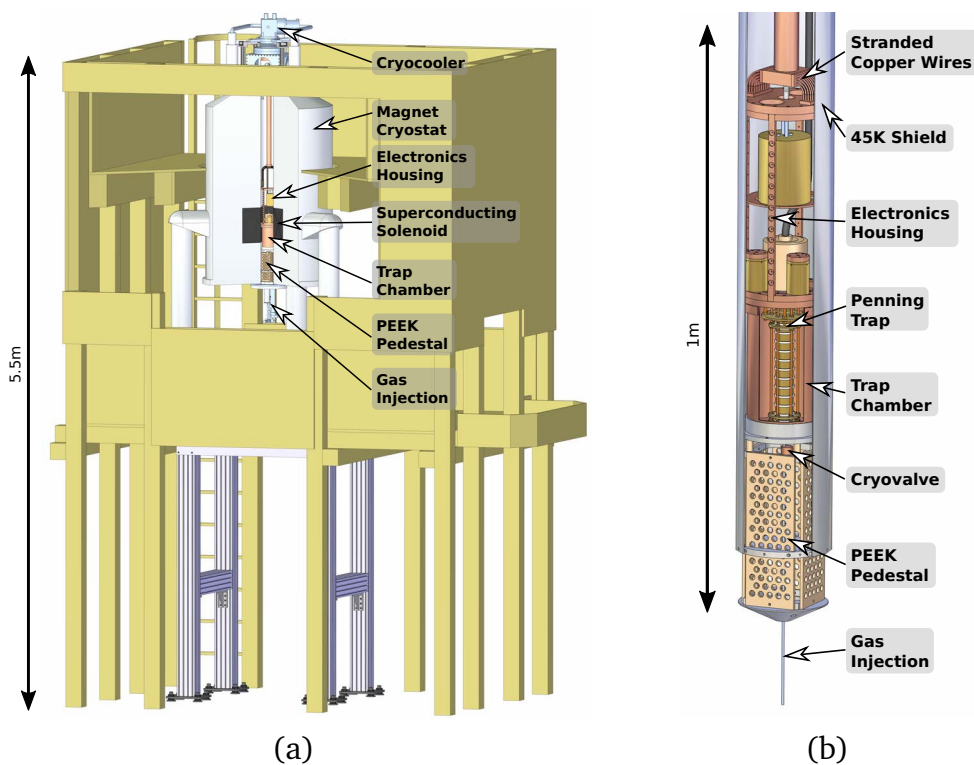


**Figure 4.2:** (a) CAD drawing of the superconducting magnet mounted on an aluminium frame, surrounded by a wooden tower to avoid distortions of the magnetic field. A cutout is applied to show the inner part of the experiment. (b) The inner part of the experiment. With a cut in the 45 K shield and the trap chamber to show the electronics and the trap. The different parts are explained in the following sections.

## 4.1 Magnet in the Wooden Tower

To provide the magnetic field for the Penning trap, a 7 tesla (7 T) superconducting magnet from VARIAN is used, comprising a superconducting niobium-titanium (NbTi) solenoid which is cooled to a temperature of 4 kelvin by liquid helium. A liquid nitrogen tank that has to be filled every two weeks protects the helium dewar from boiling off too quickly – providing a hold time of the 300 liter containing helium tank of almost one year. The magnet is operated in persistent mode, meaning it was initially energized with a current of 210 A in 2009 and is operating since then. The magnetic field has a highly homogeneous region with a central field strength of  $7.0\text{ T}^1$  and a specified homogeneity of better than 0.1 ppm over a volume of one cubic centimeter. Around the center is a cylindrical volume of 0.5 cm diameter and 10 cm length with a denoted homogeneity better than 10 ppm [18]. The high homogeneity is reached by additional shimming coils that were powered and adjusted when the magnet was initially set up.

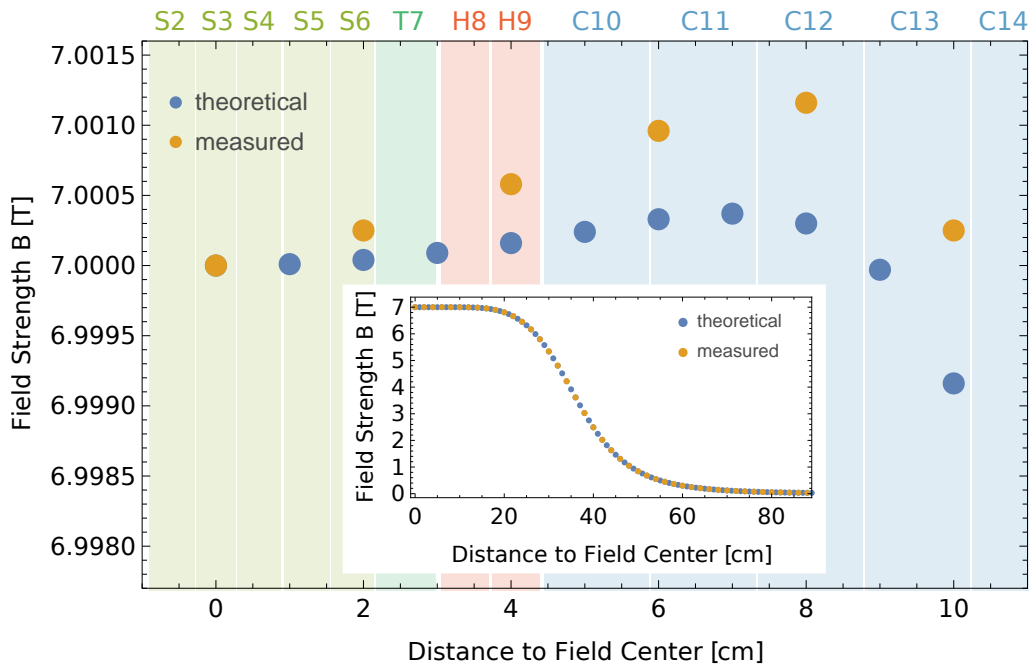


**Figure 4.3:** Magnetic field plot in the negative  $z$ -direction along the  $z$ -axis. The distance is given in centimeters from the magnetic field center. The points depict the theoretical field, as it was designed by the company, and the current field, as it was measured afterwards. The colored bars indicate the different electrodes of the Penning trap, they are to scale, according to figure 4.27(b). The inset shows the magnetic field strongly decreasing for longer distances from the field center. Please note, that for the field strength at the field center the theoretical and the measured value have the same value.

<sup>1</sup> Since there is a discrepancy between the measured values and the value of  $B=7.003\text{ T}$  that was also declared by the company, an additional measurement of the magnetic field strength must be carried out in order to determine which information is correct.

The magnetic field was designed and calculated by the company before this set-up. After magnetizing and shaping the magnetic field, the company conducted a measurement, yielding the current values for the field strength. Both sets of values are plotted in figure 4.3, showing the magnetic field strength on the  $z$ -axis in the negative  $z$ -direction (from the magnetic field center pointing to the bottom of the magnet). The values near the magnetic field center only slightly differ between the theoretical and the measured value; the highest difference of up to 0.003 T is at a distance of 28 cm. A more detailed discussion about the magnetic field in ARTEMIS can be found in [54].

Since the Penning trap and the electronics cannot be accessed from the outside, the complete cryogenic part of the experiment, consisting of the cryocooler with the suspended trap chamber and detection housing (Fig. 4.2(b)), has to be removed and disassembled, in order to do modifications or reparations. Therefore, for every modification, a self-developed four meter high aluminium hoist has to be assembled on top of the tower, since a permanent installation is not possible. When inserting the over 100 kilogram heavy experiment, great care has to be taken of eddy currents induced in the conductive parts of the experiment. Due to Lenz's law the magnetic field creates a counterforce which in the end will result in a force on the magnet's coils. Since these coils should never experience a force higher than 100 newton, a scale is introduced, so care can be taken in not exceeding this value. Figure 4.4 shows photographs of this procedure.

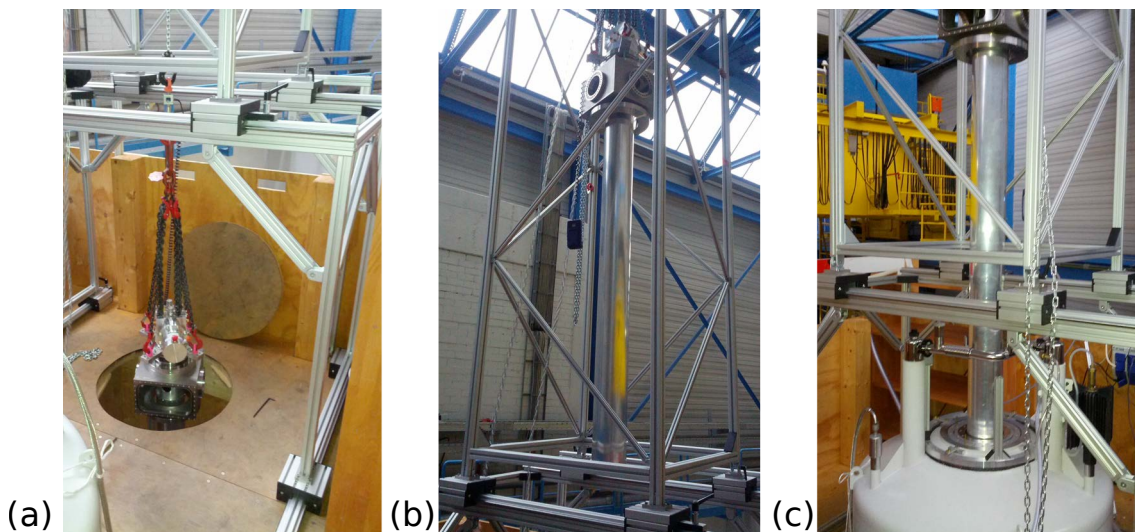


**Figure 4.4:** Procedure for inserting and removing the cryogenic parts of the experiment for reparations and modifications: (a) The cryogenic part of the experiment is stored on the intermediate floor of the wooden tower. After assembling the hoist on top of the tower, a hole in the top-floor is opened and the cryocooler with the suspended trap chamber and detection housing can be lifted. (b) After hoisting, a two axis rail is used to position the load over the center of the magnet. (c) With a high gear-ratio pulley the cryogenic part of the experiment is slowly inserted into the warm bore of the magnet.

---

## 4.2 Cryogenic Setup

---

Most of the cryogenic setup has already been described in detail in the author's Diploma thesis [52]. The cryogenic part of the experiment, as shown in figure 4.2(b), is not only for cooling the Penning trap and the electronics to a temperature of 4 kelvin – due to its massive copper pieces, it also acts as a scaffold. The cooling is provided by a SRP-82B pulse-tube cryocooler from SUMITOMO HEAVY INDUSTRIES with a cooling power at the first stage of 40 W at a temperature<sup>2</sup> of 45 K and a cooling power on the second stage of 1 W at a temperature of 4.2 K. A 705 mm long oxygen-free high thermal conductivity (OFHC) copper rod is attached to the second stage providing good thermal connection to the electronics and the trap chamber.

A set of 24 stranded copper wires with a total cross section of 240 mm<sup>2</sup> decouples the vibrations induced by the cryocooler while still maintaining thermal connection. The stranded copper wires are strained in a sandwich-like structure between indium foils and copper plates (Fig. 4.5). For optimal thermal conduction the contact area has to be as large as possible, this is assured by the indium which will fill the gaps between the different copper strands. Indium is used since it comprises a relatively good thermal conductivity with softness. Brass screws<sup>3</sup> are used to ensure a tight connection since thermal conductivity between two surfaces in cryogenic temperatures is dependent on the pressure with which they are pressed together [55].

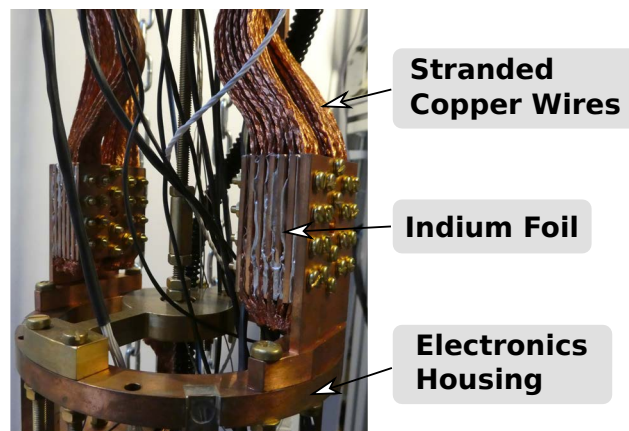


**Figure 4.5:** Photograph of the stranded copper wires that decouple the vibrations of the cryocooler while thermally connecting it with the experiment electronics. Indium foil between the solid copper surfaces and the stranded copper wires provides good thermal conduction even at low temperatures.

The trap chamber and the detection housing are encased by an aluminium tube that is connected to the first stage of the cryocooler and therefore cooled to a tem-

---

<sup>2</sup> Please note, that the temperature that can be reached is also dependent on the heat load and can therefore also be lower than 45 kelvin.

<sup>3</sup> Since the thermal expansion coefficient for brass is higher than it is for copper, the brass screws contract more than the copper parts and therefore, the connection gets more tightened when being cooled down.



---

perature of around 30 to 45 kelvin. This tube is called the 45 K shield and it is used to block the heat radiation from the room-temperature warm surroundings from impinging on the 4 kelvin cold parts. The Stefan-Boltzmann law relates the power  $P$  of the heat radiation sent from a surface to its temperature  $T$  by  $P \propto T^4$ . Adding additional shields can reduce the heat load on the cryogenic parts due to heat radiation and therefore, the aluminium tube is covered in ‘Coolcat 2’ superinsulation foil from RUAG. This is a ‘10 layer (spot welded) lay-up from double side aluminized, 6  $\mu\text{m}$  polyester film, interleaved with 10 layers polyester knit-woven spacer’ [56].

The trap chamber and the detection housing are suspended from the cryocooler during assembly and insertion. Once the cryogenic part of the experiment is put inside the magnet, it stands on a PEEK (PolyEther Ether Keton) pedestal with a low thermal conductivity of 0.25 W/(K m), on the lower flange of the magnet and it is then vibrationally decoupled from the cryocooler [52].

To further decrease the heat load on the second stage, almost all cables are either polytetrafluoroethylene (PTFE) or perfluoroalkoxy alkane (PFA) isolated constantan wires, where PTFE isolation is chosen due to the low dielectric constant. Additionally, cryogenic coaxial cables, with a brass inner conductor, a PTFE isolation and a copper-nickel (CuNi<sup>4</sup>) outer shield are used for signal lines. Further, almost all lines are thermally attached to the first stage of the cryocooler before they are thermally connected to the second stage. To provide sufficient thermal contact combined with electric isolation, ‘thermocouplers’ were built which consist of a sapphire disk against which pins are pressed and glued by silver paste to provide a good thermal connection. Additionally, the thermocouplers make the cabling more modular, hence, the detection housing and the trap chamber can be removed for inspection without the necessity of redoing the wiring.

The detection systems for axial motion detection presented in section 4.3.1 contain superconducting NbTi wires with a critical temperature of 6.5 kelvin at a magnetic field of 7 tesla. To ensure that the critical temperature is not exceeded, additional superinsulation foil covers the complete detection housing to improve the thermal shielding.

In total, the cryogenic part of the experiment consists of around 15 kilograms of copper, therefore, cooling it down to a temperature of 4 kelvin takes more than one day. A warm-up cycle would take even longer (up to several days), but can be sped up by injecting nitrogen into the vacuum or heating the trap chamber with a small heating resistor, hence resulting in the same timescale.

---

### 4.3 Detection Housing and Trap Chamber

---

The detection housing and the attached trap chamber with the double Penning trap, consisting of the spectroscopy trap ‘ST’ and the creation trap ‘CT’, are the core parts of the experiment (Fig. 4.6(a)). The housing includes the two axial resonators with

---

<sup>4</sup> CuNi alloys are not ferromagnetic and therefore can be used in the strong magnetic field.

their cryogenic amplifiers (Sec. 4.3.1); the cyclotron resonator with cryogenic amplifier and varactor diode board (Sec. 4.3.2); the cryogenic filterboards; the antenna for irradiation of the microwaves (Sec. 4.4) and the optics system (Sec. 4.3.3). The housing consists of two parallel rings that are connected by four rods containing several holes with a diameter of 2 mm separated by 14.71 mm. These holes are used to tightly connect the filterboards, the holders for the detection parts and the thermocouplers. Two cryogenic filterboards, thermally connected by a copper plate and electrically isolated by a kapton foil, are used in the system, one for the low-voltage connections, such as trap potentials and resonator lines, and one high-voltage (5 kV) filterboard for the in-trap ion creation 4.5.2. They are custom made by STAHL ELECTRONICS [57] and are further described in [18].

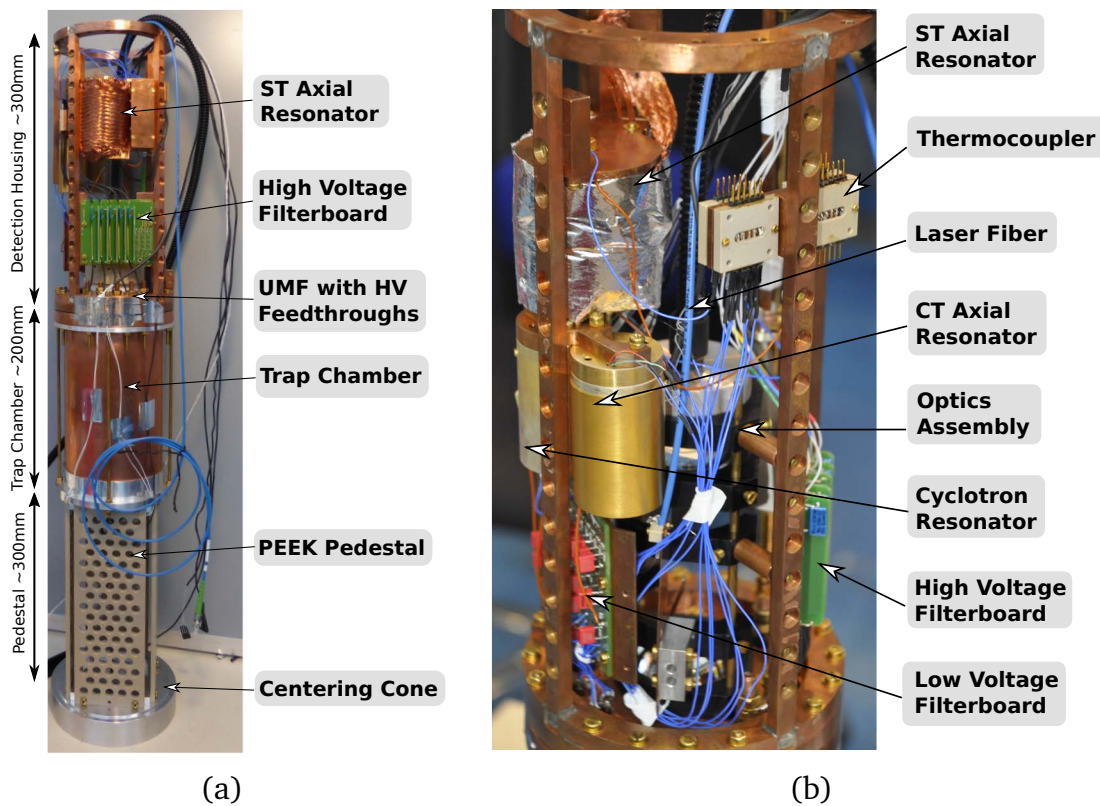


**Figure 4.6:** (a) The detection housing attached to the trap chamber mounted on the PEEK pedestal. When lowered into the warm bore of the magnet, the centering cone and its counterpart are used to align the trap chamber and therefore the Penning trap in the center of the bore. The stranded copper wires shown in figure 4.5 are not yet connected. (b) Close-up of the electronics housing from another perspective: four thermocouplers with six pins each, and all three resonators can be seen. The axial resonator in this picture is additionally wrapped in superinsulation foil. Care was taken for the wiring not to interfere with the optics assembly.

The trap chamber, a copper cylinder that houses the double Penning trap (Sec. 4.5), is attached to the lower side of the detection housing. To provide storage times

of highly charged ions in the order of weeks, the trap has to be held at ultra-high vacuum (by cryo-pumping a vacuum better than  $10^{-15}$  mbar is achieved, Sec. 5.4.1). Therefore, the vacuum inside the trap chamber is separated from the vacuum inside the magnet bore<sup>5</sup>. This is achieved on the lower end of the trap chamber by the so-called ‘cryovalve’ (4.5.2) and on the upper end of the chamber by an indium sealed copper flange called ‘UMF’<sup>6</sup>. The UMF acts as a feedthrough flange, including a quartz window for optical access (Sec. 4.3.3), five high-voltage feedthroughs for voltages in the range of several kilovolts and five four-pin low-voltage feedthroughs.

---

### 4.3.1 The Non-Destructive Ion-Motion Detection Systems

---

As described in section 3.3 non-destructive ion detection can be implemented in the form of a ‘resonator’: an inductor together with its parallel self-capacitance form a LC-circuit – when the ions motional frequency comes into resonance with the eigenfrequency  $\omega_0$  of the LC-circuit, this results in a measurable voltage drop. In ARTEMIS, these detection systems are implemented as self-wound coils in a resonator housing designed for a specific eigenfrequency  $\omega_0$  and optimized for a high quality factor<sup>7</sup>  $Q_{res}$ . More information of how to optimize these quality factors and the recent developments in superconducting resonators can be found in [47, 58].

According to equation 3.5, in order to measure the magnetic field of the Penning trap, the free cyclotron frequency is needed which cannot be measured directly, but with the Brown-Gabrielse invariance theorem it can be estimated: for this purpose all three motional frequencies have to be measured. With resonators two of these three ion motional frequencies can be measured directly, the reduced cyclotron frequency  $\omega_+$  and the axial frequency  $\omega_z$ . If both frequencies can be measured independently, the magnetron frequency  $\omega_-$  can be yielded by sideband coupling [47].

Besides the measurement of the magnetic field, the resonators used in ARTEMIS serve the purpose of cooling the ion motions in order to reach higher precisions, this so-called ‘bolometric’ cooling is presented in section 5.3. Additionally, with the axial resonators, a spectrum of the different ion species inside the trap can be created by the following relation:

$$\omega_z = \sqrt{\frac{Q C_2 U_T}{M d^2}}, \quad (4.1)$$

with the charge-to-mass ratio  $Q/M$ , the characteristic trap dimension  $d$  (Eqn. 3.2), the trap coefficient for the harmonic potential  $C_2$  and the applied trap voltage  $U_T$ . Since  $\omega_z$  can be tuned to get into resonance with the circuit, the eigenfrequency

---

<sup>5</sup> In order for the cryocooler to cool efficiently, the magnet bore vacuum should be better than  $10^{-5}$  mbar (given by the mean free path of the residual gas molecules).

<sup>6</sup> UMF is a German initialism for ‘Unterer Montageflansch’ that is used in the Mainz, CERN, GSI community.

<sup>7</sup> The quality factor of a resonator, sometimes also called ‘Q-value’, is a dimensionless number that is defined by the ratio of its frequency to its bandwidth (Sec. 3.3).



of the axial resonator has only to be designed coarsely. Additionally, by tuning the voltage, ions with different charge-to-mass ratios come into resonance with the resonator and therefore, make it possible to record a spectrum where ions with different charge-to-mass ratios can be distinguished (Sec. 5.1.2).

ARTEMIS comprises three resonators: two axial resonators (Sec. 4.3.1) connected to the creation trap (ARES CT)<sup>8</sup> and the spectroscopy trap (ARES ST) and one cyclotron resonator (Sec. 4.3.2) for measuring the reduced cyclotron frequency in the spectroscopy trap (CRES)<sup>9</sup>. The resonators mainly differ due to their geometrical designs (helical or toroidal, amount of wirings, ...), their wire material (superconducting or non-superconducting) and their cryogenic amplifier design – still, all amplifiers are biased by the BS 1-10 cryo from STAHL ELECTRONICS. A comparison of the properties for the three resonators can be found in table 4.1 and figure 4.7 shows photographs of their coils.

**Table 4.1:** Properties of the three resonators used.

	ARES CT	ARES ST	CRES
Geometry	Helical	Toroidal	Helical
Eigenfrequency at 4 K	$2\pi \times 737$ kHz	$2\pi \times 694.5$ kHz	$\sim 2\pi \times 36$ MHz
Q-Value	900	900	50
Wire Diameter	0.075 mm	0.075 mm	1.5 mm
Wire Material	Niobium-Titanium	Niobium-Titanium	Copper
Windings	300	800	10.5
Inductance	$\sim 3$ mH	$\sim 2.4$ mH	725 nH
Housing [ $\varnothing \times$ Height]	33 mm $\times$ 44 mm	48 mm $\times$ 40 mm	33 mm $\times$ 44 mm
References	[18]	[59]	[60]
Gate Voltages	-3.9 V	-1.6 V, -0.55 V, +1.16 V	-3.8 V
Current Bias <sub>1</sub>	+2.9 mA	+2.3 mA	+3.0 mA
Current Bias <sub>2</sub>	-1.8 mA	+1.8 mA	-2.2 mA

### Superconducting Resonators

The two axial resonators both consist of a superconducting niobium-titanium wire (NbTi wire) coil wound around a PTFE core in two different geometries, cylindrical for the ARES CT and toroidal for the ARES ST. Superconducting wires, which have zero electrical resistance when cooled below their critical temperature, are used in order to get a lower parasitic capacitance and therefore higher quality factors. Due to the fact that NbTi is a type-II superconductor and the resonators are placed in a magnetic field of several tesla, they need to be cooled below the critical temperature for the respective magnetic field strength (NbTi has a critical temperature of 6.5 kelvin

<sup>8</sup> ARES is an abbreviation for Axial RESonator.

<sup>9</sup> CRES is an abbreviation for Cyclotron RESonator.

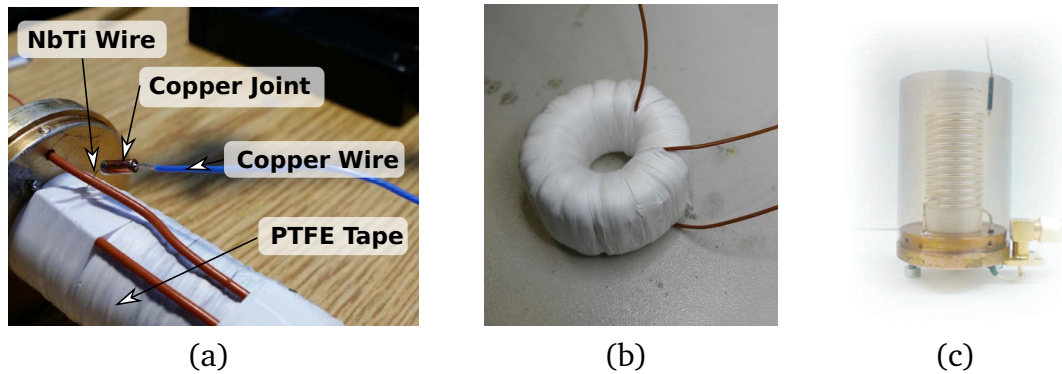


**Figure 4.7:** Photographs of the coils of the three resonators. (a) ARES CT: around the cylindrical PTFE core the NbTi wire is wound in helices and then tightly wrapped with PTFE tape. The soldering joint between the NbTi and the copper wire can be seen (Sec. 4.3.1). (b) ARES ST: around a toroidal PTFE core the NbTi wire is wound and then tightly wrapped with PTFE tape. (c) CRES: the cyclotron resonator with the helical wire wound around a PTFE core can be seen, the housing is added schematically with low opacity to see the coil.

at a magnetic field of 7 tesla). In order to get a measurable resonance, the wire has to be completely thermalized below this critical temperature – even a small part of the wire being non-superconducting results in distraction of the resonance spectrum due to the high impedance and therefore, care has to be taken in order to reach this goal. In both resonators this is achieved by tightly wrapping PTFE tape around the coil, assuring a proper thermal connection of the wire, since, once superconductivity is reached, NbTi changes from being a mediocre thermal conductor to a thermal insulator. Thus, to prevent a piece/section of the wire from being non-superconducting, the tight PTFE tape, although having a low thermal conductivity, will still maintain a proper thermal conduction. When soldering NbTi to copper care has to be taken, since joints can easily break. Therefore, a special joint was made: in a copper tube with a hole of a few 100  $\mu\text{m}$  diameter both wires are inserted from opposing sides and the tube is heated; when applying the solder, it fills the tube due to capillary forces.

Nevertheless, thermalization of the complete coil to temperatures of 4 kelvin takes more time than it does for the rest of the setup: there are two temperature sensors attached to the second stage of the experiment, one on top of the trap chamber and one on its bottom and their temperature is measured every 10 seconds. During a cooldown they only deviate in the order of a few hundreds of millikelvin, giving an indicator that thermalization between the copper parts happens at maximum on the time scale of seconds. Nevertheless, during a cooldown of the experiment the resonance curve of the ARES ST was monitored and its quality factor is shown versus one of these temperatures in figure 4.8 – it can be seen that the Q-value of the resonator, which is an indicator for the temperature of the superconducting coil, rises several hours *after* the whole experiment is cooled below the critical temperature.

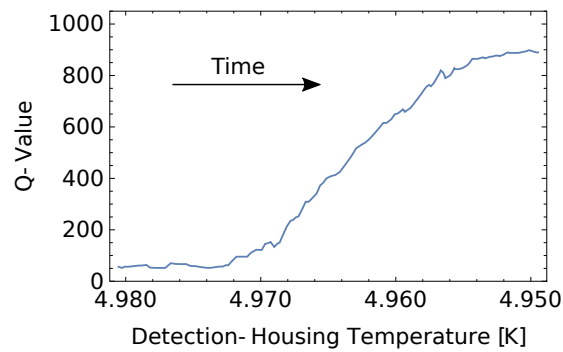


**Figure 4.8:** During a cooldown the resonance curve of the ARES ST is monitored. The corresponding quality factors are shown versus the decreasing temperature of the detection housing. Since the temperature of the housing is already more than 1 kelvin below the critical temperature (6.5 kelvin) when the coil becomes superconducting (and therefore the Q-value rises), this gives an indication of the longer thermalization time needed for the superconducting wire of the resonator, compared to the thermalization of the rest of the experiment.

The quality factor of a superconducting coil is also dependent on the magnetic field it is exposed to: a type-II superconductor in a magnetic field between the lower and the higher critical field strength is in the so-called ‘Shubnikov-phase’. The magnetic field lines can penetrate the surface and create ‘vortices’, where these vortices give rise to a finite resistance in the wire, leading to signal loss and therefore a decrease in the Q-value.

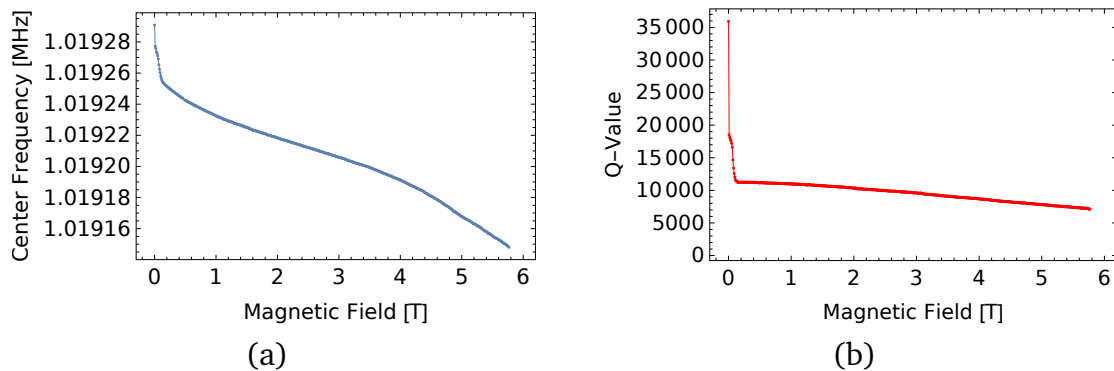


**Figure 4.9:** Measurement of the behavior of a superconducting resonator at HILITE: the resonator was located in a magnetic field that was ramped from 0 to 6 tesla and for every step a resonance curve was taken and evaluated. (a) Measured center resonance frequency as a function of the applied magnetic field. Already at a magnetic field of 120 millitesla a shift of more than 30 hertz occurs. (b) The respective Q-values for the resonator as a function of the magnetic field, after a few hundred millitesla the quality factor already decreases from 35 000 to 10 000.

A respective measurement was conducted at the ‘High Intensity Laser Ion Trap Experiment’ (HILITE, [61]): the setup consists, amongst others, of a cryocooler

---

with a thermal connection to the center of a superconducting magnet with a warm horizontal bore. This ‘dry’ (cooled by a cryocooler instead of liquid helium) superconducting magnet has additionally the advantage that the magnetic field can be ramped stepwise up to 6 tesla. The ARES ST was located in the center of this magnet and resonance spectra were taken by a spectrum analyzer at different magnetic field strengths. Figure 4.9 shows the effect of an external magnetic field on the center frequency and the quality factor of a superconducting resonator – already at a magnetic field of 120 millitesla the center frequency shifts by more than 30 hertz and the quality factor decreases severely. More results of this experiment, together with theoretical explanations, can be found in [59].

---

### Creation Trap Axial Resonator (ARES CT)

---

The axial resonator connected to the creation trap consists of a NbTi wire with around 300 windings on a PTFE body in a helical geometry. It is housed in a silver- and gold-plated copper housing. It was built by M. Shaaban with the a cryogenic amplifier developed by M. Hüllen [60] after the design from S. Stahl [49]. The amplifier uses two transistors, a 3SK166 from SONY for amplification and a NE3508 from NEC for impedance matching which are both gallium-arsenide (GaAs) transistors since standard Si-semiconductor transistors are not functional at cryogenic temperatures due to charge-carrier freezing below a temperature of 10 kelvin.

The ARES CT is connected to electrode C13 (for an overview of the electrode numbering, see section 4.5), this makes it possible to measure the axial frequency not only in the trap of C14 being the ring electrode, but also when ions are stored in the trap of C12. This is shown in section 5.4.3.

Figure 4.10(a) shows the thermal noise resonance spectrum recorded by the KEYSIGHT N9000B-CXA spectrum analyzer, yielding an eigenfrequency of the ARES CT of  $2\pi \times 737.5$  kHz with a corresponding Q-value of 900.

---

### Spectroscopy Trap Axial Resonator (ARES ST)

---

The axial resonator connected to the spectroscopy trap consists of a NbTi wire on a PTFE body in a toroidal geometry – in contrast to the other two resonators the 800 windings are wound around a ring with a rectangular cross-section. Therefore, it is an improvement over the axial resonator from N.P.M. Brantjes [62] since it comprises a more compact design with a higher Q-value. It is housed in a silver- and gold-plated copper housing. Together with the amplifier it was built by M.S. Ebrahimi [59] following the design from the BASE collaboration at CERN [58]. The amplifier is similar to the previous one which was used in the 2015 measurement time [18].

Figure 4.10(b) shows the excited<sup>10</sup> resonance spectrum of the ARES ST, yielding an eigenfrequency of the ARES ST of  $2\pi \times 694.5$  kHz with a corresponding Q-value of 900.

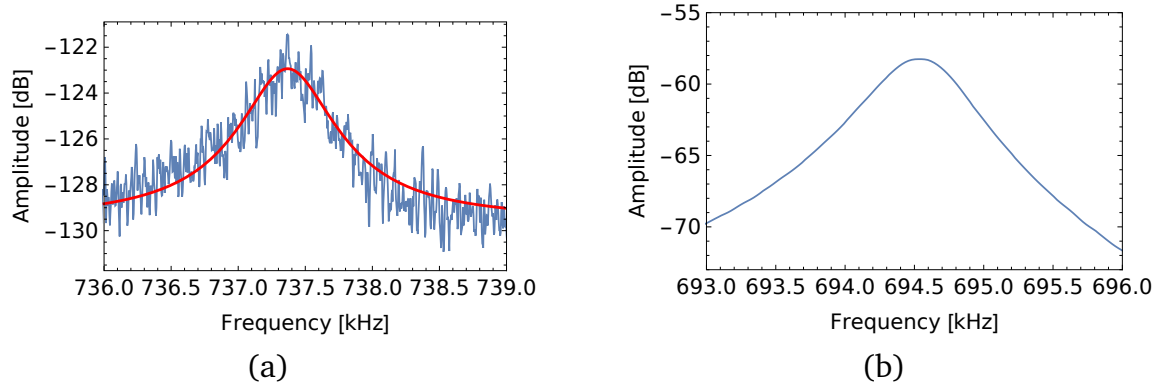


**Figure 4.10:** (a) Thermal noise spectrum of the axial resonator in the creation trap (blue, with fit in red). The center frequency is around  $2\pi \times 737.5$  kHz, with a Q-value of 900. (b) Excited resonance curve for the axial resonator in the spectroscopy trap, the center frequency is at  $2\pi \times 694.5$  kHz, the Q-value around 900.

### 4.3.2 Cyclotron Resonator (CRES)

The cyclotron resonator (CRES) connected to the split electrode S4 is designed to measure the reduced cyclotron frequency of  $^{40}\text{Ar}^{13+}$  in the spectroscopy trap which is around  $2\pi \times 35$  megahertz at a magnetic field of 7 tesla. It was developed and built by M. Hüllen [60] and consists of a silver-coated copper wire with a diameter of 1.5 mm and 10.5 windings on a PTFE body. The housing which is made of silver- and gold-plated copper, and the amplifier are similar to the housing and the amplifier in the ARES CT.

Building a resonator with a specific resonance frequency is hard to achieve, since the frequency depends on many parameters (for example the parasitic capacities) and some of them cannot be controlled sufficiently. As the cyclotron frequency of  $^{40}\text{Ar}^{13+}$  can only be changed by changing the magnetic field, it is necessary to tune the resonance frequency of the resonator: for example, by an additional superconducting wire, adding a tunable resistance by warming parts of it above the critical temperature [58]; by adding and removing additional capacitances via a switch; or by adding tunable capacitance diodes, so-called varactor diodes<sup>11</sup>. Although any

<sup>10</sup> This measurement was performed with the RIGOL DSA-815TG spectrum analyzer which, due to a high internal background noise, is not capable of measuring the thermal noise and therefore, the resonator has to be excited externally via the so-called tracking generator function. Unfortunately, a transistor in the amplifier board broke during the 2016 measurement time before it was possible to measure the thermal noise spectrum with the KEYSIGHT N9000B-CXA spectrum analyzer.

<sup>11</sup> From varactor=‘variable reactor’, sometimes also referred as varicap=‘variable capacitance’.

diode can act as a varactor diode, special ones dedicated to frequency tuning of LC-circuits are available: by applying an increasing reverse voltage, the capacitance of a p-n junction in a diode decreases [63]. In ARTEMIS a MA46H202 varactor diode from MACOM is used, with a tunable capacitance from 2.2 to 3.3 pF.

By adding a tunable capacitance  $C_{\text{var}}$  in parallel to an already existing capacitance  $C$  of the LC-circuit, the total voltage-dependent capacitance is then given by:

$$C(U_{\text{var}}) = C + C_{\text{var}}(U_{\text{var}}), \quad (4.2)$$

which leads to a tunable resonance frequency of the resonator:

$$\omega_0(U_{\text{var}}) = \frac{1}{\sqrt{L(C + C_{\text{var}}(U_{\text{var}}))}}. \quad (4.3)$$

Every varactor diode has a small series resistance and therefore, a Q-value [64] which limits the total Q-value that can be achieved by the complete system to

$$\frac{1}{Q_{\text{res}}} = \frac{1}{Q_{\text{coil}}} + \frac{1}{Q_{\text{var}}}, \quad (4.4)$$

but with  $Q_{\text{var}} = 2000$  ([65], at room-temperature – at cryogenic temperatures of 4 kelvin this value is approximately 1000) and  $Q_{\text{coil}} \approx 100$  at room-temperature the effects on the CRES are negligible.

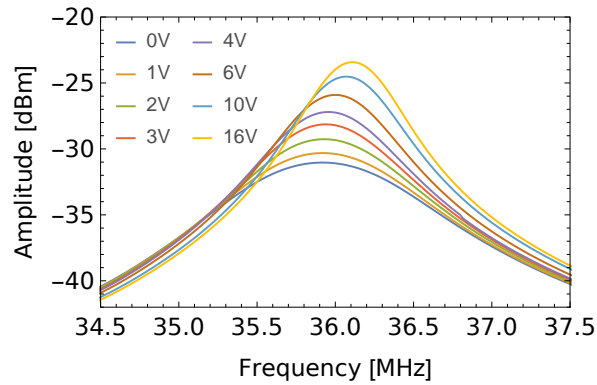


**Figure 4.11:** Excited resonance curves of the cyclotron resonator at a temperature of 4 kelvin in a magnetic field of several tesla and with different varactor diode bias voltages. Whereas in a similar room-temperature experiment the center frequency could be shifted by several megahertz, here only a shift of less than 1 megahertz has been achieved.

To combine the varactor diode with the cyclotron resonator, a high-frequency board was produced (the wiring can be found in figure A.3) and deployed in ARTEMIS for the 2016 measurement time. However, it was discovered that by combining strong magnetic fields with cryogenic temperatures the varactor diode is not fully functional anymore: figure 4.11 was recorded with the CRES at a temperature of 4 kelvin, located near the center of the trap and therefore in a magnetic

---

field of several tesla. In a previous test at room-temperature the tunable frequency range of the resonator with the varactor diode was sufficient to reach the desired  $2\pi \times 35$  megahertz; but in figure 4.11, at cryogenic temperatures, it can be seen that for smaller varactor diode bias voltages, there is almost no frequency shift. To investigate this behavior, an experiment was conducted and its results are reported in section 4.3.2.

---

### Varactor Diode Frequency Shift

---

To investigate the behavior of a varactor diode at cryogenic temperatures *and* strong magnetic fields an experiment was conducted at HILITE, a LC-circuit (Fig. 4.12) was soldered on a small testboard together with a MACOM MA46H202 varactor diode connected in parallel to the capacitance. The board was placed in the center of the magnet so different combinations of temperatures and magnetic fields could be tested. The magnetic field was ramped in steps of 0.5 tesla and after each step, an excited resonance spectrum was taken by the RIGOL DSA-815TG spectrum analyzer. These spectra were evaluated and their center resonance frequency as well as the corresponding Q-values were determined.

Figure 4.13(a) shows the center resonance frequencies of the board at room-temperature (300 kelvin) for different varactor diode bias voltages and for different magnetic field strengths; the result meets the expectations from the datasheet: for each applied bias voltage there is no shift in frequency when different magnetic fields are applied, and since the capacitance of the varactor diode is not linearly dependent on the applied bias voltage, there are stronger shifts in the center resonance frequency between the steps at lower bias voltages than between the steps at higher bias voltages.

The same measurement was performed at cryogenic temperatures of 4 kelvin. Figure 4.13(b) shows the center resonance frequency for different magnetic fields. Already at a field strength of 2.5 tesla, when applying a bias voltage of 1 volt, the frequency starts to shift to higher values. For higher magnetic fields this effect becomes even stronger until the resonance is not detectable anymore (Figure 4.13(d)) and the fit-routine gives a false value, thus, creating the artifact of the too high values. Again, this effect is only visible by the *combination of cryogenic temperatures and high magnetic fields*, as demonstrated by comparing figure 4.13(c) with figure 4.13(d), where both measurements were done at cryogenic temperatures: at zero magnetic field the occurrence of the resonance spectra for different bias voltages follows the expectations, but with the additional strong magnetic field of 6 tesla, only when higher bias voltages are applied, resonance spectra are visible.

To test the assumption that this effect is caused by the dislocation of the charge carriers in the varactor diode due to the magnetic field, the testboard and therefore the varactor diode housing was turned by  $90^\circ$ : figure 4.13(e) shows the quality factor of the resonance spectra for different bias voltages, when the diode housing was



orthogonal to the magnetic field lines, versus the magnetic field; for figure 4.13(f)<sup>12</sup> the diode housing was parallel to the magnetic field (both measurements were conducted at cryogenic temperatures, for comparison with a room-temperature measurement of the Q-value versus the magnetic field, see figure 4.14(a)). Since the difference between both figures is not severe and other effects, such as different parasitic capacitances between the different measurement setups would also change the result, this measurement cannot corroborate this assumption.

Another attempt was to investigate the exact dependence of the varactor diode on the temperature, therefore the cryocooler was switched off and resonance spectra were measured continuously during the warm-up. Figure 4.14(b) to 4.14(f) show the Q-values as a function of the temperature for magnetic fields of 0, 3 and 6 tesla. At around a temperature of 50 kelvin the quality factors reach the highest value, this is due to the rise in conductivity of the parts at low temperature. For strong magnetic fields at temperatures around 30 kelvin already a drop in the Q-values occurs and below 10 kelvin high bias voltages are needed to maintain visibility of the resonance curves.

Altogether, in the case of ARTEMIS, in order to get a sufficient range for the frequency shift of the cyclotron resonator with a varactor diode, the diode either has to be placed in a region of very low magnetic fields, or its temperature has to be above 30 kelvin. The solution for the next measurement time is a custom-made varactor diode board from STAHL ELECTRONICS, where the varactor diode is mounted on a weakly thermally coupled board that can be heated by a small current and therefore, its temperature will be above the critical region without influencing the cryogenic temperatures of the detection housing.

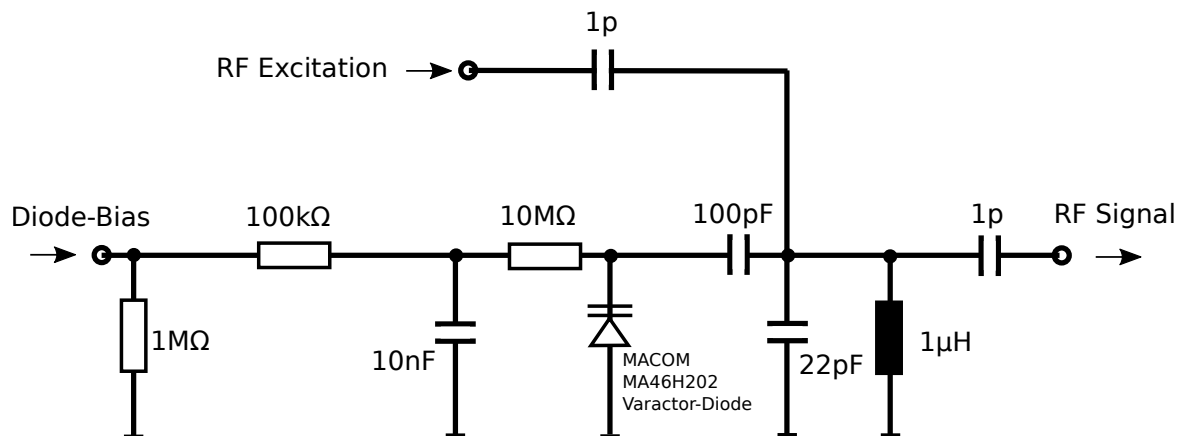
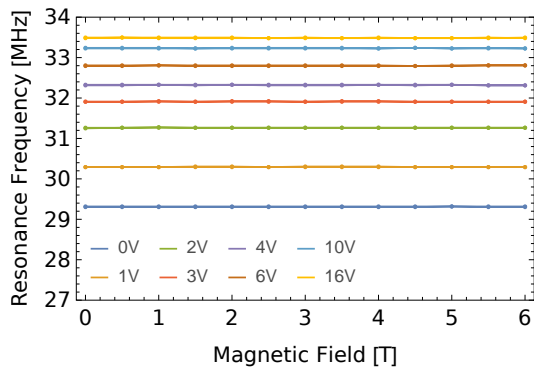


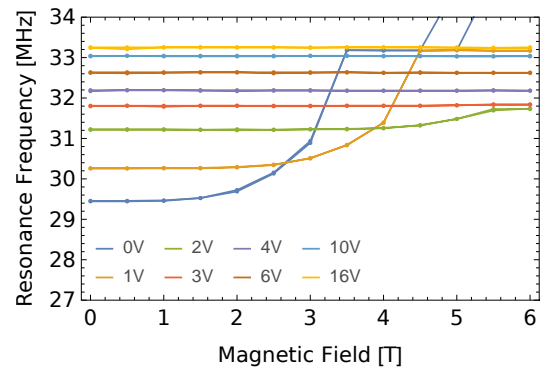
**Figure 4.12:** Equivalent Circuit of the varactor diode test board.

<sup>12</sup> Figure 4.13(f) is the only measurement that was conducted with the diode housing turned by 90° and therefore parallel to the magnetic field lines, all other measurements in this section were performed with the diode housing being orthogonal to the magnetic field lines.

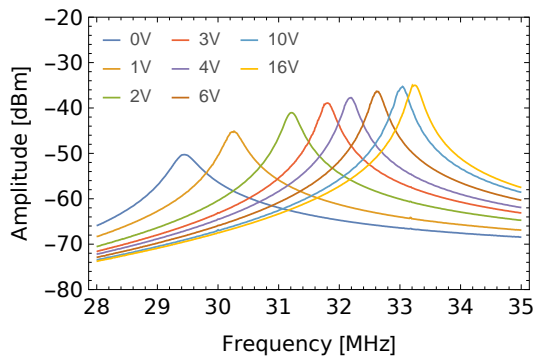




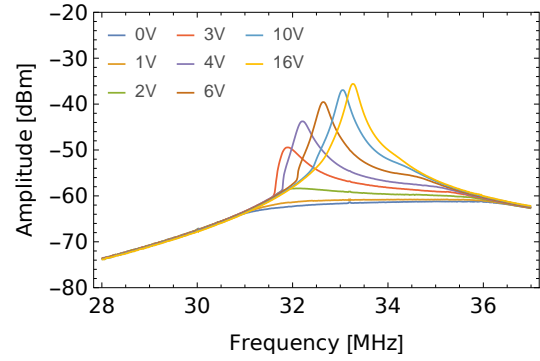
(a) Center resonance frequencies of a test circuit for the varactor diode at a temperature of **300 K** versus the magnetic field for different bias voltages; the magnetic field is ramped up and down.



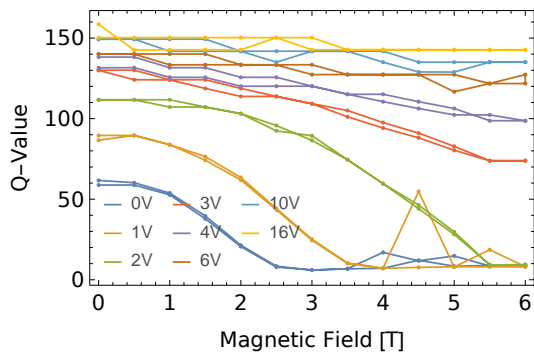
(b) Center resonance frequencies of a test circuit for the varactor diode at a temperature of **4 K** versus the magnetic field for different bias voltages; the magnetic field is ramped up and down.



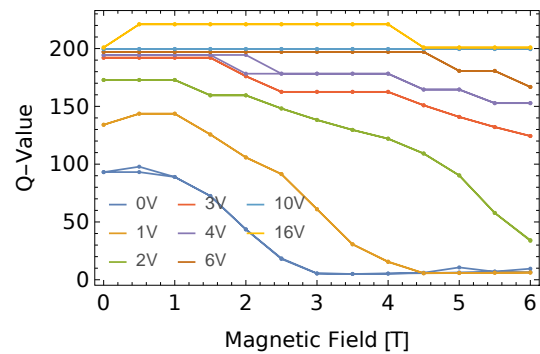
(c) Resonance spectra for different bias voltages at a temperature of **4 K** and a magnetic field of **0 T**.



(d) Resonance spectra for different bias voltages at a temperature of **4 K** and a magnetic field of **6 T**.

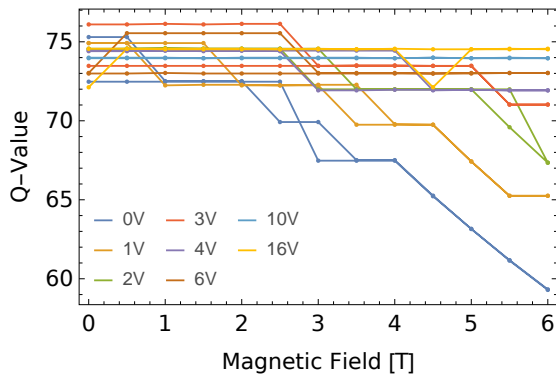


(e) Q-value of the resonance spectra for different bias voltages at a temperature of **4 K**, the diode housing is oriented **orthogonal** with respect to the magnetic field lines, the magnetic field is ramped up and down.

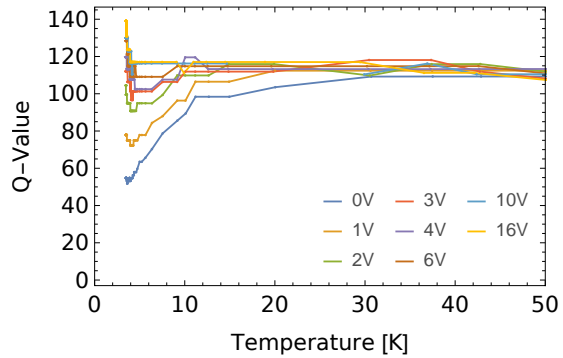


(f) Q-value of the resonance spectra for different bias voltages at a temperature of **4 K**, the diode housing is oriented **parallel** with respect to the magnetic field lines, the magnetic field is ramped up and down.

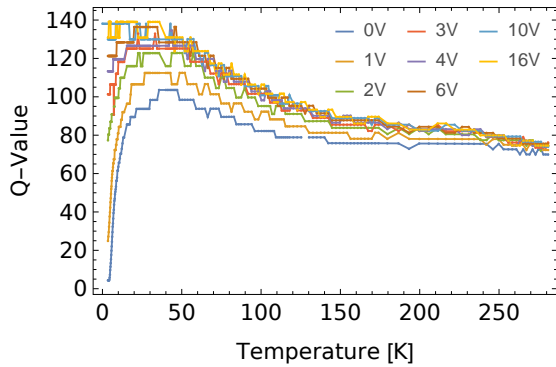
**Figure 4.13:** Behavior of the varactor diode for diff. temperatures and magnetic fields.



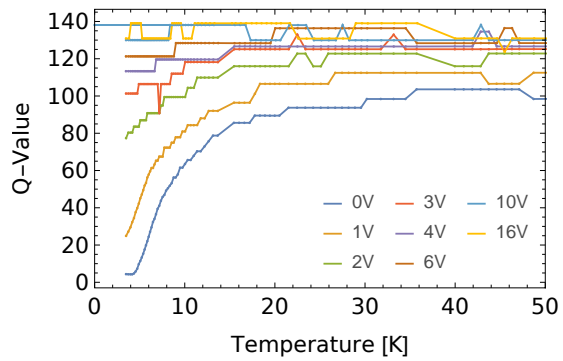
(a) Q-value of the resonance spectra for different bias voltages at a temperature of **300 K**, the magnetic field is ramped up and down.



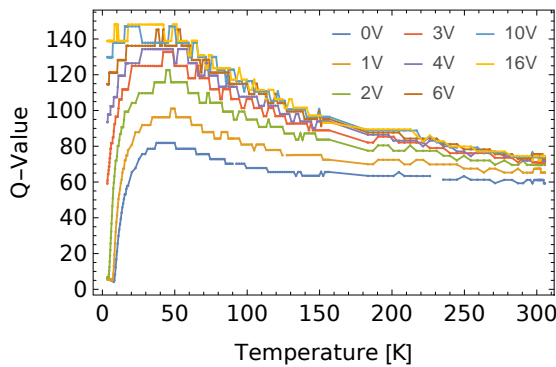
(b) Q-value of the resonance spectra for different bias voltages at a magnetic field of **0 T** (for low temperatures).



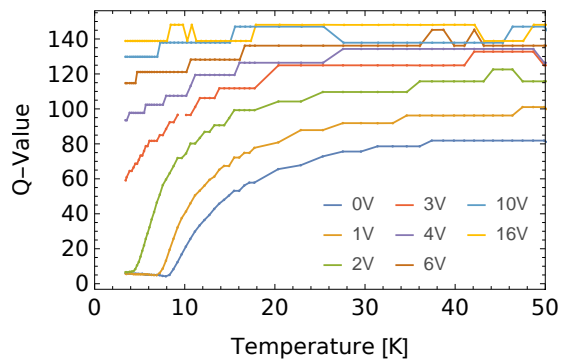
(c) Q-value of the resonance spectra for different bias voltages at a magnetic field of **3 T**.



(d) Q-value of the resonance spectra for different bias voltages at a magnetic field of **3 T** (for low temperatures).



(e) Q-value of the resonance spectra for different bias voltages at a magnetic field of **6 T**.



(f) Q-value of the resonance spectra for different bias voltages at a magnetic field of **6 T** (for low temperatures).

**Figure 4.14:** Behavior of the varactor diode for diff. temperatures and magnetic fields.

### 4.3.3 Laser and the Optical Detection System

For the double-resonance spectroscopy of  $^{40}\text{Ar}^{13+}$  (Sec. 2.3), ARTEMIS utilizes a laser with a wavelength of 441 nm. This laser system and the additional optics were mainly built and developed by A. Martin [50]. This section gives a short introduction into the used laser setup and afterwards a brief overview of the optical detection system is given, more details can be found in [50].

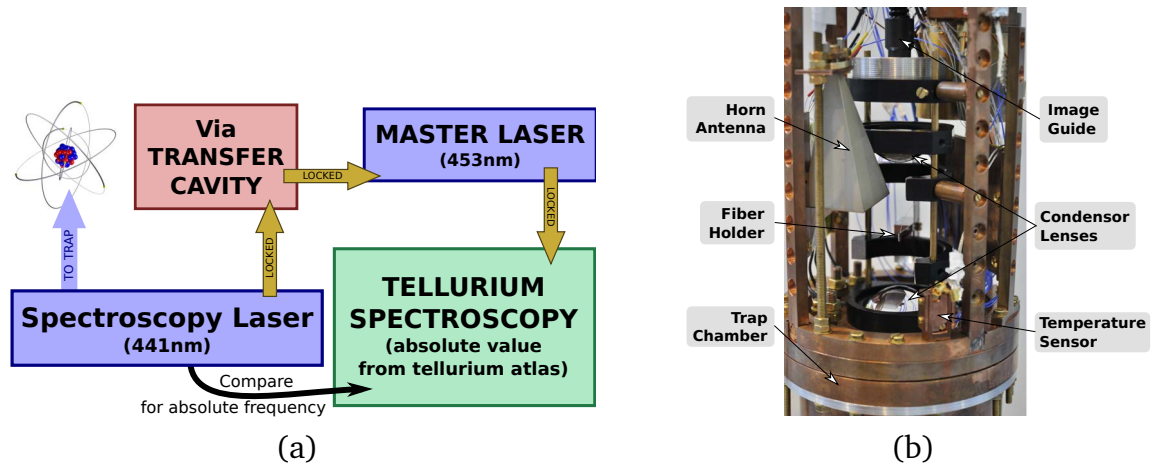


**Figure 4.15:** (a) Scheme of the locking chain of the laser. The commercial external cavity diode laser (ECDL), the ‘spectroscopy laser’, is frequency locked via a transfer cavity to the self-built ECDL, the ‘master laser’ which itself is locked on one of the well known spectroscopic lines of tellurium. (b) Photograph of the optics holder mounted in the electronics housing, a black-coated modular aluminium frame retains the two condenser lenses and a holder for the bare optical fiber. In order not to block the microwave radiation from the horn antenna, the aluminium frame is cut on one side.

Figure 4.15(a) shows a schematic view of the principle of the laser locking chain, whereas figure 4.16 gives an overview of the beam paths and the optical parts. The laser system consists of two diode lasers: the so-called spectroscopy laser TOPTICA DL 100 pro, a commercial external cavity diode laser (ECDL) with a wavelength of 441 nm; and the master laser, also a ECDL, at a wavelength of 453 nm, which was built by A. Martin and P. Baus and is described in [50] and [66]. For frequency locking the system comprises a transfer cavity and a tellurium spectrometer: an oven heats a tellurium cell to a temperature of around 500 kelvin making the solid tellurium optically accessible in the vapor phase. To this cell a Doppler-free spectroscopy, with a probe beam and a saturation beam, is carried out [67]. The detailed knowledge of the spectrum of tellurium (the so-called ‘tellurium atlas’) is then used for frequency stabilization and as an absolute frequency reference. Therefore, the master laser is locked on one of the Lamb dips to stabilize the frequency and with the help of a transfer cavity the spectroscopy laser is then locked to the master laser. This is achieved by locking the length of the transfer cavity to the frequency of the master

laser, whereas the light of the spectroscopy laser is frequency shifted by a double pass acousto-optic modulator (AOM) and locked to another mode of the same transfer cavity and by this is locked to the master laser. The spectroscopy laser's absolute frequency can then also be determined by direct comparison with the tellurium atlas. Finally, the frequency controlled laser light is coupled into a fiber leading to the experiment.

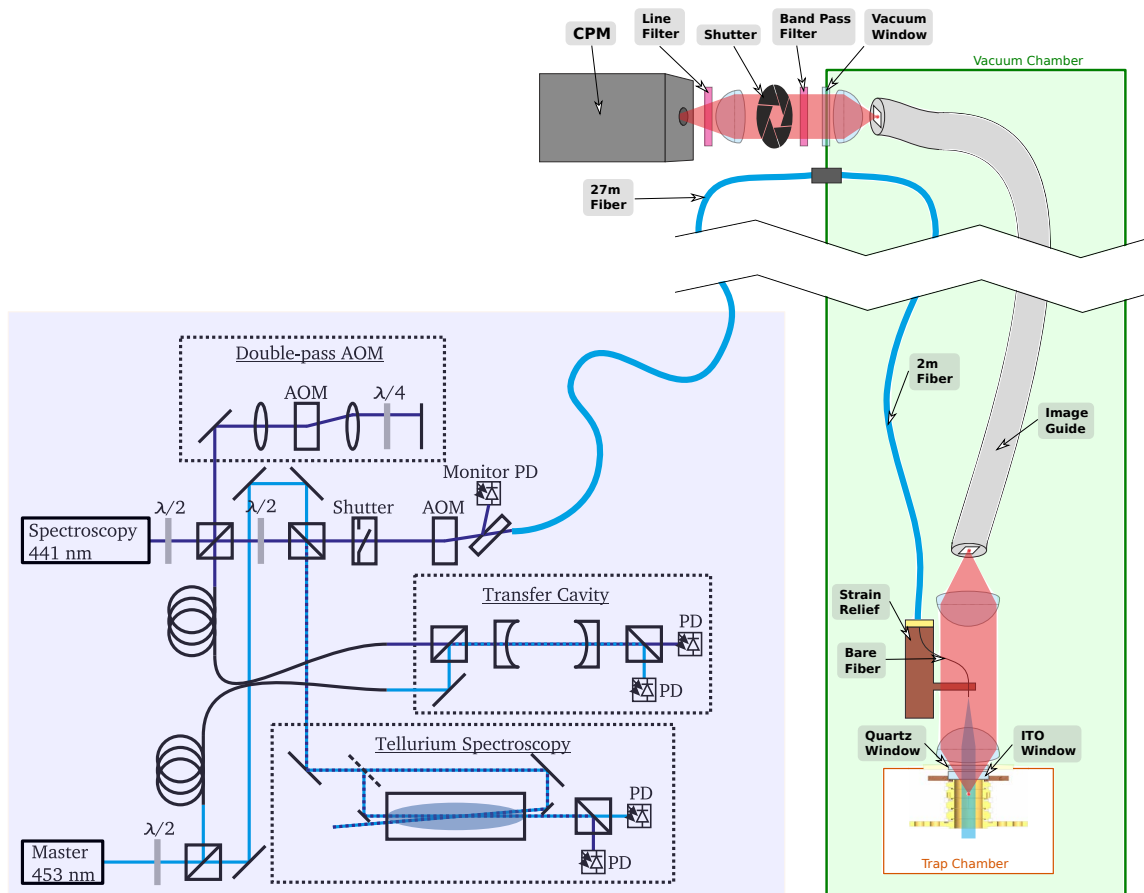


**Figure 4.16:** Scheme of the laser system (blue) and the optical coupling to the trap (green). The laser system provides the laser light at a wavelength of 441 nm which is transmitted through a 27 meter long fiber, a vacuum feedthrough and another 2 meter long fiber before it is irradiated into the trap for ion excitation. The fluorescence light of the ions is then transmitted via a fiber bundle (image guide) and finally focused on a photon counter (CPM). Parts of the figure are taken from [50].

Figure 4.16 shows a detailed scheme of the laser system together with the optical detection system. The laser light, produced in the laser lab beneath the HiTRAP-platform, is transmitted to the experiment through a 27 meter long fiber which is connected to a vacuum feedthrough which is again connected to a 2 meter fiber in the vacuum chamber that is cut at the end with the bare fiber taken out of its cover. This few centimeters long bare fiber is bent and the end glued (the tip pointing at the trap chamber) to a slim copper slab reaching into the path of the fluorescence-light

---

beam. The laser light from the fiber is then collimated by the lower aspheric lens. After transmission through the quartz window (separating the trap chamber vacuum from the magnet bore vacuum) and the ITO (the indium tin oxide-coated window used as an endcap electrode, Sec. 4.5.1) the ion cloud is illuminated by a beam with a diameter of 3 millimeter. Figure 4.15(b) shows a photograph of the optical system on top of the trap chamber, showing the bare fiber and the lenses.

The fluorescence light emitted by the ions, transmitted again through the ITO and the quartz window, is collimated by the lower aspheric lens. Although a small fraction of this light is blocked by the slab holding the fiber, this is minimized due to the very thin slab which is an improvement to the prism-holder design that was used before [18]. The collimated light is then focused by the upper aspheric lens on the tip of a so-called ‘image-guide’: a fiber bundle consisting of  $72 \times 72$  fibers on an area of  $4 \text{ mm} \times 4 \text{ mm}$  which enables the transmission of an image of the ion cloud. After this light got transmitted, it is collimated by an aspheric lens on top of the magnet, transmitted through a vacuum window and coarsely purified in wavelength by a band pass filter with a bandwidth of 10 nm around a center wavelength of 440 nm. After an electrical shutter and after focusing the light with another lens, it is finely purified by a line filter with a bandwidth of 1.7 nm at the center wavelength of 441 nm and finally detected by a CPM photon counter MP-984 from EXCELITAS. CPM stands for channeltron photo-multiplier, consisting of a bialkali photocathode that emits electrons when being impinged by a photon. These electrons are then multiplied by a photomultiplier tube (after an electron hits the wall, further secondary electrons are emitted and accelerated to the next part of the tube where they again hit the wall, releasing more electrons – the secondary electrons increase exponentially). For additional spatial resolution, the CPM can be exchanged for the ImagEM X2 EM-CCD camera from HAMAMATSU.

---

#### 4.4 The 65 GHz Microwave System

---

Together with the laser light probing the fine-structure transition, tunable microwaves are irradiated into the trap in order to measure the Zeeman shift via double-resonance spectroscopy (Sec. 2.3). Therefore, microwaves with a frequency  $\nu_L$  of around 65 gigahertz for the  $2^2P_{1/2}$  transition and around 130 gigahertz for the  $2^2P_{3/2}$  transition are needed. In this work a system for producing and transmitting the microwaves with a frequency of around 65 gigahertz was designed, tested and implemented into the ARTEMIS setup. This section gives an overview of the system and its adaptation to the experiment’s requirements, starting with the overall design, every part used in the actual design is introduced and explained and finally, measurements that were conducted in a tabletop experiment are reported.

---

#### 4.4.1 Previous Considerations

---

The microwave system was designed to fulfill the following requirements:

- **Low Thermal Conductivity**

Since the high thermal conductivity of copper and aluminum would create too much heat-load on the cryogenic stage of the experiment, at least some parts of the transmission line have to consist of a material with low thermal conductivity.

- **Low Loss Transmission Line**

Due to the long distance of more than 1.5 meter between the microwave source and the trap chamber, the transmission line should comprise low energy loss.

- **Constructional Restrictions**

Between the vacuum window on top of the magnet and the inner part of the 45 K shield, there is only a small passage with a lot of chicanes, requiring an easily bendable transmission line with small bending radii.

- **Leak-Tight Vacuum Feedthrough**

A commercial vacuum feedthrough for microwave transmission lines has to be available.

- **Magnetic Field**

The high magnetic field of several tesla forbids the usage of ferromagnetic materials, for example nickel diffusion barriers that are needed for gold plating, additionally, stainless steels can only be used if they are austenitic.

There are two types of adequate transmission lines, the rectangular waveguide and the coaxial cable which both have advantages and disadvantages (Sec. 4.4.4). On the one hand, a standard rectangular waveguide has very low losses in signal strength, approximately an attenuation per meter of 1.7-3.2 dB/m, but this comes at the price of a limited bendability and a relatively large surface area which, combined with the fact that most waveguides are made of either copper or aluminum, results in a high thermal conduction.

On the other hand a coaxial cable is more flexible and can be made of many different material layers such that the thermal conductivity can be minimized without decreasing the transmissibility. But the loss in signal strength is already higher due to the dielectric insulator, with an approximate attenuation per meter of 14 dB/m. Additionally, for coaxial cables vacuum feedthroughs are commercially available, whereas in order to use horn antennas the TE<sub>10</sub> mode (Sec. 4.4.4) and therefore a waveguide is needed.

By combining both types of transmission lines, the benefits of both designs can be achieved. In the end, a so-called hybrid design was developed. The next sections give an overview of the idea and all the parts used. By conducting a tabletop experiment the overall assembly and the individual parts were tested.

---

## 4.4.2 Hybrid Design

---

Tunable microwave sources up to frequencies of 65 gigahertz are expensive and it is nevertheless not necessary to have a tunable range over several tens of gigahertz since a range of  $\pm 0.5$  GHz around the center frequency  $\nu_L$  is sufficient. Therefore, a microwave source capable of creating frequencies up to 20 gigahertz is deployed (Sec. 4.4.3), linked with a frequency counter for monitoring the output frequency and amplitude, and is connected to a frequency multiplier by a high-frequency SMA coaxial cable<sup>13</sup>. This active ‘quadrupler’ (Sec. 4.4.7) multiplies the frequency by the factor of four, resulting in a tunable frequency range between 64 and 66 gigahertz with an output power of 10 dBm. Due to the high cost of a tunable amplifier but in order to still be variable in power, an additional high-gain (20 dB) amplifier with a mechanical tunable attenuator (Sec. 4.4.9) can be used, yielding a total power tunable by almost 50 dB.

With the help of a waveguide-to-coax adapter (Sec. 4.4.5) the  $TE_{10}$  mode, transmitted in the waveguide, is converted into a TEM mode that can be transmitted by coaxial cables (Sec. 4.4.4) and a short coaxial cable is connected to the vacuum feedthrough (Sec. 4.4.6). On the vacuum side a special cryogenic non-magnetic coax cable is used (Sec. 4.4.4). Due to its flexibility it can easily be threaded through the difficult geometry on top of the warm bore and due to its low thermal conductivity it connects the room-temperature part with the cryogenic part without creating too much heat-load. Although it is a high-performance cable, a waveguide still represents a better choice in terms of loss and therefore, for the last meter of the transmission line, a coax-to-waveguide adapter and then again a waveguide is used. This waveguide is made of OFHC copper without gold-plating since gold-plating would have required a magnetic nickel-diffusion barrier. Additionally, the waveguide is slightly bent, so the center of the following high gain horn antenna (Sec. 4.4.10) is pointing in the direction of the ions.

---

## 4.4.3 Microwave Source

---

To provide a tunable frequency of around 65 gigahertz an ultra-stable microwave-frequency generator is used to tune between the base frequency  $\nu_b$  of 16 to 16.5 gigahertz. Then a quadrupler (Sec. 4.4.7) will multiply this frequency by a factor of four resulting in a frequency  $\nu_L$  of 64 to 66 gigahertz.

---

<sup>13</sup> The SubMiniature version A (SMA) is a standard  $50\ \Omega$  connector developed in the 1960’s for high frequency purposes, usable from DC to around 20 GHz. High-frequency cables are coaxial cables that consist of additional shielding layers and are often silver-plated to reduce the losses due to the skin-effect.



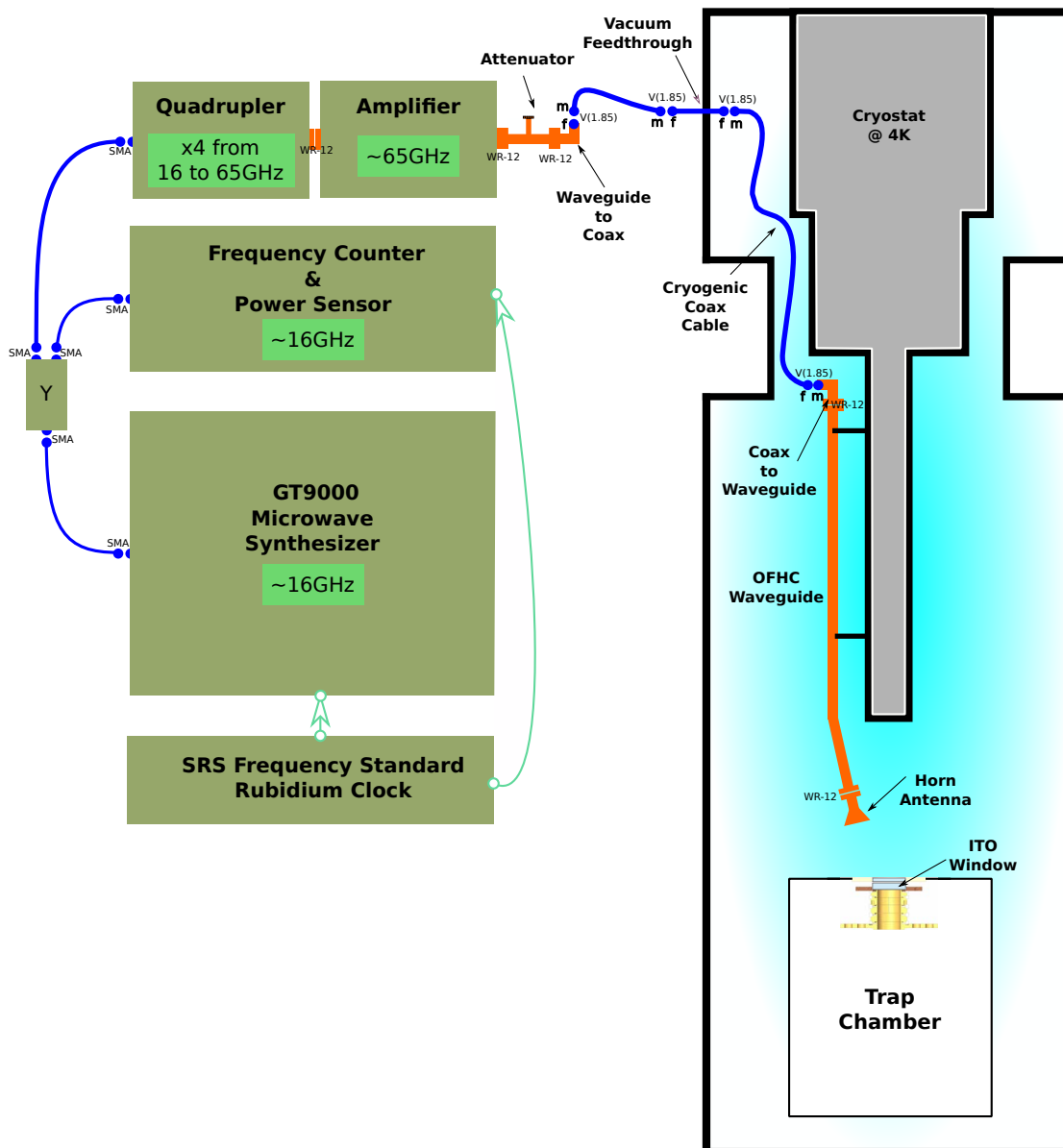


**Figure 4.17:** Overview of the hybrid design microwave system. The GIGATRONICS GT9000 microwave source produces a microwave with a frequency of around 16 gigahertz which is multiplied by the quadrupler to a frequency of around 65 gigahertz. This frequency is then transmitted, first through waveguides and then, after a waveguide-to-coax adapter, by a coaxial cable. Inside the vacuum, at cryogenic temperatures, a special non-magnetic cryogenic coaxial cable is used. After the difficult geometry at the top of the vacuum chamber, another coax-to-waveguide adapter is deployed and the microwaves are further transmitted by an about 1 meter long OFHC-copper waveguide, until a horn antenna irradiates them into the trap chamber. Waveguides are drawn in orange, coaxial cables in blue. For the high frequency coaxial cables, the gender of the plugs is indicated by ‘f’ for female and ‘m’ for male. The different types of transmission lines and the devices are explained in the next sections.



Therefore, a GT9000 microwave synthesizer from GIGATRONICS [68] is deployed which uses two different yttrium iron garnet (YIG) oscillators for generating the frequency: one oscillator to create a frequency from 2 to 8 gigahertz and the other for the frequency from 8 to 20 gigahertz. These YIG oscillators have a high quality-factor and therefore, are low-phase noise oscillators that are tunable by an adjustable magnetic field. They are tuned coarsely by a coil to 10 megahertz around the desired frequency and then fine tuned by a frequency modulation (FM) coil [68]. Via a phase lock loop the frequency is then compared with and locked to a 10 MHz frequency standard (either internal or external by the SRS FS725 Rubidium Frequency Standard).

Figure 4.18(a) shows a phase-noise diagram obtained with the KEYSIGHT N9000B-CXA spectrum analyzer at the base frequency of  $\nu_b = 16.255\,005\,076$  GHz, where the orange curve shows a snapshot of the phase noise and the blue curve the smoothed average given by the device. In the figure, four areas are shown that define the signal shape [69]: the red part is dominated by the noise from the 10 MHz frequency standard (the external rubidium standard); the plateau in the green area originates from the synthesizer (phase lock loop, phase detector, . . . ); the slope in the blue area stems from the YIG oscillator; finally, the overall thermal noise is detected in the gray area. Additionally, figure 4.18(b) shows the a frequency spectrum around the base frequency  $\nu_b$ .

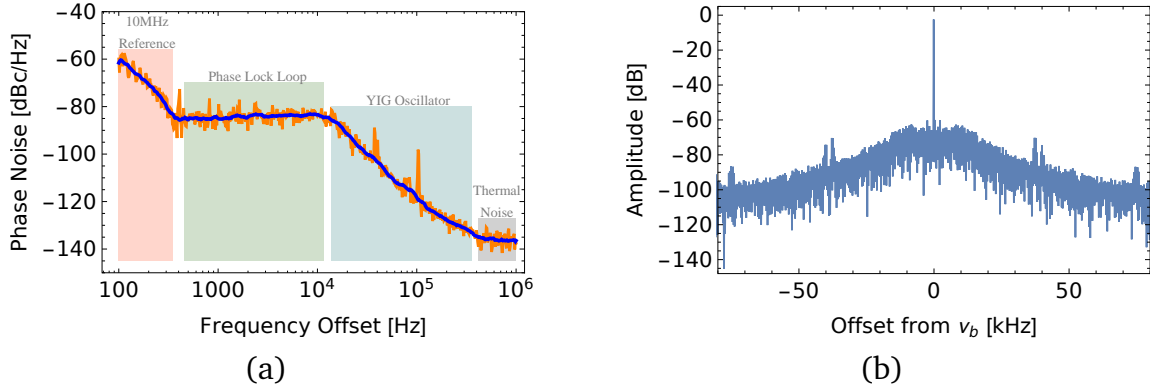


**Figure 4.18:** (a) Phase-noise measurement of the  $\nu_b = 16.255\,005\,076$  GHz base frequency of the GIGATRONICS GT9000 microwave source. The structure of the curve according to the different areas is found in the text. (b) Frequency spectrum around the base frequency  $\nu_b$  with the visible sidebands.

By using an EIP Microwave Model 578 Source Locking Microwave Counter the output frequency of the GT9000 was measured with an accuracy of 1 hertz, confirming the frequency measurement of the spectrum analyzer. Additionally, a long-term power measurement at the frequency  $\nu_b$  was conducted, yielding a stability of the output power of less than  $\pm 0.1$  dB over the time of 12 hours.

#### 4.4.4 Transmission Lines and Waveguide Flanges

The theory of propagating electromagnetic waves, waveguides and other transmission lines can be found in detail in [70, 71]. Due to the boundary conditions by the walls of a rectangular waveguide (where in  $x$ -direction is the width, in  $y$ -direction the height and in  $z$ -direction the direction of propagation), only certain waves can propagate. These waves are the  $TE_{nm}$  and the  $TM_{nm}$  waves, with  $n$  and  $m$  being the mode numbers and either the electrical field  $\vec{E}$  or the magnetic field  $\vec{B}$  being perpendicular to  $z$ . The typical wave for a standard rectangular waveguide is the  $TE_{10}$  mode.

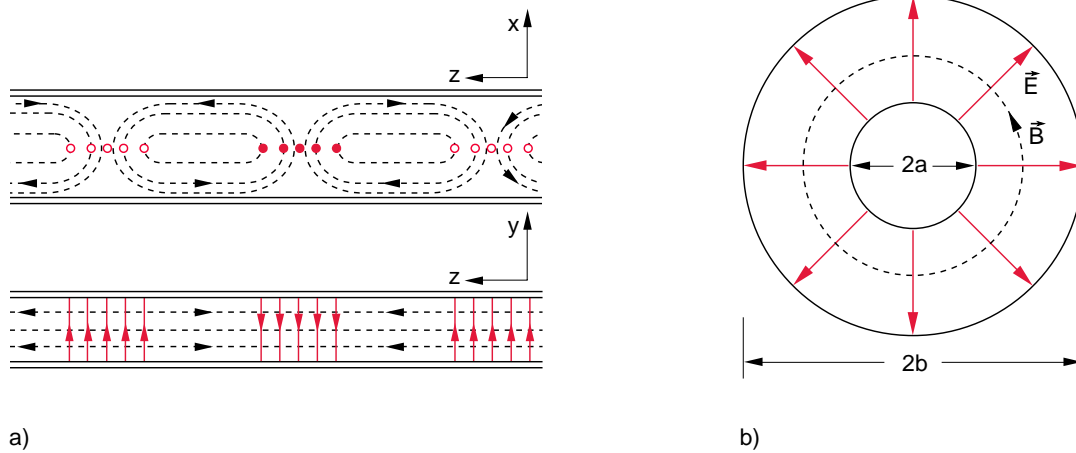


**Figure 4.19:** Figure taken from [70]: a) Propagation of a  $TE_{10}$  wave in a rectangular waveguide with the electric field lines in red and the magnetic field lines in black. The electric field is perpendicular to the  $z$ -direction. b) Propagation of a  $TE_{10}$  wave in a coaxial cable with the electric field in red between the inner and outer conductor and the magnetic field perpendicular to it, with  $a$  being the radius of the inner conductor and  $b$  the radius of the outer conductor.

A characteristic that is often used when working with microwaves is the VSWR, the voltage standing wave ratio. When two waveguides are not matched perfectly, there is always some power reflected on the mismatch, therefore, with the voltage reflection coefficient  $\Gamma = V_0^-/V_0^+$ , which is the ratio between the amplitude of the reflected wave and the amplitude of the transmitted wave, the VSWR can be written as:

$$\text{VSWR} = \frac{1 + \Gamma}{1 - \Gamma} = \frac{V_0^+ + V_0^-}{V_0^+ - V_0^-} \quad (4.5)$$

The VSWR therefore is a number between 1 (for a perfect match) and infinity. Table 4.2 gives some values for different VSWRs and their resulting power loss.

**Table 4.2:** VSWR values and their related transmission power losses. Data taken from [72]

VSWR	Power Loss [dB]
1	0
1.05	0.003
1.08	0.006
1.1	0.01
1.2	0.036
1.3	0.075
1.4	0.122
1.5	0.177

---

## Waveguides

---

Waveguides are classified according to their operating frequency band, other frequencies might also be transmitted, but with a strong attenuation, or, if these frequencies are lower than the mode dependent cut-off frequency  $\nu_c$ , not transmitted at all. There are standardized waveguide sizes for the various bands. For the frequency of 65 gigahertz the E-band (60-90 GHz) or the V-band (50-75 GHz) with the corresponding waveguide dimensions WR-12 and WR-15, respectively, can be used<sup>14</sup>. The bands also have different standard-flanges for connecting two waveguides, in the case of the two mentioned bands, the most commonly used flanges are the UG-387/U for the E-band (WR-12) and the UG-385/U for the V-band (WR-15). The current design only operates in the E-band, so all waveguides are WR-12 and the flanges use the UG-387/U standard. Figure 4.20 shows the dimensions of such a flange. They are contact precision flanges that are pressed together by four screws; two alignment pins and two holes on each side provide highest precision.

These waveguides are standard components, table 4.3 shows some properties according to their datasheet, and can be bought from various companies with different coatings for higher conductivity and therefore less transmission losses. For the design of ARTEMIS, a waveguide without the nickel diffusion barrier (which is necessary for gold plating) was needed, therefore, a 950 mm long waveguide from MI-WAVE made of bare OFHC copper is used.

---

<sup>14</sup> The numbering 12 and 15 links to the dimensions of the waveguide, as it gives the width of the rectangular cross-section in percentage of an inch. For example WR-12 has a width of 12% of 25.4 mm = 3.05 mm.

WR-12 Flange  
(UG-387/U)

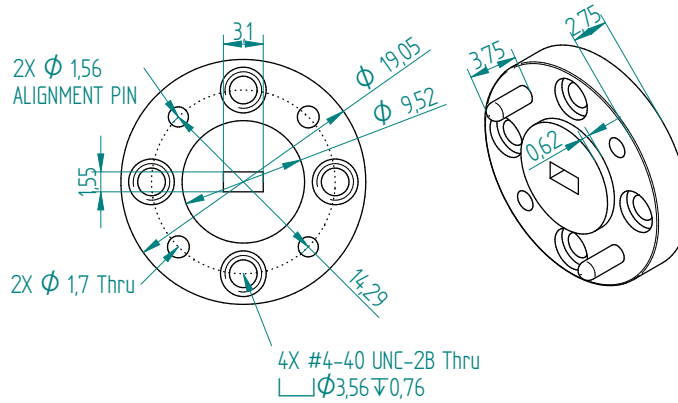


**Figure 4.20:** Technical drawing of a WR-12 flange for the E-band (60-90 GHz) with the UG-387/U standard. All dimensions are given in millimeter.

**Table 4.3:** Specifications of a standard WR-12 waveguide as presented in [72].

Frequency Range	60.5 - 92 GHz
TE <sub>10</sub> Cut-off Frequency	48.35 GHz
Dimensions ( $a \times b$ ) [inch]	0.122 $\times$ 0.061
Dimensions ( $a \times b$ ) [mm]	3.099 $\times$ 1.549
Theoretical Attenuation	3.11 - 1.74 dB/m
Connectors	UG-387/U

A major part of damping in waveguides is due to the finite surface conductivity, for a TE<sub>10</sub> wave with a frequency  $\nu$ , it can be estimated by [73]:

$$\alpha[\text{dB/m}] = \frac{0.0023 \cdot R_s}{b \sqrt{1 - (\nu_c/\nu)^2}} \left( 1 + 2 \frac{b}{a} \left( \frac{\nu_c}{\nu} \right)^2 \right), \quad (4.6)$$

with the waveguide typical cut-off frequency  $\nu_c$ , the longer width  $a$  and the shorter height  $b$  of the rectangular waveguide and the surface resistance

$$R_s = 0.00825 \sqrt{\frac{\sigma_{\text{Cu}}}{\sigma}} \sqrt{\nu[\text{GHz}]}, \quad (4.7)$$

with the ratio of conductivities  $\sigma_{\text{Cu}}/\sigma$  between copper and the waveguide material. With this formula an attenuation per meter of 2.3 dB/m for a copper waveguide at a frequency of 65 gigahertz is calculated. Note that the long waveguide will be at a temperature of 4 kelvin and therefore, the conductivity will rise, depending on the purity of the copper used, by two to three orders of magnitude, and therefore, resulting in a negligible loss.

---

## Coaxial Cables

---

Coaxial cables transmit TEM waves (Fig. 4.19) and are common for radio-frequency (RF) application, but for higher frequencies, due to the dielectric isolation, they suffer from higher losses than hollow waveguides – for applications above a frequency of around 20 gigahertz the common SMA connector is not suitable anymore. For higher frequencies different other types of connectors are available, although, assembling them is more difficult and needs special equipment and experience. For a frequency of 65 gigahertz the so-called 1.85 mm V-type is the standard connector.

The current hybrid design consists of two different types of high frequency coaxial cables, outside the vacuum chamber a commercial cable from ASTROLAB is used, whereas inside the vacuum a special low thermal conductivity cable from SHF is deployed, the SC-119/50-SB-B: it consists of a silver-plated copper beryllium inner conductor with a diameter of 0.29 mm, a 0.32 mm thick PTFE isolation and a 0.135 mm thick beryllium copper outer conductor. It has a minimal bending radius of 3.3 mm, is non-magnetic and is specified at room temperature to have a loss per meter of 14 dB/m at a frequency of 65 gigahertz. With an insertion loss of <0.7 dB and a length of 0.5 m this adds up to total loss of 7.7 dB.

Figure 4.21 shows the material compositions of the two cryocoax cables used. Please note that the measurement of table 4.12 was done with the TCR119CG/PB, with an attenuation of only 10 dB/m. Unfortunately, it broke and is not available anymore.

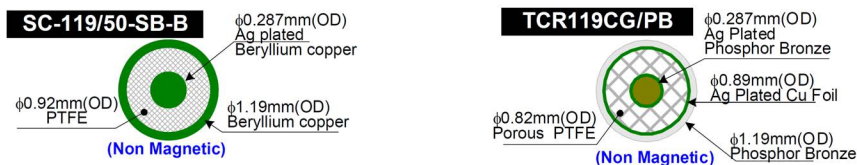


**Figure 4.21:** Material composition of the two different cryocoax cables from SHF. The coaxial cable with the cross-section shown on the left side, the SC-119/50-SB-B, is currently deployed in the apparatus. Pictures taken from [74].

---

### 4.4.5 Adapter: Waveguide-to-Coax

---

For conversion between  $TE_{10}$  mode waves and TEM modes, and therefore between transmitting the microwaves in waveguides or transmitting them in coaxial cables, an adapter is used (which can act either way, from waveguide to coaxial cable or vice versa). Figure 4.22 shows the principle of such an adapter: the inner conductor of the coaxial cable reaches into the waveguide, acting like an antenna. At a distance  $D$  the waveguide is closed and short-circuited, the waves are reflected and interfere in-phase with the waves from the antenna. This distance  $D$  is usually around one quarter of the wavelength of the microwave,  $\lambda/4$ . Additional tuning screws are used

to minimize losses due to high VSWR which is usually already performed by the manufacturer and locked before shipping. There are two different adapters from two different companies implemented in the current setup, the specifications can be found in table 4.4.

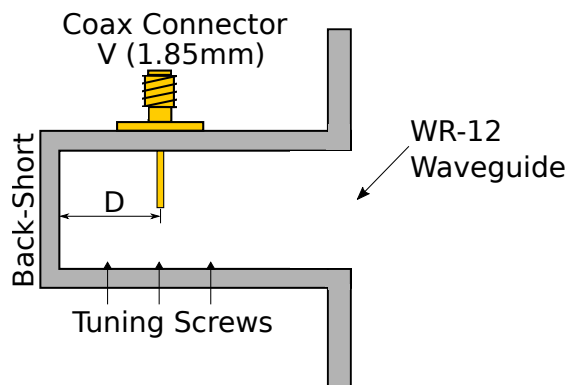


**Figure 4.22:** Schematic view of a coax-to-waveguide adapter as used in the experiment.

**Table 4.4:** Specifications of the waveguide-to-coax adapters 410E from MI-WAVE used inside the vacuum and the PTC-12VM-01 from DUCOMMUN used outside the trap chamber.

	410E	PTC-12VM-01
Company	MI-WAVE	DUCOMMUN
Frequency Range	60 - 90 GHz	60 - 90 GHz
VSWR	<2.0:1	1.8:1
Insertion Loss	1 dB	0.6 dB
Connectors	WR-12, 1.85 mm (male)	WR-12, 1.85 mm (female)

#### 4.4.6 The Vacuum Feedthrough

Vacuum feedthroughs with waveguide can be implemented for example by two antennas that are placed on opposite sides of a PTFE window, one transmitting the microwaves and the other receiving them after they passed through the PTFE vacuum seal [73]. Or by two thin epoxy-filled windows, sealing the vacuum, that are placed, at a distance of around a quarter wavelength of the microwaves  $\lambda/4$ , in-between the waveguide assembly [75]. In the case of ARTEMIS, since a coaxial cable was used anyways, a commercial vacuum feedthrough with 1.85 mm connectors from SHF was bought, which easily can be screwed into a hole in a commercial CF-flange<sup>15</sup>. The specifications of this vacuum feedthrough can be found in table 4.5.

<sup>15</sup> The CF vacuum flange, or ConFlat by VARIAN, ‘consists of two symmetrical flanges both having circularly-symmetric knife edges of a particular cross-section. A flat copper gasket is placed between the flanges and, when they are bolted together, the knife edges bite into the copper..’ [76].

**Table 4.5:** Specifications of the KPC185FFHA vacuum feedthrough from SHF.

Frequency Range	DC - 65 GHz
Insertion Loss	<0.7 dB
Temperature Range	−55 to 125 °C
He Leak Rate	10 <sup>−9</sup> mbar · l/s
Connectors	1.85 mm (female)

#### 4.4.7 Quadrupler

The underlying principle of most active frequency multiplications is the use of the non-linear voltage-to-current behavior in diodes. The current depending on the voltage can be expressed by

$$I(U) = I_s \left( e^{\frac{qU}{nk_B T}} - 1 \right), \quad (4.8)$$

where  $I_s$  is the diode-type dependent saturation current,  $q$  the electron's charge,  $k_B$  Boltzmann's constant,  $T$  the temperature and  $n$  the ideality factor that depends on the structure of the diode and varies typically between 1 and 2. This  $U$ - $I$  dependence can be expanded to higher orders. With low-pass filters these higher harmonics can be isolated and therefore, a multiplier by integer numbers can be built. However, not only the carrier is multiplied, noise levels are also increased: as a rule of thumb, the noise level is increased by  $20 \log m$  [dB] for a multiplication of  $m$ , therefore, in the case of the quadrupler, an amplification of the noise level of at least 12 dB takes place [71].

There exist various multiplier types, for example, reactive diode multipliers with varactor diodes or resistive diode multipliers that use Schottky diodes. Most of the multipliers, and also other active microwave parts, are built as monolithic microwave integrated circuits (MMIC) that combine different parts such as transmission lines, active devices, and other components on a semiconductor substrate.

In order to produce a frequency of around 65 gigahertz, an active quadrupler CFM1616X410-01 from CERNEX is used, with an output power of 10 dBm in a frequency range of 64 to 66 gigahertz. More specifications about this quadrupler are given in table 4.6.

The quadrupler is also equipped with an isolator on its outlet which prevents damaging the quadrupler by reflected waves. Many designs for isolators are known [77] and they have in common that the wave in the forward direction is almost not attenuated, whereas the returning wave is strongly attenuated. One example is the resonance isolator: a TE<sub>01</sub> wave traveling in a waveguide has a magnetic field traveling in the propagation direction as it is shown in figure 4.23(a). At one point of the waveguide, during wave propagation, the direction of the magnetic field vector will



change at every timestep – it rotates and circular polarization occurs. Additionally, at a certain distance from the wall, the amplitude will not change, therefore, at this position, a ferrite slab is introduced into the waveguide. This ferrite is biased by a permanent magnet mounted around the waveguide, making the electrons in the ferrite precess in a certain direction. If this direction coincides with the direction of the polarization, the energy of the wave is coupled into the system, attenuating the wave. This is called the resonance absorption and should be the case for the reverse wave. For the opposite, the forward wave, the two directions will not coincide, therefore leaving the wave unharmed. The exact calculation of this position can be found in [71].

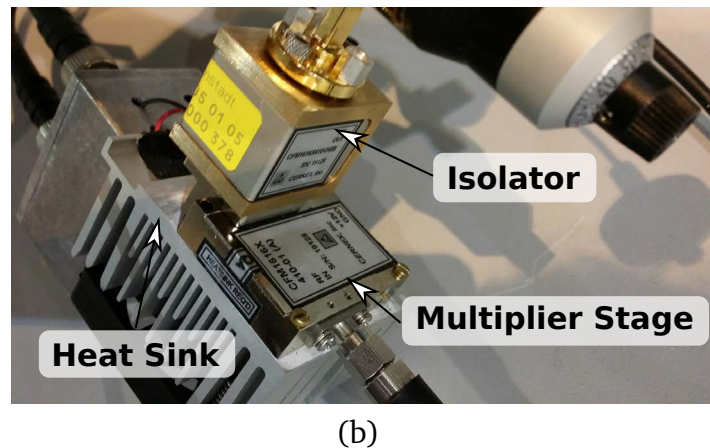
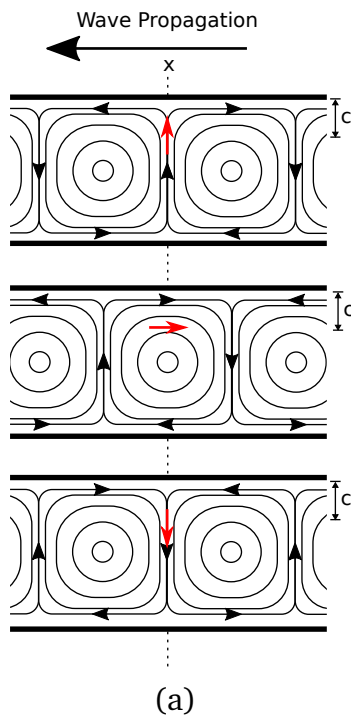


**Figure 4.23:** (a) Schematic showing the circular polarization of the magnetic field in a waveguide. The field lines propagate through the waveguide, therefore, at the point  $(x,c)$  the magnetic field vector is rotating. (b) Photograph of the quadrupler with isolator and heat sink attached.

Unfortunately, during the time when the tabletop test experiment was conducted, the quadrupler showed a strong power instability in irregular time intervals, one of the output stages was broken, so most measurements had to be performed carefully and constant surveillance of the output power was necessary. Also the desired output power of 10 dBm was never reached, most of the time the power only reached a value between 1 and 3 dBm.



**Table 4.6:** Specifications of the CFM1616X410-01 x4 multiplier from CERNEX.

Input Frequency	16 - 16.5 GHz
Input Power	10 dBm
Output Frequency	64 - 66 GHz
Output Power	10 dBm
Bias Voltage	12 V @ 400 mA
Connectors	SMA (f) (In), WR-12 (Out)
Size	MV4

#### 4.4.8 Amplifier

There are different kinds of amplifiers available which serve different needs. The two most prominent are the low-noise amplifier (LNA) and the power amplifier (PA). They are also built as monolithic microwave integrated circuits (MMIC) and therefore, their basic working principle is similar to a normal RF amplifiers which mostly consist of a transistor amplifier stage and impedance matching parts. LNAs are usually used, when there is only a small signal rising out of a noise floor since signal and noise figure then have the same gain and the output will still have a clear signal above the noise floor. This kind of amplifier is mostly used after a lossy line to refurbish the signal. A PA is used, when a strong signal before a lossy line is needed, as it is the case in ARTEMIS. Therefore, a SP654-15-24W power amplifier from SPACEK is deployed which has a gain of 19.8 dB with a corresponding maximum output power of 23.5 dBm at a frequency of 65 gigahertz. Due to complications with the VSWR at a frequency of 65 gigahertz the company could not deliver the exact specifications, so the current model has 1 dBm less output power. The updated, tested specifications can be found in table 4.7.

**Table 4.7:** Updated specifications of the SP654-15-24W power amplifier from SPACEK. The amplifier is equipped with a heatsink and fan assembly that uses 150 mA of the bias current.

Frequency Range	63 - 67 GHz
Gain	18.8 - 19.8 dB
$P_{\text{out @ 1dB gain}}$	21.5 - 23.9 dBm
$P_{\text{saturated}}$	22.5 - 24.9 dBm
VSWR	2:1
Bias Current	650mA @ +8 to +11 V
Connectors	WR-12

---

#### 4.4.9 Attenuator

---

Since tunable amplifiers are expensive, the amplitude of the signal can be tuned by an uncalibrated mechanically-tuned attenuator: by turning the dial it attenuates the microwaves by pushing a small slab into the waveguide. Table 4.8 shows the specifications of the 520E attenuator from MI-WAVE.

**Table 4.8:** Specifications of the 520E attenuator from MI-WAVE.

Frequency Range	60 - 90 GHz
Attenuation Range	0 - 25 dB
VSWR	1.15
Connectors	WR-12

---

#### 4.4.10 Horn Antenna

---

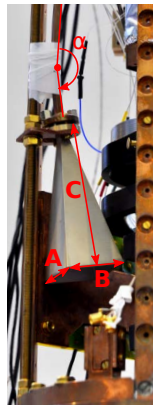
To irradiate the microwaves into the trap, a pyramidal horn antenna from MI-WAVE (Fig. 4.24(a)) is used which is designed to provide a high gain in the center forward direction. The gain  $G$  is defined according to

$$G = \frac{P_{\text{rad}}}{P_{\text{in}}} D, \quad (4.9)$$

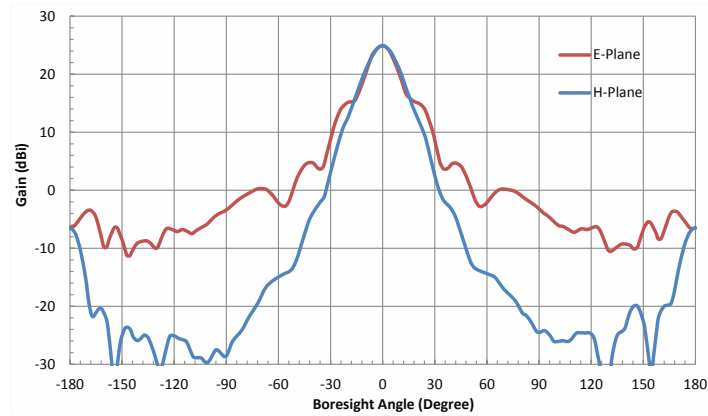
where  $P_{\text{rad}}/P_{\text{in}}$  is the ratio of the radiated power and the power supplied at the input of the antenna; and  $D$  is the directivity, a measure of how much power is emitted in the forward direction compared to the average radiation of an isotropic antenna [71]. A typical radiation pattern of a pyramidal horn antenna can be found in figure 4.24(b) and table 4.9 shows the specifications of the 261E horn antenna from MI-WAVE.

**Table 4.9:** Specifications of the 261E pyramidal horn antenna from MI-WAVE. BW stands in this case for beamwidth – the angle after which the gain drops by 3 dB.

Frequency Range	60 - 90 GHz
Gain	25 dB
3 dB BW E-plane	9°
3 dB BW H-plane	10°
Connectors	WR-12



(a)



(b)

**Figure 4.24:** (a) Geometries of the pyramidal horn antenna implemented in the experiment with the dimensions  $A= 37.1$  mm,  $B= 30.8$  mm,  $C= 81.3$  mm and the bending angle of the waveguide, so the center forward direction of the antenna points at the position of the ions of  $\alpha=11^\circ$ . (b) Typical pyramidal horn antenna gain for a 25 dB gain antenna at a frequency of 62.5 gigahertz. For a frequency of 65 gigahertz the radiation patten should be similar. Figure taken from [78].

After irradiation by the antenna, the microwaves are transmitted through the quartz window in the UMF and the borosilicate glass (N-BK-7) window with the ITO coating (Sec. 4.5.1). The propagation losses  $\alpha$  in the bulk materials of the windows can be estimated according to:

$$\alpha[\text{dB/m}] = 20 \log_{10} \left( e^{\frac{k \tan(\delta)}{2}} \right) \quad \text{with} \quad k = \frac{2\pi \nu \sqrt{\epsilon_r}}{c}, \quad (4.10)$$

where  $\nu$  is the frequency of the propagating microwave;  $c$  is the speed of light; and  $\epsilon_r$  and  $\tan(\delta)$  are the dielectric constant of the material and its loss tangent, a parametrization of the dielectric loss used in microwave engineering [71]. Table 4.10 gives some of the values taken from [71].

**Table 4.10:** Dielectric constants and loss tangents for different materials, with the corresponding calculated loss at a frequency of 65 gigahertz. Data taken from [71].

Material	$\epsilon_r$	$\tan(\delta)$	Loss [dB/m]
Fused Quartz	3.78	0.0001	1.1
Glass (Pyrex)	4.82	0.0054	70
Nylon	2.84	0.012	120
Plexiglass	2.60	0.0057	54
Polyethylene	2.25	0.0004	3.8
PTFE	2.08	0.0004	3.4

---

#### 4.4.11 Power Diode

---

The power diode uses the nonlinearity of a diode in order to convert a fraction of the power of the incoming microwave into a voltage that can be measured with a standard multimeter, where the video sensitivity (Tab. 4.11) gives the relation between the measured voltage and the incoming RF power. Although no power sensor is needed in the final hybrid design, a 950E power diode from MI-WAVE was used to conduct test measurements before the implementation into the ARTEMIS setup.

**Table 4.11:** Specifications of the 950E power diode from MI-WAVE.

Frequency Range	60 - 90 GHz
Video Sensitivity	500 mV/mW
Connectors	WR-12 (in), SMA (out)

---

#### 4.4.12 Tabletop Measurements

---

Before the microwave system was implemented in the ARTEMIS setup, a tabletop test experiment was conducted in order to characterize the system and test the complete assembly. In a first test experiment the losses in signal strength of most parts were measured with the 950E power diode from MI-WAVE (Sec. 4.4.11), the results are given in table 4.12 – the large errors result from the instability of the quadrupler (Sec. 4.4.7). All measurements were conducted with a source output power of 11.1 dBm, resulting in an input power of the quadrupler of 10 dBm, and a center frequency of  $\nu_b = 16.255005076$  GHz. Please note that these measurements were performed with the TCR119CG/PB cryogenic coax cable, not with the SC-119/50-SB-B that is currently installed (Sec. 4.4.4). Since most parts could not be measured individually, whenever it was possible, different combinations of parts were measured in order to extract the individual values for the power losses.

By having access to a spectrum analyzer with a larger frequency range, another measurement was performed: with the KEYSIGHT N9040B-UXA, capable of detecting frequencies of 65 gigahertz, the output power of the complete assembly was measured and compared to the output power measured directly after the quadrupler. Therefore, the signal-strength loss in the complete line (in this case with the SC-119/50-SB-B cryogenic coaxial cable) was measured to be 12.9 dB, with an output power of the quadrupler of 3.7 dBm. This is in accordance with the theoretical loss of 13.2 dB. Since the N9040B-UXA was only accessible for a short period of time,

only one measurement was conducted and therefore no value for the error due to the instability of the quadrupler can be given<sup>16</sup>.

**Table 4.12:** Theoretical and measured losses for the different parts of the hybrid design where  $l$  denotes the length of the transmission lines, the theoretical values are taken from the corresponding datasheets. Since most parts could not be measured individually, different combinations of parts were measured and the individual values extracted. The theoretical value for the complete assembly is the sum of all parts and the experimental value is from the measurement that was carried out with the KEYSIGHT N9040B-UXA. Please note that the measurement of the complete assembly was conducted with the SC-119/50-SB-B cryogenic coaxial cable.

	Theo. Loss [dB]	Meas. Loss [dB]
Waveguide-to-Coax Adapter	0.6	N/A
Short Coax Cable ( $l = 50$ mm) + Feedthrough	1+0.7	0.6±0.7
Cryo Coax TCR119CG/PB ( $l = 500$ mm)	5.7	3.9±1.1
Cryo Coax SC-119/50-SB-B ( $l = 500$ mm)	7.7	N/A
Coax-to-Waveguide Adapter	1	N/A
Waveguide OFHC copper ( $l = 950$ mm)	2.2	4.2±2.6
Complete Assembly (KEYSIGHT)	13.2	12.9

In another measurement with the KEYSIGHT N9040B-UXA spectrum analyzer and the complete setup assembled, the frequency of the GT9000 microwave source was swept from 16 to 16.5 gigahertz in 500 kilohertz steps and the output power was measured (Fig. 4.25(a)); afterwards this was repeated with a smaller frequency window from 16.25 to 16.26 gigahertz in 10 kilohertz steps (Fig. 4.25(b)).

Figure 4.26 shows a comparison between the phase-noise measurement of the source and the quadrupler combined and a phase-noise measurement of the whole hybrid design assembled, with a frequency set to  $\nu_b$ , resulting in a frequency of around 65.02 GHz after multiplying. The shape of the curve is similar to the curve for  $\nu_b$  which is explained in section 4.4.3.

After the microwaves are created, multiplied and transmitted, they are irradiated into the trap by the horn antenna. Here, additional losses have to be taken into account due to the UMF quartz window and the ITO coated N-BK-7 window (Sec. 4.5.1). As estimated in section 4.4.10, the losses for the bulk materials such as quartz and glass are small enough and can be neglected. The loss of the ITO coating was therefore measured with two opposing horn antennas where the UMF with the electrode holding the ITO-coated window was mounted in-between. After four measurements, over a timescale of several minutes to account for the instability of

<sup>16</sup> At the time when this measurement was performed, the unstable behavior of the output power was partially under control, detectable instabilities only occurred after some hours of operation. Therefore, the quadrupler was only switched on during the measurement, hence, for these few minutes no instabilities were detected.

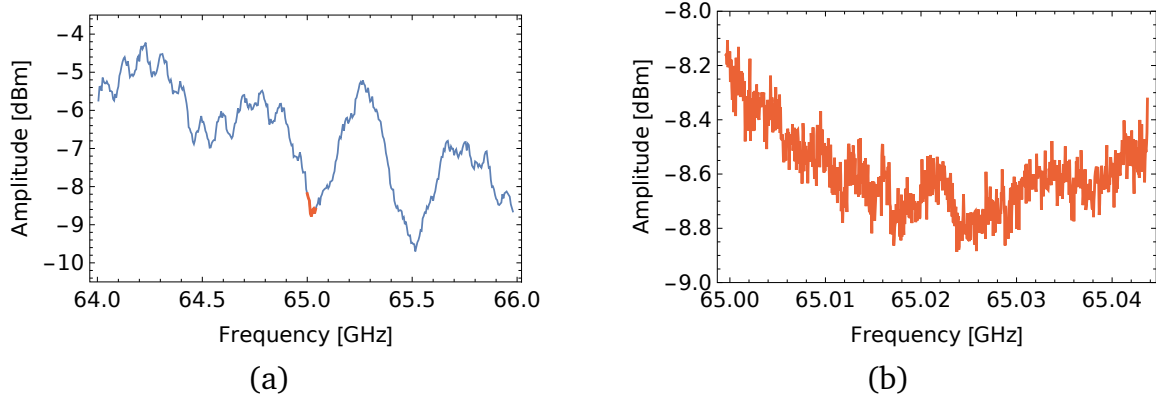


**Figure 4.25:** Frequency dependence of the transmitted power for the complete hybrid-design setup. (a) The frequency of the GT9000 microwave is swept from 16 to 16.5 GHz in 500 kHz steps. (b) The frequency is swept in a smaller frequency window from 16.25 to 16.26 GHz in 10 kHz steps. Please note that these measurements were performed at a later date and the output power of the quadrupler was not known precisely at that moment, hence, the measured amplitude is given.

the quadrupler, the total loss was measured to be  $23.4 \pm 4.2$  dB. This is a rather high value, but since the ITO coating is a conducting surface, it was not clear that there is a transmission at all. Although, the coating is only a few tens of nanometers thick and the skin depth is in the order of a few hundreds of nanometers.

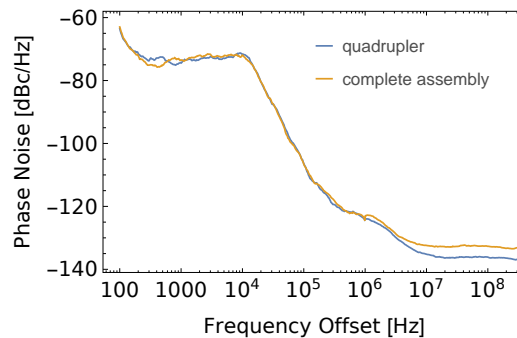


**Figure 4.26:** Phase noise at a frequency of 65.02 GHz, comparison between the phase noise of source and quadrupler combined and the phase noise of the complete assembly.

Altogether, the tabletop test experiment showed that with the hybrid design it is possible to transmit microwaves and irradiate the ions. With a conservative estimation (not taking into account the smaller losses at cryogenic temperatures) the total power is reduced by around 37 dB. With a maximum power after the amplifier of 24 dBm and a tunable attenuation range of 49 dB (by potentially excluding the amplifier), the power at the position of the ions can approximately be varied between  $-61$  and  $-12$  dBm or 0 to 50 microwatt correspondingly.

## 4.5 The Penning Trap

The heart of ARTEMIS is the Penning trap (Sec. 3.1), housed in the so-called ‘trap chamber’ which is hermetically sealed at cryogenic temperatures (Sec. 4.5.2) and therefore guarantees ultra-high vacuum conditions. It consists of a stack of hollow cylindrical electrodes with a inner diameter of  $17.513\ \mu\text{m}$  machined to micrometer precision out of OFHC copper. They are plated with a 20 micrometer thick silver diffusion barrier, with a less than one micrometer thick gold-plating on top. The Penning-trap stack can be divided into two parts, the spectroscopy trap (ST) and the creation trap (CT). A photograph of the trap can be seen in figure 4.27(a) with a labeled CAD drawing in figure 4.27(b). The creation trap (from electrodes H8 to H19) is designed for in-trap ion creation and later allows for in-flight capture of HCl from the HITRAP facility (Sec. 4.6). The spectroscopy trap (electrodes S1-S6) is for the final preparation of the ion cloud and conducting high precision spectroscopy. Both traps are connected by the transport electrode T7, so ions can be transported by slow-adiabatic passage between the traps. The electrodes are separated and electrically isolated with 3 millimeter thick macor rings in the CT and by 3 millimeter thick sapphire rings in the ST. Isolated copper rods, which are bolted to the UMF, attached to the top and bottom electrodes hold the stack together. Emphasis was put on keeping the electrodes as parallel to the UMF as possible and in a next stage the UMF was also aligned as parallel to the magnet flange as possible, resulting only in a very small tilt of the trap’s  $z$ -axis to the magnetic field axis. Although tilts modify the individual oscillation frequencies, the Brown-Gabrielse invariance theorem ensures the free cyclotron frequency to be unaffected by small tilts (Sec. 3.2). Table 4.13 gives the dimensions of the trap electrodes, on one hand the designed values and on the other hand the values taking the additional silver- and gold-plating and the thermal contraction into account.

**Table 4.13:** Trap geometries for the spectroscopy and the creation. The inner diameter ID and the inner height IH of the electrodes are given for the designed values from the CAD drawings, and taking silver- and gold-plating and the thermal contraction to temperatures of 4 K into account.

Electrode Number	ID <sub>CAD</sub> [mm]	IH <sub>CAD</sub> [mm]	ID <sub>4K</sub> [mm]	IH <sub>4K</sub> [mm]
S2	8.757	5.893	8.704	5.911
S3	8.757	5.380	8.704	5.4
S4	8.757	5.893	8.704	5.911
S5	8.757	6.220	8.704	6.237
S6	8.757	5.729	8.704	5.748
T7	8.757	8	8.704	8.010
H8, H9	10	6.5	4.961	6.516
C10 – C18	8.757	14.13	8.704	14.118



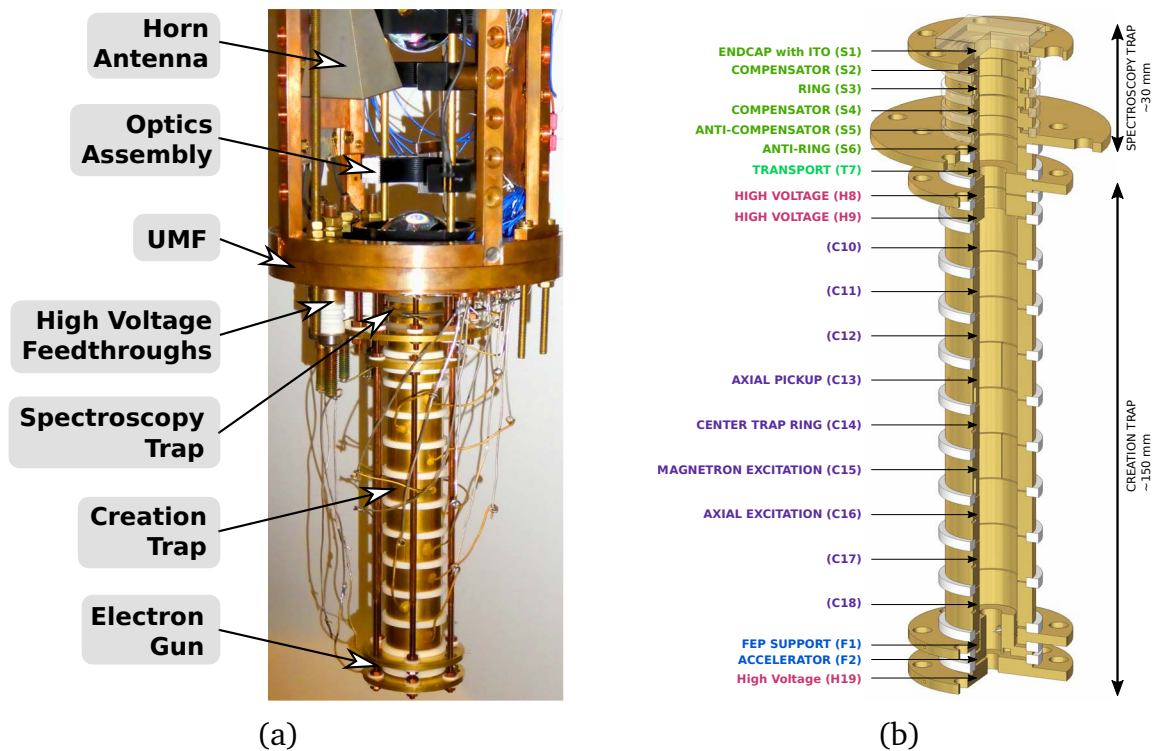


**Figure 4.27:** (a) Photograph of the double Penning trap with the trap chamber removed. On top of the trap the optics assembly together with the horn antenna for microwave irradiation is attached. (b) Rendered sectional view of the trap with the labels for the electrodes in brackets.

---

## Spectroscopy Trap

---

The spectroscopy trap (ST) is designed to satisfy the following needs:

- **Large Solid Angle**

To conduct spectroscopy, a large solid angle increases the overall light collection efficiency and therefore reduces the signal-to-noise ratio.

- **Trap Harmonicity**

For precise measurements of the cyclotron frequency the trap has to be as harmonic as possible.

- **Double-Trap Technique**

For creation or dynamic capture of ions the CT is necessary, transporting them into the ST is required.

- **Rotating Wall**

The ion density can be increased and hence, forcing more ions into the focus of the laser beam, increasing their excitation and therefore the spectroscopy light.



The best **trap harmonicity** for a cylindrical Penning trap is obtained by an electrically-compensated closed-endcap design as introduced in [34]. Since this would block the optical access, the open endcap design was proposed [33] – the potential of a long tube mimics a potential of a closed endcap. As pointed out in [79] the length of this long tube is typically in the order of four times  $z_0$  (for  $z_0 \approx \rho_0$ , Sec. 3.1). This leads to a solid angle of 0.2 steradian (sr). Therefore, for the upper electrode in the ST, the closed endcap design was modified by exchanging the optical closed copper electrode with an electrically conducting indium tin oxide coated glass window (Sec. 4.5.1) allowing optical access with a **large solid angle** of around 2 steradian.

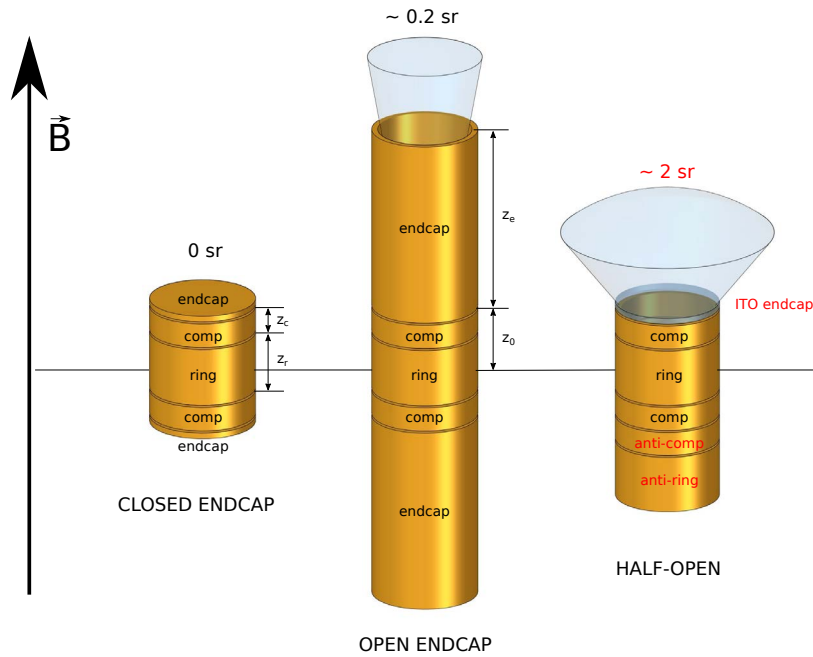


**Figure 4.28:** On the left: closed endcap electrically compensated Penning trap with  $z_r$  being the height of the ring electrode and  $z_c$  the height of the compensation electrode. In the middle: open endcap design with optical access on both sides and a rather small solid angle of 0.2 steradian. On the right: half-open design of ARTEMIS with a large solid angle of 2 steradian due to the light transmitting ITO coated endcap window and with a shorter length on the lower end due to the anti-trap design.

Since short consecutive traps are needed for a slow adiabatic transport, at the lower part of the trap a long tube cannot be used. Although other experimental setups couple many transport electrodes in order to simulate a long tube, in the case of ARTEMIS a shorter solution for the connection of the **two traps** was found, the so-called ‘anti-trap’. Figure 4.29(a) shows a schematic: after the compensation electrode a so-called ‘anti-compensator’ is added followed by an ‘anti-ring’; identical electrodes to the original ones but with exact opposite voltages applied to and therefore mimicking the potential of an open-endcap tube. Figure 4.29(b) shows a cross-section CAD drawing of the ST with some dimensions and the effective conical angle, also

showing the ITO-coated window. Since the dimensions of the anti-trap electrodes are symmetric to the dimensions of the ‘original’ trap electrodes, the gap between S4 and S5 has to be twice the length of the other gaps. The exact calculations and more details for this ‘half-open Penning trap’ can be found in [18].

Additionally, the spectroscopy trap comprises a four-fold segmented ring-electrode (S3) that can be used for the **rotating wall** technique [45]. The quarters are electrically isolated by sapphire spheres. The cyclotron resonator CRES (Sec. 4.3.2) is connected to the split S4 electrode and the axial resonator ARES ST (Sec. 4.3.1) is connected to S2. The ST is supplied by a HV200-8 from STAHL ELECTRONICS, nevertheless, the filter-board electronics should not exceed a voltage of  $\pm 30$  V. In a later stage, for more stability and accuracy the slower UM 1-14-28 can be introduced which has ten times more absolute accuracy (10 ppm) and 100 times less fluctuation (0.004 ppm per minute) [18].

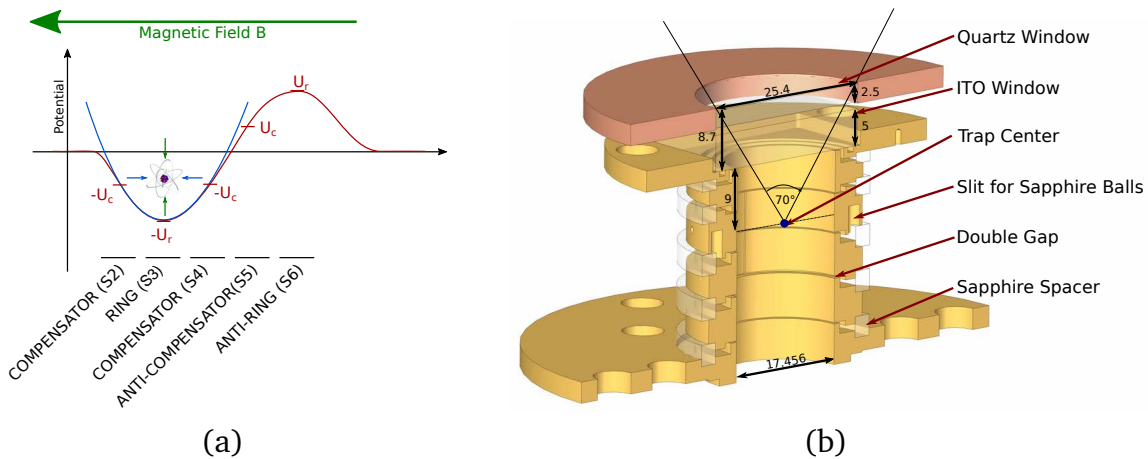


**Figure 4.29:** The half-open spectroscopy trap: (a) Shown in red is the potential of the spectroscopy trap. Since the anti-trap, consisting of anti-compensation electrode and anti-ring electrode are set to the exact opposite potential of their equivalent, this creates a harmonic potential shown in blue, where the ions are confined axially. Additionally, due to the magnetic field they are confined radially. (b) Cross-section drawing of the ST with the ITO coated endcap electrode and the quartz window, defining the conical angle for light emission. The dimensions are given in millimeter

---

## Creation Trap

---

The creation trap (CT) is designed to fulfill two main needs. At this stage in-trap ion creation is possible; at a later stage also in-flight ion capture from external sources is foreseen. Therefore, the creation trap consists of 12 electrodes and the electron gun (Sec. 4.5.2), with H8, H9 and H19 for the high-voltage confinement of the hot electron beam, and nine similar electrodes C10 to C18 which, when alternating voltages are applied, can form three consecutive mechanically compensated traps. Also here,

the principle of the anti-trap is used: when the second to next electrode has the opposite potential with respect to the next electrode harmonicity can be achieved despite the use of short endcap electrodes. All these electrodes are supplied by a HV 250-8 from STAHL ELECTRONICS capable of a voltage of  $\pm 250$  V and thus deep potential wells can be formed, designed to trap hot and big ion clouds.

After creation, the ion cloud is stored in C14, the central of the three ring electrodes. The axial resonator ARES CT (Sec. 4.3.1) is connected to C13; C15 is a split electrode for magnetron excitation, whereas axial excitation can be applied at C16. Due to the filterboards ‘CT/ST-Magn.-Exc’ should not exceed a voltage of 10 volts peak-to-peak and ‘CT-Exc.Ax-Dipole-Exc’ should not exceed a voltage of 15 volts peak-to-peak (Sec. A.2). The potential of C14 can also be fast switched to clean the trap with the SWIFT procedure which is demonstrated in section 5.8.

More details about the combined Penning traps, calculation and dimensions can be found in [79, 18]. Some relevant values taken from the latter reference are shown in table 4.14.

**Table 4.14:** Geometrical trap parameters for the spectroscopy and the creation trap with the additional 20 micrometer silver- and gold-plating and with the thermal contraction taken into account. Trap coefficients taken from [18]. The parameters are explained in section 3.1.

	$z_0$ [mm]	$\rho_0$ [mm]	$d$ [mm]	$C_2$	$C_4$
Spectroscopy Trap (S3)	9.008	8.704	7.714	0.5229	<0.001
Creation Trap (C14)	7.459	8.704	6.838	0.5631	0.001

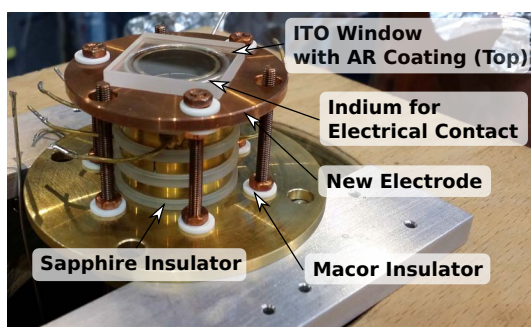
#### 4.5.1 Indium Tin Oxide-Coated Window

As mentioned above, the Penning trap comprises a large solid angle with the endcap electrode being as close as possible to the position of the ions. In the first design of ARTEMIS this was achieved by a thin fine gold-plated mesh that simulates a DC potential like a closed surface. Although the average transmission of light is rather good with a value of 60 %, due to unlucky circumstances it is possible that the peak of the laser beam can hit the strands and therefore, less than this average is transmitted. Additionally, since the mesh is visibly not planar, this can lead to unwanted anharmonicities of the trap.

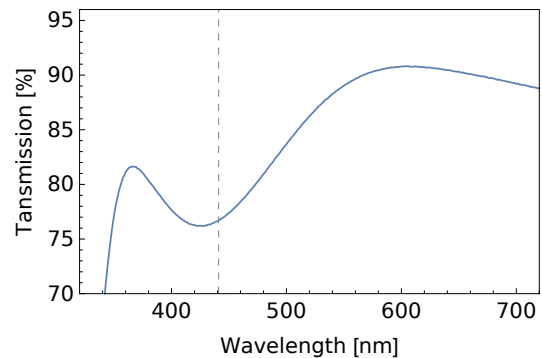
Therefore, the mesh was replaced by an indium tin oxide-coated (ITO-coated) window (Fig. 4.30(a)). ITO is tin-doped  $\text{In}_2\text{O}_3$  that, due to its big band gap of 3.75 eV [80], already in the middle of the last century was found to be transparent when applied in thin films on a substrate. Additionally, it was found, although it already has a quite low surface resistance, that by doping the electrical properties can be changed [81] and with different doping levels of tin an even lower resistivity can be achieved

[82]. Overall, the properties of an ITO film are very much dependent on how it is prepared and due to the interdependence of the mechanisms of electrical conduction and optical transmission ITO coatings can be manufactured to the requirements needed [83]. ITO has been used for example in microfabricated transparent surface traps [84].

The ITO-coated window used in ARTEMIS is the WTSQ11050-A from THORLABS [85]. It is a commercially available N-BK7 substrate with an anti-reflection (AR) coating for wavelengths of 350-500 nm on one side and with an ITO coating with a sheet resistance of 50-80  $\Omega$  /sq on the other side<sup>17</sup>. It has a transmission of 77 % for light with a wavelength of 441 nm.



(a)



(b)

**Figure 4.30:** (a) Photograph of the spectroscopy trap with the ITO-coated window built in. The indium wire can be seen which provides the electrical contact to the new S1 electrode. (b) Transmission of the THORLABS ITO coated WTSQ11050-A window. Data taken from [85]. The dashed line marks the 77 % transmission for light with a wavelength of 441 nm.

Since ITO is degenerate due to its high charge-carrier density, it shows a resistance behavior similar to metals and follows the Bloch-Grüneisen law. Nevertheless, at very low temperature, where the exact temperature of occurrence is depending on various parameters of the ITO coating, this law can not be applied anymore and a rise in resistance occurs [87]. This behavior was also found in a test experiment: the ITO-coated window was pressed, with its ITO-coated side facing down, on two pieces of indium foil for electrical contact and then clamped with a sapphire plate for thermal contact. The resistance between the two edges was measured during a cooldown phase and is shown in figure 4.31(a).

When ARTEMIS will be connected to the HITRAP beamline the endcap electrode might be used as an endstage Faraday cup charge detector indicating that ions were injected into the trap. To investigate if the typically few-hundred-nanometer-thick

<sup>17</sup> Definition from [86]: ‘The units for sheet resistance are  $\Omega$ , but people commonly use the units ‘ $\Omega$  per square’. The sheet resistance is numerically equal to the measured resistance of a square piece of the material. Note that sheet resistance is independent of the size of the square measured, and it is not necessary to know the film thickness to measure sheet resistance.’

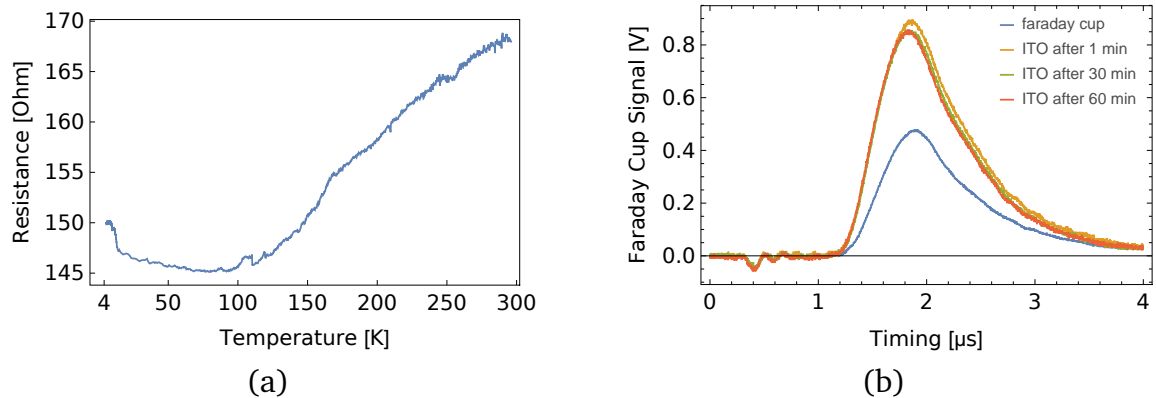


**Figure 4.31:** (a) Temperature dependence of the resistance of an indium tin oxide film. The THORLABS ITO-coated window was clamped and thermally anchored to a teststand cryocooler. The resistance was measured every 10 seconds during a cooldown to a temperature of 4 kelvin. Notice the rise in resistance after the temperature drops below a temperature of 75 kelvin and an even stronger increase after the temperature drops below 12 kelvin, since ITO is degenerate due to its high charge-carrier density. (b) Using the ITO as a Faraday cup in an EBIT: a commercial Faraday cup is compared to an ITO-coated window. Even after one hour with 8 ejections per minute of shooting highly charged ions on the ITO coating, no strong degradation of the signal can be seen.

ITO coating could be destroyed by HCI impact, an experiment was conducted in a DREEBIT Type-3 Electron Beam Ion Source located at HILITE. An electron beam ion trap (EBIT) uses an electron beam to ionize a target gas. The ions can then be trapped for further ionization or to conduct directly experiments in the EBIT or they can be extracted to other experiments. Every 8 seconds a beam of ionized residual gas atoms was extracted. These ions were first shot on a commercial Faraday cup, and then the anode was exchanged for a THORLABS ITO-coated window. The results can be seen in figure 4.31(b). It shows that the signal shape stays the same, it only changes in height due to the difference in resistances between the Faraday cup and the anode. Additionally, even after one hour with a total of around 450 ion impacts there is no visible degradation, so the ITO coated S1 electrode can be used as a detector on the endcap.

As far as the author knows, using an ITO-coated window as an electrode in a Penning trap was not yet implemented in other experiments, and in section 5.6 it is shown that the technique works as an endcap electrode forming a Penning trap, since it was possible to store ions in the spectroscopy trap. Closer investigations on how the ITO-coated window affects the harmonicity of the trap still need to be performed.

---

#### 4.5.2 Mini Electron Beam Ion Source (EBIS), Cryovalve and Gas Injection

---

In the future, ARTEMIS will obtain highly charged ions (HCI) either via the HITRAP decelerator or from external EBITs (Sec. 4.6). Nevertheless, since the beamline con-

---

necting HITRAP with ARTEMIS is still under construction, to this point, the ions are produced inside the trap with a home-made mini electron beam ion source that can ionize gases injected into the trap chamber by a cryogenic valve. Further information about this system can be found in [51].

---

### The Mini-EBIS

---

Typically, in EBITs, HCIs are produced by electron impact ionization, where the electron beam is usually created by thermionic emission of electrons. In the cryogenic environment of ARTEMIS this is not possible and therefore, electrons are produced in a so-called field-emission point (FEP), a sharp needle made of tungsten, where a highly negative potential is applied on a very small tip of several tens of nanometers. Therefore, the electric field line density in this tip is very high which leads to electrons tunneling through the potential barrier. With another electrode, the ‘accelerator’ electrode on a positive potential, these electrons are attracted and due to the high magnetic field trapped radially. The potential on the FEP defines approximately the kinetic energy of such produced electrons, whereas the accelerator’s potential, among others, determines the electron-current density. Similar to an EBIT, with reflection electrodes on both ends (in axial direction), the electron beam is also trapped axially and can be reused and therefore much higher charge densities can be achieved. Figure 4.32 shows a schematic of this principle as it is used in ARTEMIS. Neutral argon gas is let into the trap. The electron beam that was produced by the FEP is confined by the highly negative potential walls created between H8/H9 and H19. This electron beam then ionizes the argon gas, creating positive argon ions which are trapped in the three wells of the creation trap – C12, C14 and C16. Once lowly charged ions are trapped, they are constantly bombarded by the electron beam. This is called charge breeding and leads to much higher charge states. By controlling the electron-current density, the breeding time and the FEP voltage, different charge states can be produced effectively (Sec. 5.2). Note that the maximum charge state is always limited by the energy of the electron beam, thus by the voltage applied to the FEP. The FEP electron gun was built and tested by D. Lindenfels [51, 18].

The electron gun is supplied by a HV-FEP from STAHL ELECTRONICS, providing  $\pm 3$  kV. As mentioned above, the voltage applied to the FEP controls the energy of the electrons and the voltage applied to the accelerator determines coarsely the electron current (also called ‘FEP current’). However, the overall FEP current is determined by the FEP voltage, the accelerator voltage and the shape of the tip which can change over time, since it is not only one single tip, but rather a ‘dominant’ tip with several smaller tips on the side that can break or can be blocked by frozen residual gas. This leads to different FEP currents for the same voltages at different times. Although the display of the HV-FEP device shows this currents, it does not allow a PC-based readout; therefore, twice in 2016, a table was made. Figure 4.33 shows some of the values and it can be seen that there is a significant change.

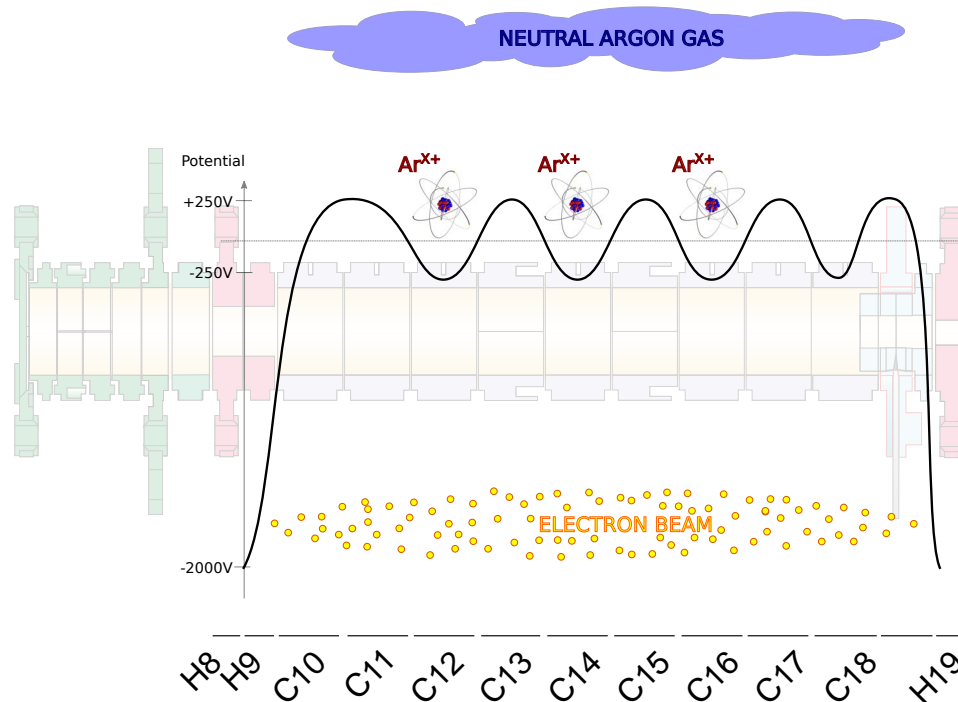


**Figure 4.32:** Scheme of the in-trap ion creation: the potentials of the ion trap are set such that they form three potential wells. Additionally, the high voltage electrodes H8/H9 and H19 are set to highly negative potentials and therefore, the electron beam from the FEP is reflected between those electrodes. Argon gas is inserted which is ionized by electron impact and the so produced ions are trapped in the three potential wells, where their charge state will be further increased by charge breeding.

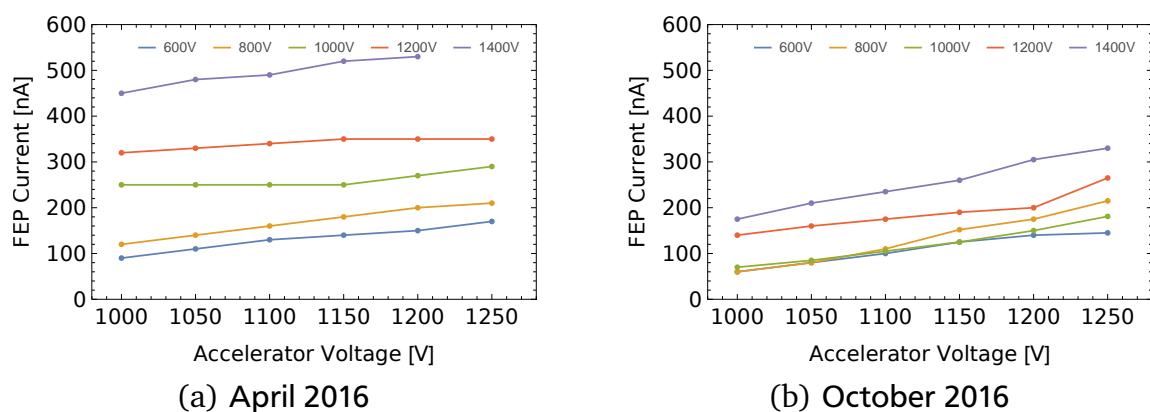


**Figure 4.33:** FEP currents for different combinations of accelerator voltages and FEP voltages, shown in different colors (legend). The left figure was measured in April 2016, the right figure in October 2016.



---

## The Cryo Valve and Gas Injection

---

To inject gas, a two-stage valve system is used which is explained in detail in [18]. In a first stage, the so-called ‘cross’ is flooded with argon gas. By using a dosimeter valve, only a small flow of gas is led into a defined volume, whereas this flow is maintained by constant pumping by a vacuum pump. Once this flow is stable, a pressurized air controlled valve can be opened for a defined period of time. This valve is preferred over an electrically-controlled valve since its relay can be placed outside the strong magnetic field and therefore does not distract the field when being switched.

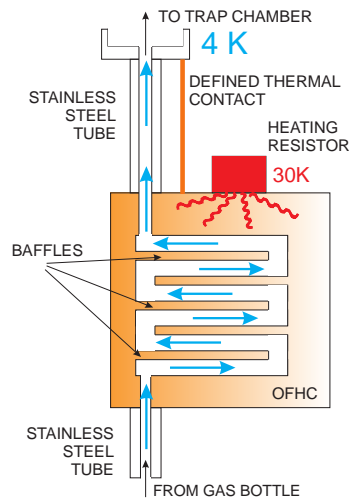


**Figure 4.34:** Schematic of the cryo valve: baffles inside a copper cylinder block a direct path between the lower and the upper stainless-steel tube. This cylinder is cooled to cryogenic temperatures and therefore, all gas atoms will freeze on the surface since they touch the surfaces various times due to the chicane-like structure. Therefore, the valve is closed. By heating the copper cylinder above a specific temperature, the gas atoms are not frozen anymore on the surface and therefore, the valve is opened. Figure taken from [51].

Between the pressurized air controlled valve and the trap chamber there is a second valve: in order to reach a ultra-high vacuum, the complete trap chamber has to be at temperatures of 4 kelvin to enable cryopumping. Since moving parts are difficult to implement at cryogenic temperatures, a special valve was designed which consists of a baffle structure that forms a chicane as it is shown in figure 4.34. This chicane, when kept at very low temperatures, has a non-zero sticking coefficient for all gases except helium. Due to its structure, all atoms will touch the surface of the walls several times and as a result will stick at some point. This blocks all residual gas atoms from the outside, enabling a vacuum in the trap chamber smaller than  $10^{-15}$  mbar. By heating this chicane structure, the sticking coefficient can be modified, thus ‘opening’ it for argon gas. Hence, to inject gas, the cryo valve is heated for a short period of time, increasing its temperature to approximately 30 kelvin, then the



---

pressurized air controlled valve opens for a few milliseconds and an argon gas pulse is let into the trap chamber. After a few seconds the cryovalve is again cooled down to a temperature of 15 kelvin and ‘closed’ again.

---

## 4.6 Fast Opening Valve

---

The previous section described the in-trap ion production of medium-charged heavy ions. In the future, ARTEMIS will be connected to the HITRAP facility which enables access to heavy highly charged ions such as hydrogen-like uranium [88]. Additionally, an external EBIT will be accessible for testing purposes and independence of beam-time. Most of the beamline already exists and is described in [89, 90]. Nevertheless, the beamline of this connection, the so-called ‘last meter’ to ARTEMIS, is still under construction.

Although the beamline vacuum is already a high vacuum with around  $10^{-10}$  mbar, to achieve storage times for highly charged ions in the order of hours or even days, the vacuum has to be at least  $10^{-13}$  mbar or better, which can only be achieved by a quasi closed trap chamber and cryopumping. Therefore, one attempt is the so-called fast-opening valve (FOV) which operates at cryogenic temperatures and separates the two vacua, namely the beamline vacuum and the trap vacuum, by being opened only for some tens of milliseconds. Hence, not to disturb the magnetic field, its electrical motor has to have a certain distance to the magnetic field center. Since a valve meeting these requirements was not commercially available, this FOV was designed together with W. Schott from TU Munich and built by the company PINK.

Figure 4.35(a) shows a CAD drawing of the ‘last meter’ with the FOV being installed below the magnet and figure 4.35(b) shows a cross-section of the fast-opening valve: two electromagnets (ITS-LS 4035 D-12 from CONRAD ELECTRONICS) with a pulling force of up to 36 newton sit on opposite sides and take turns in pulling via a long rod on the outer rim of the actuation tube. By turning this tube the shutter placed on top of it will be opened and shut. Shutting, in this case, means that a titanium bolt, which is slightly pressed against the bottom of the trap chamber, is pushed in front of the entrance and therefore blocks it. For a room-temperature valve this would not be sufficient to separate two vacua, since there is no sealing material between them. For the FOV this is different, since all parts are at cryogenic temperatures of 4 kelvin and the vacuum conditions provide molecular flow. By blocking a direct path all residual gas atoms will hit the cryogenic surface several times and due to the non-zero sticking coefficient, they will be adsorbed after some contacts with the surface.

The complexity of this device, in a mechanical sense, is rather high, since three vacua (including the magnet bore vacuum) have to be separated and the temperature of 4 kelvin has to be maintained which requires additional heat radiation shielding (Sec. 4.2) and therefore several tube-in-tube structures are necessary. A detailed explanation of the exact setup, a description how to assemble the FOV, and first tests and their results can be found in [54]. In atmospheric conditions functionality was

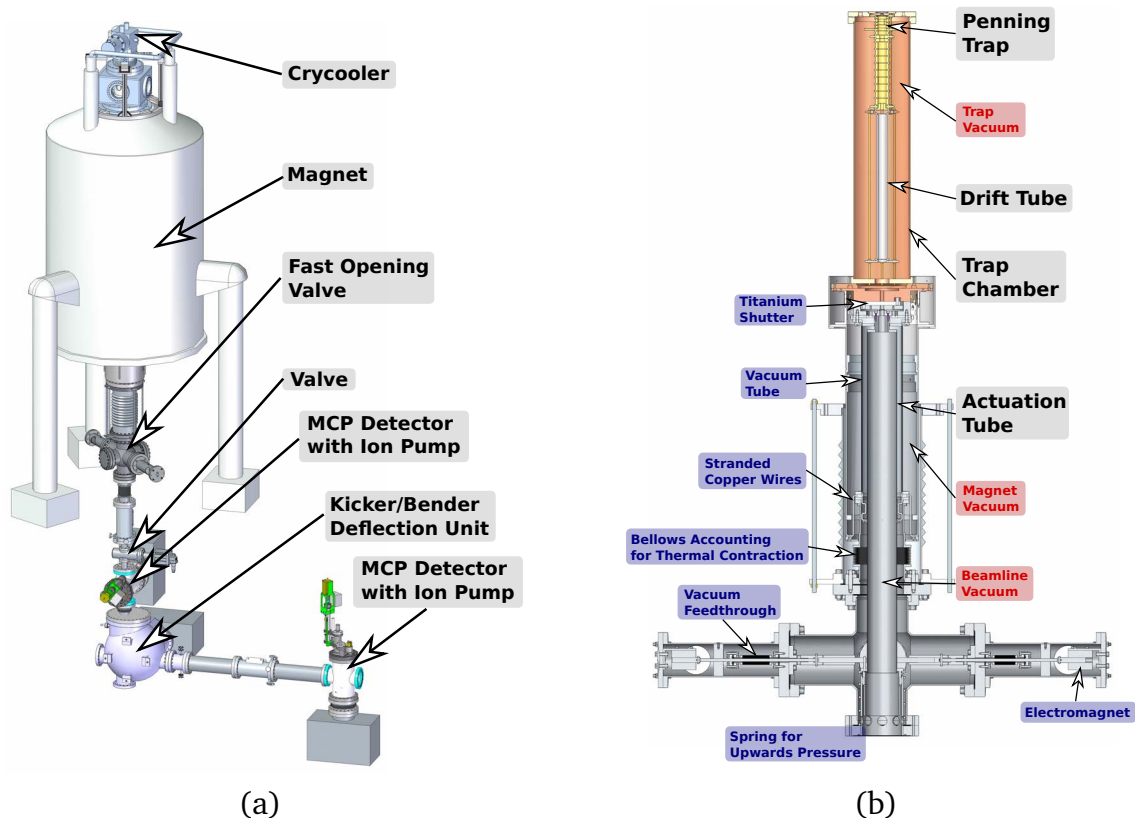


**Figure 4.35:** (a) CAD drawing of the ARTEMIS magnet, showing the fast-opening valve and the ‘last meter’ of the beamline. (b) Cross-section of the fast-opening valve with the drift tube and the trap chamber on top.

proven and opening times of several tens of milliseconds were achieved. Nevertheless, at cryogenic temperatures it could not yet be tested sufficiently.

On the other hand, simulations with the gasflow program Molflow+<sup>18</sup> showed that even with an opened FOV, due to the geometry of a thin tube and the cryogenic temperatures, already a suppression in the transmission of residual gas atoms of  $10^{-5}$  can be achieved [54]. Additionally, SimIon<sup>19</sup> simulations showed that it is still feasible to place the shutter of the valve below the bottom magnet flange [91] and therefore simplify the complicated inversed ‘T’ structure of the valve in a one-dimensional apparatus. Both ways, the original idea of the FOV as well as a more simplified structure, are currently under investigation.

<sup>18</sup> Molflow+, ‘A Monte-Carlo Simulator package developed at CERN’ that allows ‘to calculate the pressure in an arbitrarily complex geometry when ultra-high vacuum condition is met.’, <http://molflow.web.cern.ch/>

<sup>19</sup> SimIon ‘is a software package primarily used to calculate electric fields and the trajectories of charged particles in those fields when given a configuration of electrodes with voltages and particle initial conditions, including optional RF (quasistatic), magnetic field, and collisional effects.’, <http://simion.com/>

---

## 5 Preparation of an Ion Cloud and Measurements

For  $g$ -factor measurements in boron-like argon via double-resonance spectroscopy (Sec. 2.3), a sufficiently cooled cloud of  $\text{Ar}^{13+}$  ions has to be stored in the spectroscopy trap (ST, Sec. 4.5). Experimental studies to find the right parameters for important intermediate steps, such as creation of highly charged ions, cooling an existing ion cloud, and removing all unwanted charge states, are presented in this chapter. A detailed analysis of the creation trap (CT, Sec. 4.5) was carried out and is reported. Transporting ions from the creation into the spectroscopy trap has been successfully performed and further investigation of the transport between different traps is outlined.

This chapter reports the measurements done with the setup assembled in the beginning of 2016 whereas in [18] the results of the measurement time in 2015 can be found. There, the fundamentals in ion creation and ion cooling were laid, however, at that time, the setup suffered from limitations preventing further advance, *e.g.* the short-circuit between electrodes C11 and C13<sup>1</sup>, the false fluorescence of the optical parts and the malfunction of the resonator in the spectroscopy trap. These problems were solved and together with some minor changes, several major improvements were carried out between the 2015 and 2016 measurement time, as reported here:

- The microwave system capable of 65 gigahertz for irradiation of the ion cloud was tested in a tabletop experiment and installed in the experiment (Sec. 4.4).
- The optical detection system was revised and improved, providing additional modularity and adjustability (Sec. 4.3.3).
- A new axial resonator was built and connected to the spectroscopy trap whereas the old axial resonator, which was previously connected to the ST, was repaired and attached to the creation trap (Sec. 4.3.1).
- The argon gas injection system was improved which results in less leakage and therefore in a better vacuum in the trap chamber and a longer usable period of the argon gas bottle.
- A varactor diode was introduced to shift the resonance frequency of the cyclotron resonator (Sec. 4.3.2).
- The mesh on the endcap electrode S1 was replaced by an ITO-coated window (Sec. 4.5.1).

---

<sup>1</sup> Figure 4.27(b) in section 4.5 shows the labeling of the different trap electrodes.

- 
- During the 2016 measurement time a new spectrum analyzer (KEYSIGHT N9000B-CXA) was introduced, with which the thermal noise of the ARES CT could be detected (Fig. 4.10(a)), replacing the RIGOL DSA-815TG.

A detailed historic overview of the measurement phases can be found in section A.3.

In the first part, this chapter gives an overview of the data acquisition, the LABVIEW control system, and introduces the most frequently encountered depiction of measurement data, the charge-to-mass ( $Q/M$ ) spectrum. Then a closer look into the creation of ions with the current setup is given (Sec. 5.2), where investigations were pursued in order to optimize the production of  $\text{Ar}^{13+}$ . Section 5.3 focuses on ion cooling, namely the resistive cooling of the axial motions and afterwards, a more detailed view on specific features in the creation trap is given, for example the creation of highly charged tungsten  $\text{W}^{27+}$  or non-linear effects of the detection system. Based on a measurement of the reduced cyclotron frequency the magnetic field in the creation trap is estimated in section 5.7. Afterwards, investigations on the ion transport into the creation trap and from there to the spectroscopy trap are reported and the measured ion signal in the ST is then shown and discussed. Finally, it is reported how the ion cloud, a mixture of many different argon charge states, is purified via the SWIFT method (Sec. 5.8), such that only  $\text{Ar}^{13+}$  is left.

---

## 5.1 Data Acquisition

---

If not noted otherwise, the data in this chapter was recorded by the KEYSIGHT N9000B-CXA spectrum analyzer (SA) which can be controlled by the LABVIEW experimental system that is briefly explained in the following section, whereas afterwards, the different methods of taking data with the spectrum analyzer are explained.

---

### 5.1.1 Introduction to the Measurement Labview System

---

The LABVIEW<sup>2</sup> measurement system was introduced by D. Lindenfels [18] and further extended during the time of this thesis. It is a work in constant progress and therefore only a short introduction is given.

Most experimental processes and ideas, especially in the set-up phase of the experiment, require flexible programming of the control system. For example, when investigating a new technique, different ways of implementation have to be studied

---

<sup>2</sup> LABVIEW is a graphical programming environment from NATIONAL INSTRUMENTS which is used in many experimental physics groups since it provides a fast and pictorial way of programming experiment-control systems. Program-subroutines are called virtual instruments (VIs) and consist of a block diagram, where the graphical programming language is used and a front end, where buttons, input and output panels and other graphical representations mimic the front end of a physical measurement device. Different sub-VIs can be combined in order to build a comprehensive measurement system.

and huge sets of parameters are run through in night or weekend measurements to find the best working point.

These requirements were satisfied best by exclusively using the block diagram structure of LABVIEW. A so-called VI-tree was created, consisting of sub-VIs that each represent an experimental procedure and therefore, by combining lists of parameters with loop and flat sequence structures, more complex consecutive tasks can be built and executed. Every measurement scheme is saved in a new file and thus, all parameters are saved with it. This is an improvement over the ‘front end’ system for the master VI in which every new input needed to be attached with an additional saving function. An example of such a measurement scheme is given in figure 5.1: first, an ion creation is performed, then the trap is cleaned of unwanted ions and afterwards the ions are magnetron centered and finally further cooled. The different techniques are explained in the following sections.

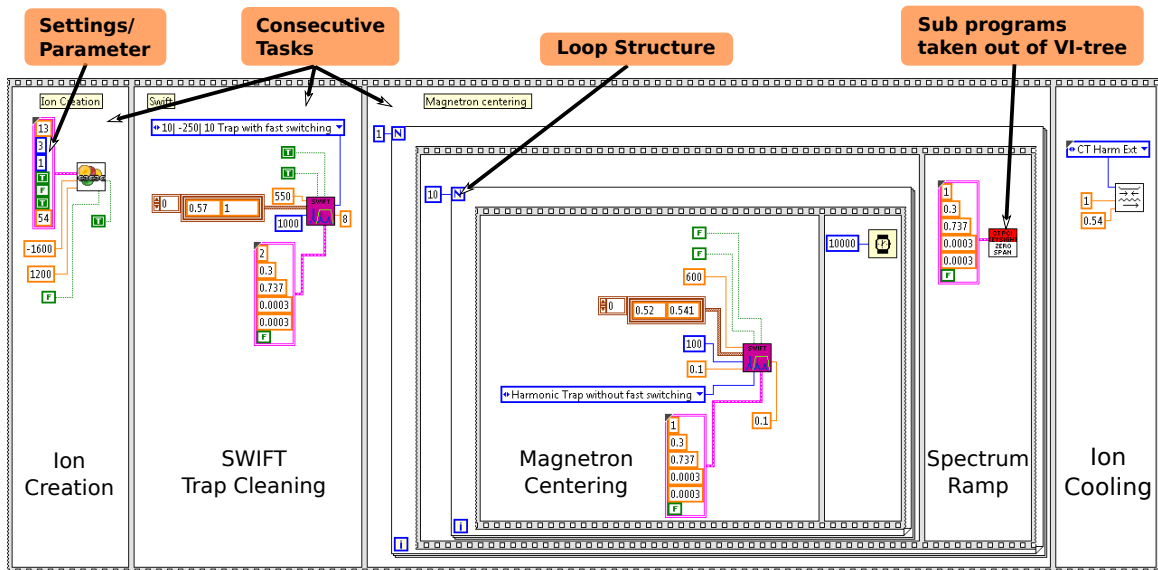


**Figure 5.1:** Example of a block diagram LABVIEW routine. By using the block diagram function, modularity is obtained by combining sub programs (sub-VIs) from the VI-tree. A flat structure (‘film reel’) separates the consecutive tasks that are performed: first, ions are created with a given set of parameters; then a cleaning task is applied; afterwards a loop structure is executed, in which the ions are magnetron centered and then a spectrum is taken; finally, the trap is set for ion cooling. The different techniques in this diagram are explained in the following sections.

## 5.1.2 Spectrum Read Out

The most important measuring technique in ARTEMIS is the so-called spectrum ramp or charge-to-mass ramp which is used for resolving the different ions in the trap according to their charge-to-mass ratio. Three different methods, distinguishing mostly in how the data is processed, can be utilized. Figure 5.2 gives a schematic illustrating

these methods which are explained in the next three subsections. Nevertheless, they have in common that they exploit the relation for the axial frequency (Sec. 3.2):

$$\omega_z = \sqrt{\frac{Q C_2 U_T}{M d^2}}, \quad (5.1)$$

to link the axial frequency directly to the charge-to-mass ratio  $Q/M$ ; where  $C_2 \approx 0.56$  is a trap coefficient,  $d$  is the characteristic trap dimension (Eqn. 3.2) and  $U_T$  is the applied electric potential to the trap. The resonator is fix in frequency, for example the ARES CT has a resonance frequency of  $2\pi \times 737.5$  kHz, so by tuning the trap potential  $U_T$ , ions with different charge-to-mass ratios come into resonance with the resonator, thus, creating a resolved spectrum of the charge-to-mass ratios of the ions. This procedure is performed stepwise where in each step, the trap voltage is decreased<sup>3</sup> and the strength of the resonator signal is measured. Additionally, in order to account for the fact that the charge-to-mass ratio depends quadratically on the frequency, the voltage step size is adjusted correspondingly when applying lower trap voltages and therefore, the value for the step size is given in units of frequency rather than in volts. Figure 5.2 shows the three different schemes that can be applied in order to record a spectrum ramp.

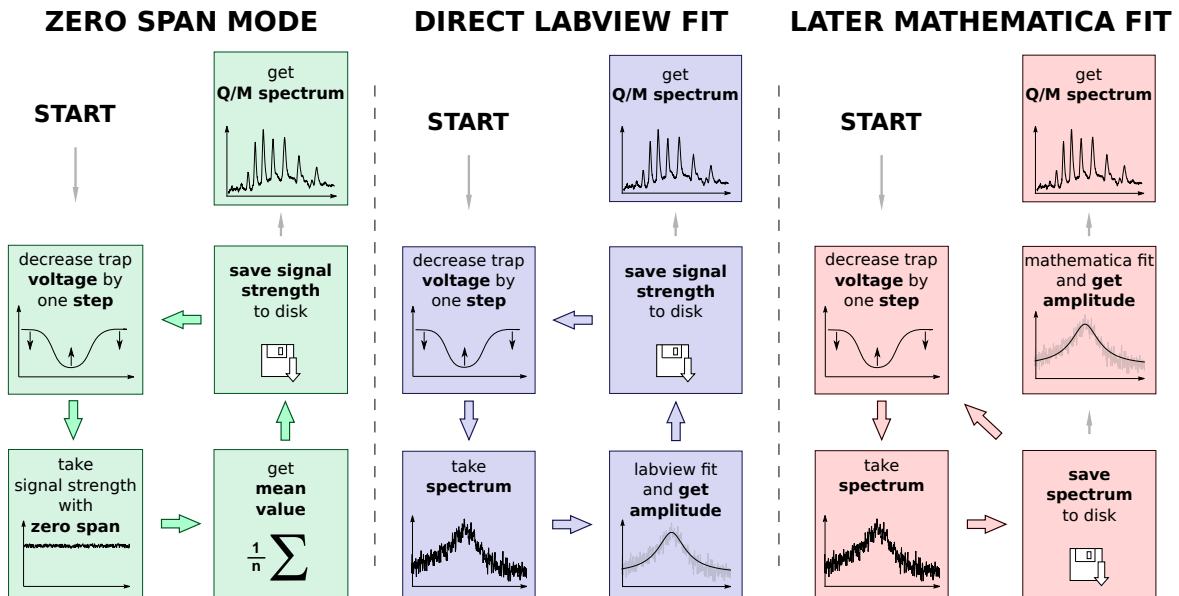


**Figure 5.2:** Scheme of the three different methods for data taking: after each voltage step a data set is taken and either directly evaluated or saved for later evaluation and with the so achieved data, for example, spectra resolved by the charge-to-mass ratio of the ions can be created. More information is given in the text.

<sup>3</sup> Since it does not matter for the signal shape, if the ramp goes from lower to higher voltages or vice versa, the latter is taken, to minimize the ion loss by cooling them first before the potential decreases.

---

---

## Zero-Span Mode

---

In the ‘zero-span mode’ the local oscillator of the spectrum analyzer is set to a specific frequency, namely the center frequency of the resonator and the signal amplitude is integrated in the bandwidth window around this frequency. Thus, the signal strength is presented as a function of time. The advantage of this method resides in its rapidity and its sensitivity since with this measurement method a spectrum can be created, even when the thermal-noise resonance of the resonator cannot be detected due to the high internal background noise (as it is the case with the RIGOL SA). For the ‘zero-span mode’ the usual setting is a recording time of 100 milliseconds per voltage step, with a bandwidth of 100 or 300 hertz. After each step, the mean value of the signal strength in the recorded time window is calculated and saved.

---

## Direct LABVIEW Fit

---

The ‘direct LABVIEW fit’ method takes advantage of the fact that with the KEYSIGHT SA the thermal noise of the ARES CT is visible. After each voltage step a complete resonance spectrum is recorded and then, with a in LABVIEW implemented routine, a Lorentzian is fit to it; the peak value is saved and the next voltage step is applied. Afterwards, every peak value is plotted versus the voltage in order to receive the spectrum. Although in principle the spectrum analyzer can record one of these spectra in only a few milliseconds, when the fast Fourier transform (FFT) mode is active, the rather long fitting time of the LABVIEW program increases the overall time that is needed to record one spectrum.

---

## Later MATHEMATICA Fit

---

In the ‘later MATHEMATICA fit’ method, the spectrum is recorded similar to the previous method, but the complete data of the spectrum is saved on the disk and, after the complete measurement, a MATHEMATICA notebook needs to be loaded to fit the data. Since it can use the advantage of the FFT mode of the SA, the method is also fast in recording the overall data and additionally, all informations are saved and can be used for later evaluation. Nevertheless, the disadvantage of that method is the amount of data – one single ramp needs approximately 100 MB of disk space – and also it is quite unhandy, since it is always necessary to run the MATHEMATICA notebook afterwards. Figure 5.3(a) shows a 3D plot of an unevaluated data set taken with the ‘later MATHEMATICA fit’ method. In every step a complete spectrum of the thermal noise of the resonator is taken and once the ions start to get into resonance with the resonator, the overall curve gets wider and broader. This happens because the ions axial motion bandwidth is much broader than the ARES CT bandwidth – if the motional bandwidth was smaller, a peak would rise on the thermal noise resonance curve and in the case of only a few cold ions, this could even result in a dip [49].



Figure 5.3(b) displays that all three methods yield similar results. Since by applying them consecutively on the same ion cloud, the only difference is in relative amplitudes due to different normalizations in the processing of the data. Nevertheless, creating this spectrum with the ‘zero-span’ ramp took 4 minutes, with the ‘direct LABVIEW fit’ it took 18 minutes and with the ‘later MATHEMATICA fit’ it took 6 minutes (plus the post-processing) and therefore, if it is not necessary to save more information, spectrum ramps are usually recorded in the ‘zero-span mode’.

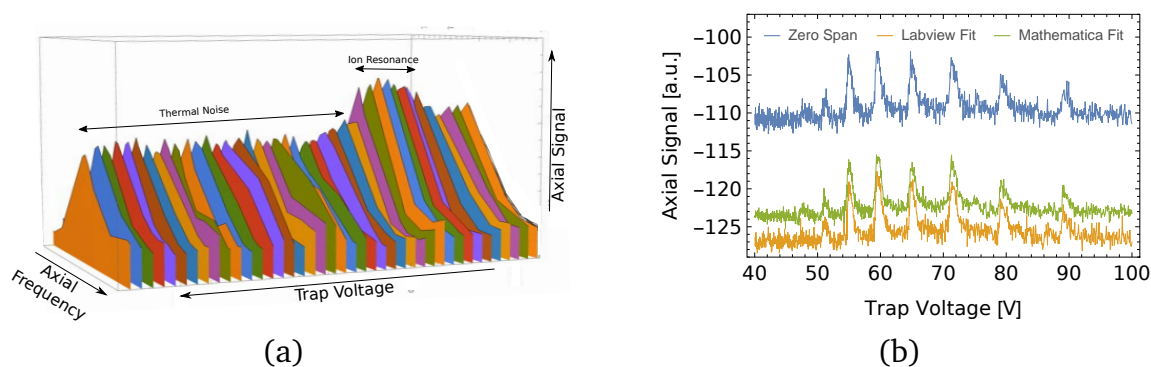


**Figure 5.3:** (a) Illustration of the unevaluated data taken with the ‘later MATHEMATICA fit’ method. For each voltage step a complete axial frequency spectrum is recorded; if the ions are in resonance with the resonator, the spectrum gets broader and therefore, by estimating the axial signal height and plotting it versus the trap voltage, the different ion species can be resolved by their charge-to-mass ratio. (b) With the three different methods of taking data a charge-to-mass ratio spectrum was created, thus, the results differ only slightly, merely an offset, due to the different normalizations in the processing of the data, can be seen.

## 5.2 Ion Creation

In the future, when ARTEMIS is connected to the HITRAP beamline, highly charged ions will be received from an EBIT or the GSI accelerator facility. At the current status, they are produced inside the trap with the mini-EBIS (Sec. 4.5.2):

As a reminder from the previous chapter: to create ions, first the potentials of the CT are set such that three harmonic traps are formed and the electron beam is switched on by applying a negative high voltage on the FEP (field-emission point) and a positive high voltage on the accelerator electrode. Additionally, the reflector electrodes H19 and H8/H9 are set to a potential 400 volts more negative than the FEP, so the electron beam is reflected back and forth over the length of the creation trap. The cryovalve is then heated and the air-pressurized valve opened for a time of 54 milliseconds and thus, the argon gas flows into the trap chamber, where the atoms are ionized and confined in the three traps. Further charge breeding takes place, since the trapped ions are furthermore exposed to the electron beam (Fig. 4.32).



After the charge-breeding time  $t_c$  the electron beam is switched off and the ions in the three traps are concentrated into the central trap C14<sup>4</sup> (Sec. 5.4.3). Alternatively, it is not always necessary to inject argon gas, since argon can also be sputtered from the walls of the trap that have argon frozen to the 4 kelvin cold surface. Only occasionally, when the creation efficiency decreases, new argon gas has to be inserted. Altogether, there are several parameters that can be tuned in order to create a suitable ion cloud including Ar<sup>13+</sup>.

---

### Field Emission Point (FEP) Voltage

---

The FEP voltage can be altered between voltages of  $-500$  volt and  $-3000$  volt with the energy of the electron beam closely related to it, thus, higher charge states can only be produced if the FEP voltage times the electron charge is above the ionization energy needed for this charge states (Tab. 5.1). Although the rate at which a charge state is created strongly depends on the FEP voltage, it should be noted that with higher voltages also the next higher charge state can be produced more efficiently and therefore, the total amount of the originally desired charge state decreases [92]. For example figure 5.4(a) shows an ion cloud that was produced with a FEP voltage of  $-1800$  volt and it contains more of the undesired higher charge states than Ar<sup>13+</sup>.

**Table 5.1:** Ionization energies (IE) for various argon charge states. Data taken from [93].

Charge State	17+	16+	15+	14+	13+	12+	11+	10+	9+	8+	7+
IE [eV]	4121	918	855	756	686	618	539	479	422	143	124

---

### Accelerator Voltage

---

The accelerator voltage is the main parameter for changing the electron-beam density, since, by applying higher voltages, the electrons are stronger attracted to the accelerator electrode, and therefore, more electrons will tunnel out of the FEP. With higher electron-beam densities higher charge states can be produced more efficiently, but additionally, with higher FEP currents the ion cloud gets heated stronger. Since the tip of the field-emission point degrades over time, the effective electron-beam density changes. Hence, the FEP current should be taken as a reference, thus making the ion creation more reproducible. In order not to harm the tip, the FEP current should never exceed 500 nA.

<sup>4</sup> ‘Trap C14’ denotes that the electrode C14 acts as the ring electrode and therefore, electrodes C13 and C15 are on the opposite potential, forming the endcaps and if not noted separately, all other electrodes in the creation trap are set to corresponding alternating potentials to form a harmonic trap.

---

---

## Breeding Time

---

The breeding time  $t_c$  defines the duration of how long the electron beam is switched on. Therefore, with a longer breeding time, higher charge states can be produced more efficiently, but since more electron impacts occur, the ion cloud gets heated stronger. For example, this can be seen by comparing figure 5.4(c) with figure 5.4(d).

---

---

## Argon Gas Pulse

---

For gas injection into the trap chamber, first the cryovalve is heated and then the pressurized-air valve is opened for a short period of time. This can be either carried out while the electron beam is active, or gas can be injected beforehand, such that some atoms will stick on the surface of the trap and when the electron beam is switched on will be sputtered and ionized.

---

---

## Creation Parameter Sets

---

Although in [94] the highest production rate for  $\text{Ar}^{13+}$  was found to be at a FEP voltage of  $-1.855$  kV, the calculations were carried out with many assumptions that are not known very precisely and therefore, additional measurements were performed in order to optimize the production of  $\text{Ar}^{13+}$ . Exemplarily, figure 5.4 shows the results for four interesting sets of parameters after some initial cooling. In this chapter, labeled lines are drawn in most figures and help to identify the different charge states. The theoretical positions of these lines were calculated and the whole pattern shifted (Sec. 5.3), such that it matches the positions of the center of the ion signals. However, in some figures, in order to visualize the shift from the ion signal to the theoretical values, the lines are drawn at the theoretically calculated positions and thus, this is noted in the caption.

- (a) Figure 5.4(a) shows a charge-to-mass spectrum of an ion cloud that was created with a high FEP voltage of  $-1.8$  kV, a high FEP current of  $370$  nA and a long breeding time of  $3$  min which leads to a production of higher to highest charge states. Plenty of  $\text{Ar}^{13+}$ ,  $\text{Ar}^{14+}$ ,  $\text{Ar}^{15+}$  and even  $\text{Ar}^{16+}$  ions are created.
- (b) Figure 5.4(b) represents the opposite, with a FEP voltage of only  $-780$  V, just slightly above the ionization potential of  $756$  eV for  $\text{Ar}^{14+}$ , together with a FEP current of  $240$  nA and again a long breeding time of  $3$  min it is not possible to create a sufficient amount of  $\text{Ar}^{13+}$  ions.
- (c) Figure 5.4(c) was generated by the so-called ‘hot’ ion creation, a parameter set frequently used. It comprises a FEP voltage of  $-1.6$  kV and a rather high FEP current of  $370$  nA with a long breeding time. This set of parameters is found to produce, relative to the other charge states, the highest amount of  $\text{Ar}^{13+}$  ions

but, due to the long breeding time and the high electron-beam density, the ions produced are quite hot and more additional cooling is needed afterwards.

- (d) Figure 5.4(d) shows the result of the parameter set referred to as the ‘cold’ ion creation. It is the second set of parameters that is used frequently and represents with a breeding time of only 1 second and the relatively low FEP current of 170 nA the most *gentle* way to ionize the gas atoms (more similar to the creation in [49]), resulting in a colder ion cloud. Although  $\text{Ar}^{12+}$  is more abundant than the desired charge state  $\text{Ar}^{13+}$ , the number of unambiguously distinguishable charge states as well as the reduced intensity of higher charge states compensates for this, since in section 5.8 it is shown that removing lower charge states is easier than removing higher charge states. Therefore this creation mode is the most appropriate one when aiming for a pure  $\text{Ar}^{13+}$  ion cloud.

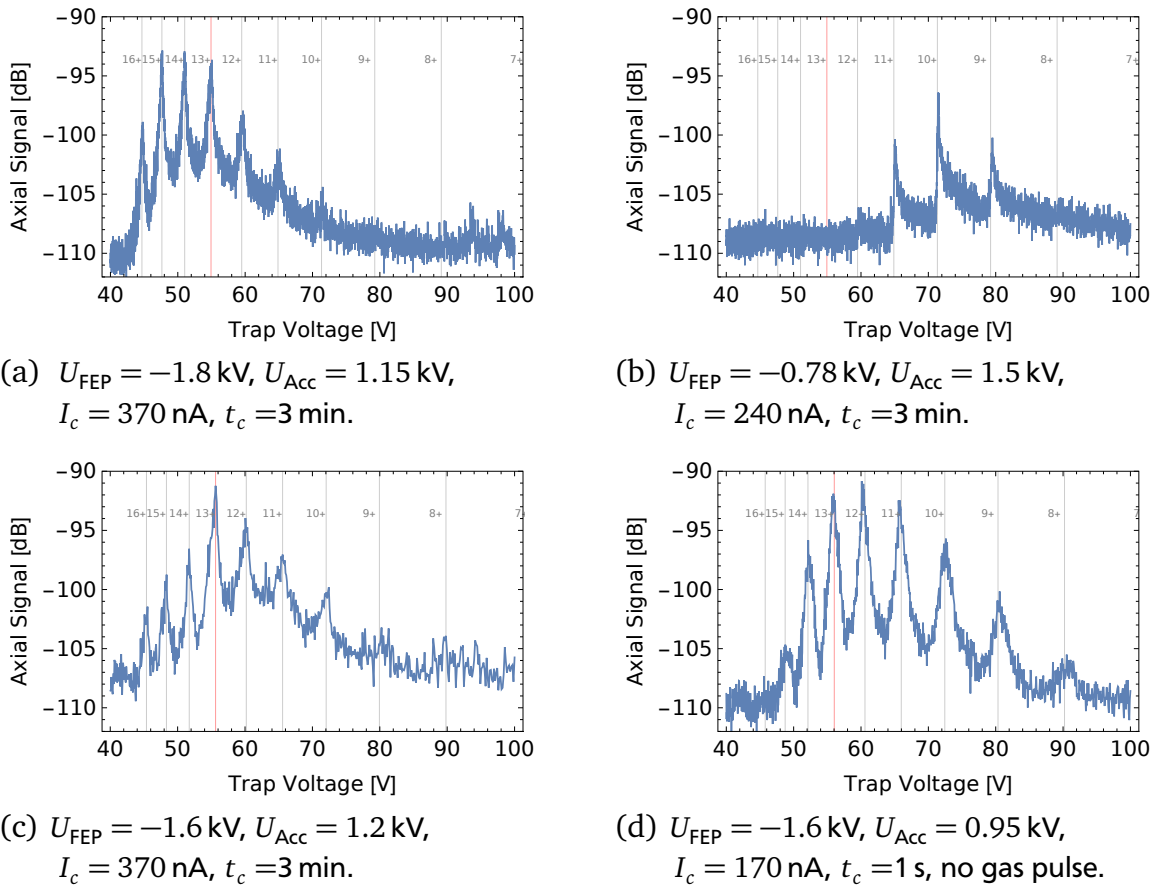


**Figure 5.4:** Charge-to-mass spectra of ion clouds that were created with four different sets of parameters, where  $U_{\text{FEP}}$  is the FEP voltage,  $U_{\text{Acc}}$  is the accelerator voltage,  $I_c$  the FEP current and  $t_c$  the breeding time. For better identification of the different charge states, lines with the corresponding charge state of argon are drawn which are shifted from the theoretical values. Please note that figures (a), (b) and (c) were recorded with the RIGOL SA.

---

## Tungsten Ions

---

Since the trap chamber does also contain other atom species due to the various materials used and since it also contains residual gas atoms, it is very likely that these atoms get ionized as well. In [18] it is already shown that, if the residual gas pressure is too high in the trap chamber,  $O^{5+}$  to  $O^{8+}$  can clearly be identified.

It was found that, if the accelerator voltage is very high and therefore the FEP current is in the order of many hundreds of nanoampere, it can lead to tungsten ions being produced in considerable quantities. The field-emission point, responsible for the electron beam, consists of tungsten, thus, by applying high FEP currents, tungsten atoms can be released from the tip and further ionized by the electron beam. As shown in figure 5.5 tungsten ions up to charge states of  $W^{27+}$  are visible. Table 5.2 gives some ionization energies for tungsten, hence, with a FEP voltage of  $-1.6$  kV theoretically even  $W^{36+}$  would be possible.

**Table 5.2:** Ionization energies (IE) for various tungsten charge states. Data taken from [95].

Charge State	37+	36+	28+	27+	26+	25+	24+	23+	22+	21+
IE [eV]	1622	1569	1132	881	833	784	734	686	641	595

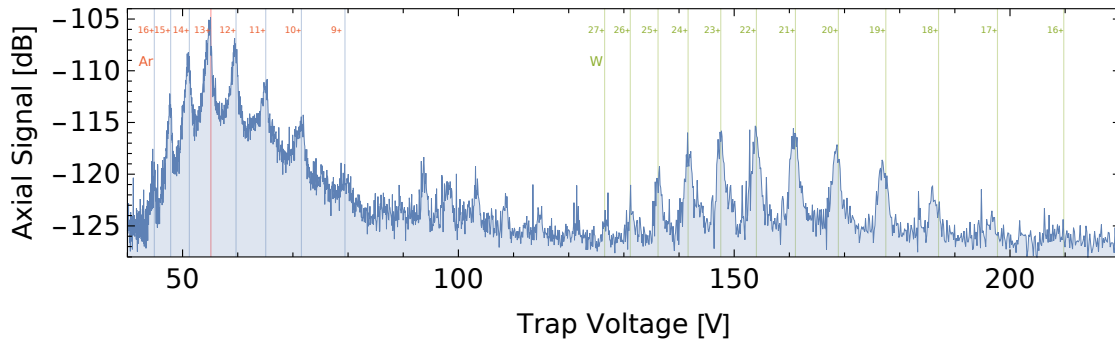


**Figure 5.5:** With high FEP currents tungsten atoms are released from the FEP, which consists of a sharp needle made of tungsten, ionized and trapped together with the argon ions. Due to further ionization, charge states up to  $W^{27+}$  can be identified. Please note, that for a better identification of the different charge states, the labeled lines are shifted from the theoretically calculated positions.

---

## 5.3 Ion Cooling

---

In Penning traps, in order to prepare cool ion clouds, various techniques can be applied, such as, for example, laser cooling [96] and resistive cooling [48]. This

section discusses the resistive cooling which has been applied to the axial motion of the cloud. With the help of axial cooling also magnetron centering was performed.

Resistive or ‘bolometric’ cooling takes place when the motion of the ions is brought into resonance with the detection circuit and therefore, via the image current  $I_p$ , power is transferred into the ohmic resistance  $R_p$  (Sec. 3.3) of the resonance circuit according to:

$$P_R = I_p^2 R_p. \quad (5.2)$$

Since the resonance circuit is located in a thermal bath at a temperature of 4 kelvin, the ion motion can therefore be cooled to that temperature. For a single ion with the three independent motions, an exponential decay of the axial kinetic energy can be expressed as

$$E_z(t) = E_z(0) e^{-\gamma t} \quad \text{with} \quad \gamma^{-1} = \tau = \frac{D^2 M}{R_p Q^2}, \quad (5.3)$$

where  $\tau$  is the cooling time constant which is dependent on the mass  $M$  and the charge  $Q$  of the cooled ion and on the ‘effective electrode distance’  $D$  that was first introduced in [49] and combines the geometry-dependent factors explained in [46]. A method to calculate  $D$  from the induced image current for cylindrical electrodes is given in [97] and is explained in [96].

For ions which are stored in the trap formed by the electrode C14 as the ring electrode and the ARES CT connected to the electrode C13,  $D$  can be calculated according to:

$$D^{-1} = \frac{-1}{\rho_0 \pi} \int_0^\infty \frac{I_0(x r / \rho_0)}{I_0(x)} \left[ \sin\left(x \frac{z - z_R}{\rho_0}\right) (z - z_R) - \sin\left(x \frac{z - z_L}{\rho_0}\right) (z - z_L) \right] dx, \quad (5.4)$$

where  $I_0(x)$  is the modified Bessel function of the first kind,  $\rho_0 = 8.704$  mm is the inner radius of the electrodes, and  $z_L = 7.456$  mm and  $z_R = z_L + z_{C13} = 21.568$  mm (where  $z_{C13}$  is the height of the C13 pick-up electrode) are the distances from the C14-trap center to the nearer edge of the C13 electrode and the distance to the further edge of the C13 electrode, respectively (Tab. 4.13).

For different axial and radial positions  $z$  and  $r$  equation 5.4 was calculated and the results are given in figure 5.6. The right ordinate of this figure additionally shows the corresponding cooling time constant  $\tau$  in the case of the ARES CT and  $\text{Ar}^{13+}$ . As it can be seen, the effective electrode distance  $D$  is strongly dependent on the axial and radial position of the ions – a change of almost one order of magnitude is possible and due to  $\tau \propto D^2$  the cooling time constant can easily vary by two orders of magnitude.

Although the theory of ion cooling of single ions or small clouds consisting of a few ions is well understood, for bigger ion clouds, and especially for such with different charge states, there is no model that can describe the behavior sufficiently; nevertheless, different models can be found, for example, in [35, 96].

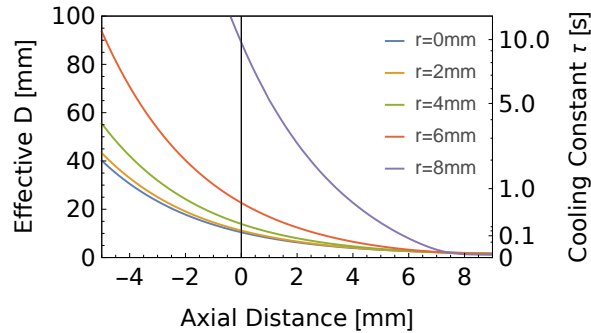


**Figure 5.6:** Calculated effective electrode distance as a function of the axial position  $z$  from the trap center for various radial positions  $r$ . The right ordinate additionally shows the corresponding cooling time constant  $\tau$  in the case of the ARES CT and  $\text{Ar}^{13+}$ .

---

## Axial Cooling

---

When the ions are in resonance with the resonator, energy from the motion of the ions is dissipated in the resonator that is cooled to cryogenic temperatures. Therefore, whenever a spectrum ramp is recorded, consecutively different ion species come into resonance for some limited period of time: in ARTEMIS, due to the energy distribution of the ions, the oscillations have a frequency distribution with a bandwidth of around 10 kilohertz which is several times larger than the bandwidth of the resonator with  $850 \pm 20$  hertz. Thus, depending on the step size (mostly 300 hertz), a certain ion species will be in resonance for several steps, hence, every spectrum ramp is also a cooling ramp with the amount of cooling dependent mostly on two parameters: the step size chosen and the scan time and therefore, how long the dwell time for each voltage step is (which is, when measuring with the zero-span mode and the usual settings, around 0.55 seconds). Figure 5.7 shows the typical evolution of an ion cloud that was created with a low current, a short breeding time and a FEP voltage of  $-1600$  volts, where consecutive cooling ramps were applied until the ion cloud is sufficiently cooled. Note that the cooling took place *during* each ramp and recording each ramp took about 5.5 minutes. Please note, that the voltage is ramped from higher to lower values.

- (a) Since the ion cloud is still hot, the first cooling ramp, directly after creation, shows a blurred signal which decreases from right to left as the ion cloud gets cooled.
- (b) The second ramp shows the ions after the first initial cooling where already some discrete peaks are visible, nevertheless the different charge states are not yet distinguishable.

- (c) After some more cooling ramps, *e.g.* after the 8th ramp, the charge states can be identified by shifting the lines of the theoretical values by a voltage of 5.2 volts to higher voltages. Since the ions are still hot, they are likely to be outside the harmonic part of the potential and therefore, their center frequencies are shifted.
- (d) The frequency shift decreases since the ions get cooled; nevertheless, it is still visible in this 17th ramp.
- (e) A large shift occurs when comparing the 17th to the 18th ramp (see also Fig. 5.8(b)); in the 18th ramp, the positions of the different ion species almost coincide with their theoretical values.
- (f) After further cooling, *e.g.* after the 88th ramp, a much colder ion cloud can be recorded. The asymmetries with an emphasis on the left stems from a non-vanishing  $C_4 < 0$  coefficient of the creation trap (Sec. 3.1) and could be used in tunable traps (for example in the ST) to tune out trap anharmonicities [47].

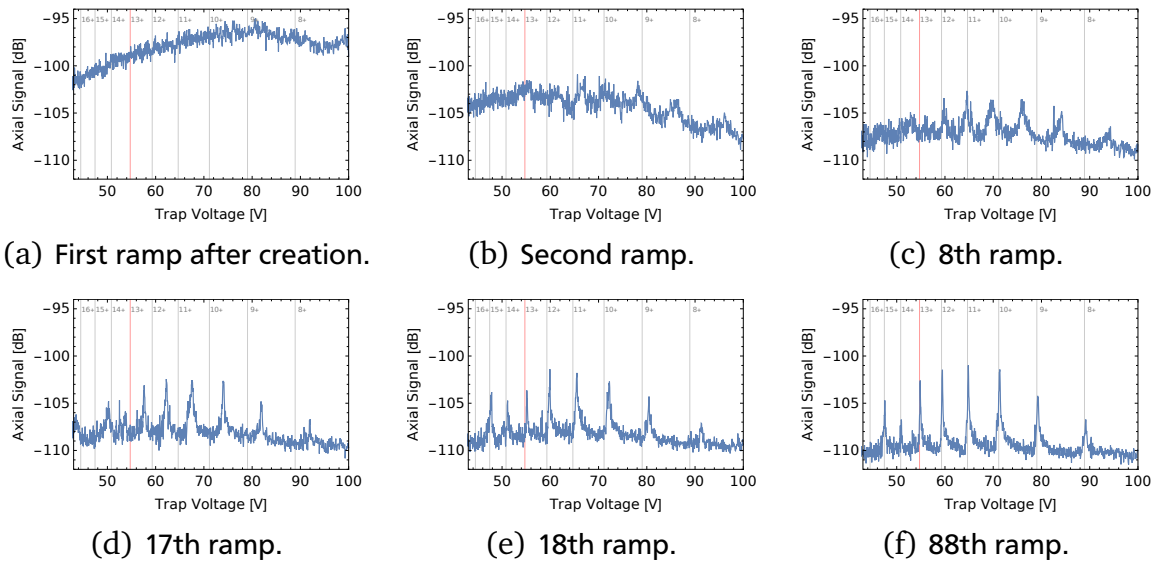


**Figure 5.7:** Consecutive cooling ramps after an ion cloud creation with a FEP voltage  $U_{\text{FEP}} = -1.6$  kV, an accelerator voltage  $U_{\text{acc}} = 0.95$  kV and the corresponding FEP current  $I_c = 170$  nA, with a breeding time of  $t_c = 1$  s and no gas pulse ('cold' ion creation, Sec. 5.2). The lines in the figures give the theoretical positions of a single argon ion with the corresponding charge state; more information about the spectra is given in the text.

Various spectra recorded by consecutive cooling ramps were evaluated and are given in figure 5.8: For figure 5.8(a) the mean value of the complete signal strength of every but the first spectrum ramp is calculated and plotted versus the number of the ramp; two sets of data were measured, each with a different step size (Sec. 5.1).

The axial motional frequency distribution depends on the energies of the ion motions. In the equations 3.11 it is shown that with a non-zero  $C_4$  the axial motional frequency is not only dependent on the axial motional energy but also on the magnetron motional energy and for a non-homogeneous magnetic field also on the modified magnetron motional energy. Since for higher energies the frequency distribution gets broader, the mean value of the signal is proportional to the motional energies, hence, gives a measure of the temperature of the ion cloud [98].

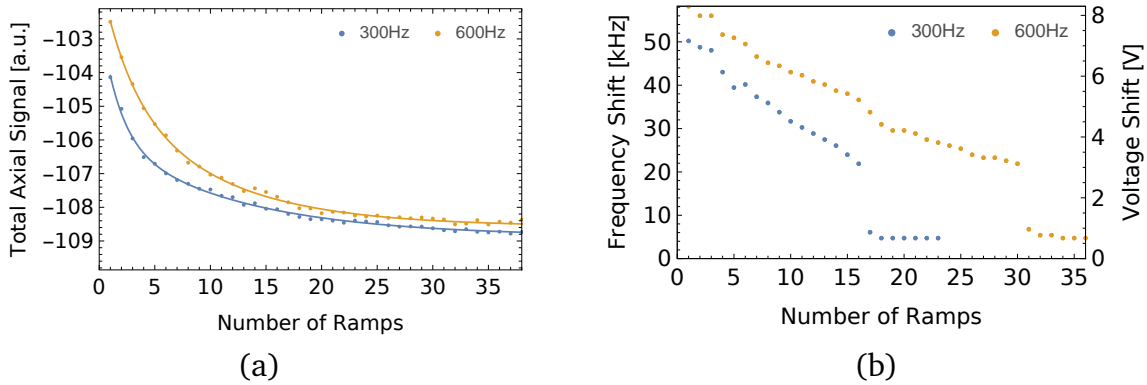


**Figure 5.8:** Two ion clouds have been cooled, each by a set of consecutive cooling ramps, one with a frequency step size of 300 Hz and the other with frequency step size of 600 Hz. (a) The mean value of the complete signal strength of each spectrum ramp is calculated and plotted versus the number of the ramp. Two exponential functions are fit to the data. (b) For each ramp the shift of the ions axial motional frequency to the theoretical value is determined and plotted against the number of the ramp.

In blue, with the standard step size of 300 hertz, the slower ramp, where every ramp takes 10 to 11 minutes to measure, is shown. In yellow, with a step size of 600 hertz, the faster ramp is given where every ramp takes 5 to 6 minutes. Two exponential functions are fit to the data and, with additional assumptions, the cooling time constants  $\tau$  for the first exponential function are  $\tau_{300\text{Hz}} = 73\text{ s}$  and  $\tau_{600\text{Hz}} = 24\text{ s}$ . The expected value for the cooling time constant from equation 5.4 would be in the range between 100 milliseconds to a maximum of a few seconds. Thus, the two measured and this theoretical value do not coincide. One reason might be the additional heating of the ion cloud which takes place, due to the fact that the trap voltage is reset and thus raised after each ramp. Additionally, since the ion cloud consists not only of many ions, but also of different charge states, the models which are suitable for few-ion systems cannot be applied anymore. For figure 5.8(b) the difference between the position of the different ion species and their corresponding theoretical values was determined and this shift is plotted versus the number of the ramp. At one point a strong non-linearity can be seen when the shift drops to almost zero which happens for both sets of measurements at almost the same frequency shift. However, a similar drop has also been seen in many other measurements. It cannot



be explained with usual cooling models, due to the various ion species and the large ion clouds. It is nevertheless important to account for that drop when implementing the so-called SWIFT cleaning technique (Sec. 5.8) that requires that the exact center axial motional frequency of the different ion species is known.

## Magnetron Centering

With the help of resistive cooling of the axial motion also centering of the magnetron motion by axial sideband coupling can be carried out. Figure 5.9(a) shows the principal concept for a single ion which utilizes the fact that the amplitude of the magnetron motion decreases, the more energy is deposited in it (Sec. 3.1): by irradiating the sum frequency of the axial and magnetron frequency  $\omega_z + \omega_-$  the magnetron motion gets more centered, but at the same time the amplitude of the axial motion increases. Therefore, by setting the trap potential such that the axial frequency is in resonance with the resonance circuit, the axial motion is cooled simultaneously, thus, counteracting the heating of the axial motion and resulting in a net magnetron motion centering [99].

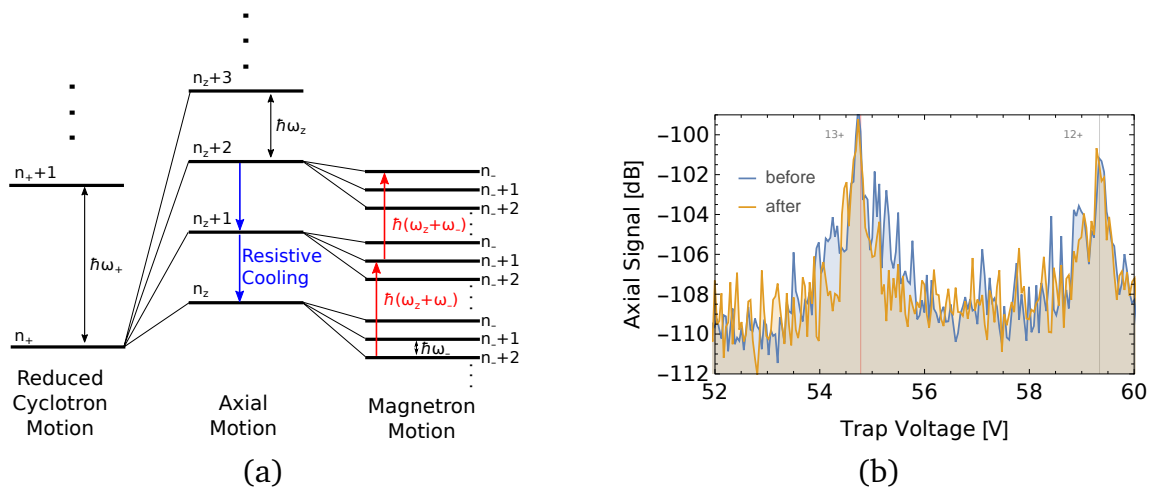


**Figure 5.9:** (a) The level scheme of the different quantized ion motions, similar to figure 3.4, illustrates the technique of axial sideband cooling: by irradiating the sum frequency of  $\omega_z + \omega_-$  energy is deposited in the axial motion and the magnetron motion. Therefore, the axial quantum number is increased and, since the magnetron motion is inverted, the magnetron quantum number is decreased at the same time. In order to counteract the increase in the axial amplitude, resistive cooling is applied which simultaneously cools the axial ion motion, thus, resulting in a net centering of the magnetron motion. (b) After irradiating the broadband signal containing the sum frequency of  $\omega_z + \omega_-$ , the axial motional frequency distribution of  $\text{Ar}^{13+}$  gets narrower since centering of the magnetron motion took place.

In section 3.2 the magnetron frequency is given according to:

$$\omega_- = \frac{\omega_c}{2} - \sqrt{\frac{\omega_c^2}{4} - \frac{\omega_z^2}{2}}, \quad (5.5)$$

which with a magnetic field of 7 tesla and an axial frequency of  $\omega_z = 2\pi \times 737$  kHz results in a magnetron frequency for  $\text{Ar}^{13+}$  of  $\omega_- = 2\pi \times 7.8$  kHz. Since the magnetic field in the creation trap is not known precisely and since it is not homogeneous, a broadband excitation (Sec. 5.8) was chosen when first trying the technique – the trap was set to a potential to continuously cool  $\text{Ar}^{13+}$  ions and meanwhile a broadband signal, consisting of  $10 \times 100$  bursts with 100 ms excitation time each and an excitation voltage of  $0.1 V_{pp}$ , ranging from  $\omega_z + 2\pi \times 4.3$  kHz to  $\omega_z + 2\pi \times 19$  kHz, was irradiated. Figure 5.9(b) shows the spectral distribution of the axial motional frequencies for  $\text{Ar}^{13+}$  and  $\text{Ar}^{12+}$  before and after irradiating the sum frequency and therefore applying magnetron centering – it can be seen that for  $\text{Ar}^{13+}$  the bandwidth of the distribution gets narrower.

---

## 5.4 Ions in the Creation Trap

---

This section focuses on some peculiarities of the creation trap which consists of nine similar electrodes that can form up to three traps where the center trap with the ring electrode C14 is most harmonic when an alternating potential on the electrodes is applied (Sec. 4.5). Since the trap chamber and all parts of the trap are cooled to a temperature of 4 kelvin, the so-called ‘cryo pumping’ leads to ultra-high vacua.

---

### 5.4.1 Residual Gas Pressure Estimation

---

Due to the good vacuum conditions, high charge states can exist for days or even weeks, since the rate of residual gas collisions, which would lead to charge exchange, is extremely low. This can be seen in figure 5.10 where a strongly cooled ion cloud was stored over the course of days and after a first spectrum ramp, two more were recorded after 24 hours and 48 hours. Additionally, the inset in the figure shows the change of the mean signal of the frequency distribution of each charge state in arbitrary units where the blue dots indicate the mean signal of the initial ramp, the yellow and the green dots the mean signal after 24 hours and 48 hours, respectively. During this time, charge exchange takes place. For example: the amount of highly charged  $\text{Ar}^{14+}$  ions gets smaller whereas the amount of lowly charged  $\text{Ar}^{8+}$  gets larger. Therefore, the residual gas pressure can be roughly estimated from the change in axial signal according to [21], were for a pure ion cloud this pressure can be estimated by

$$p = \frac{1}{\sigma t_c} \sqrt{\frac{k_B T \mu_m}{3}}, \quad (5.6)$$

where  $\sigma$  is the cross section for electron capture,  $k_B$  the Boltzmann constant and  $T$  the temperature of the ions. Additionally,  $t_c$  and  $\mu_m$  are given by

$$\mu_m = \frac{m_R m_i}{m_R + m_i} \quad \text{and} \quad t_c = \frac{t_1}{\ln \frac{N_0}{N_1}}, \quad (5.7)$$

where  $m_R$  and  $m_i$  are the mass of the residual gas atom and the mass of the ion.  $N_0$  is the initial amount of ions and  $N_1$  the amount of ions that is still there after the time  $t_1$  has passed. In the case of figure 5.10 one can take for example the axial signal of the  $\text{Ar}^{13+}$  ions at time  $t = 0$  and after  $t_1 = 48$  h. To make a conservative estimation it is assumed that all higher-charged ions that are lost become  $\text{Ar}^{13+}$ . With this, a decay constant of  $t_c = 78$  days is calculated. By assuming a charge-exchange cross section of roughly  $\sigma = 5 \times 10^{-15} \text{ cm}^2$  (for example [100] or the Müller-Salzborn fit from [21]) and a temperature of 4 K, an upper limit for the residual gas pressure is estimated to  $9 \times 10^{-16} \text{ mbar}$ .

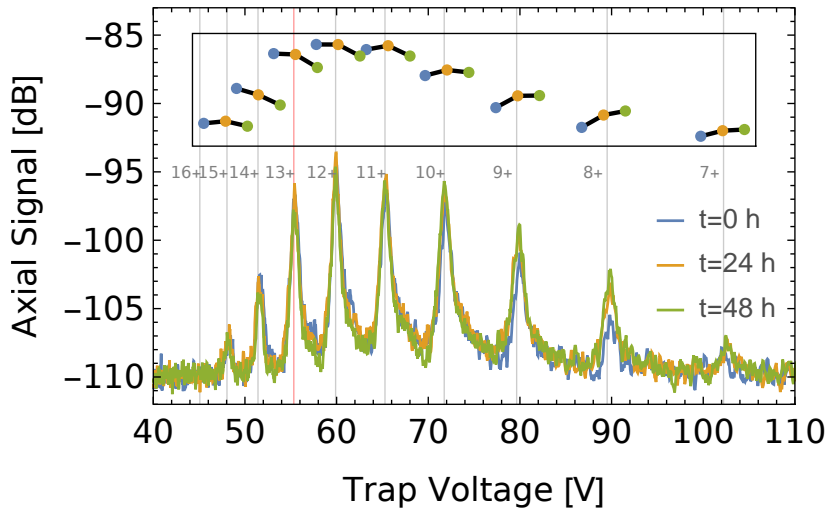


**Figure 5.10:** Spectra of highly charged argon ions after they have been trapped for one day and two days. The inset shows the evolution of the total signal of each corresponding charge state during this time in arbitrary units. With this lifetime an upper limit of the residual gas pressure of  $9 \times 10^{-16} \text{ mbar}$  was estimated. Please note, that for a better identification of the different charge states, the labeled lines are shifted by 1 V towards higher voltages compared to the theoretically calculated positions.

#### 5.4.2 Higher-Order Motion Seen by the Detector

With a certain preparation of an ion cloud in the creation trap, non-linearities of the detection system can be made visible: after a creation with a FEP voltage of  $-1.15 \text{ kV}$  and an accelerator voltage of  $1.9 \text{ kV}$ , leading to an FEP current of  $370 \text{ nA}$ , and after cooling for several hours, many fast spectrum ramps with small step sizes are carried out. They do not apply severe cooling, but excite the ions due to many fast changes in potential and therefore, the amplitude of the ions is increased.

With such a prepared ion cloud, it is possible to create a spectrum as shown in figure 5.11. Additionally to the usual  $\text{Ar}^{X+}$  charge state distribution another spectrum appears at lower voltages, at the position corresponding to a charge-to-mass ratio of 1.2. This position would leave only  $\text{H}^+$  as a potential candidate, but since also a pattern is visible, this signal must originate from something else: since the ARES CT is at the fix eigenfrequency of around  $\omega_0 = 2\pi \times 740$  kHz, when taking a spectrum, the voltage is ramped from higher to lower values which will induce a signal when the ions axial motional frequency  $\omega_z$  is also at  $2\pi \times 740$  kHz. At lower voltages, when the ions axial motional frequency is at around half the ARES CT frequency,  $\omega_0/2$ , and therefore at a quarter voltage ( $\omega_z \propto \sqrt{U_T}$ ) an additional signal is detected. This is due to the non-linear properties of the non-ideal ion cloud and detection system, hence, by having a finite ion cloud inducing a signal in the finite pick-up electrode. The ion motional frequencies therefore feature also higher harmonics, hence, when  $\omega_z = \omega_0/2$  the first higher harmonic will be at  $\omega_z$  and induce a signal into the the ARES CT. To illustrate this effect in figure 5.11, the signal is magnified four times ( $\omega_z \propto \sqrt{U_T}$ ) and depicted as an inset above the argon peaks, thus, showing the same position and separation between the peaks in both plots and the same relative height of the signals.

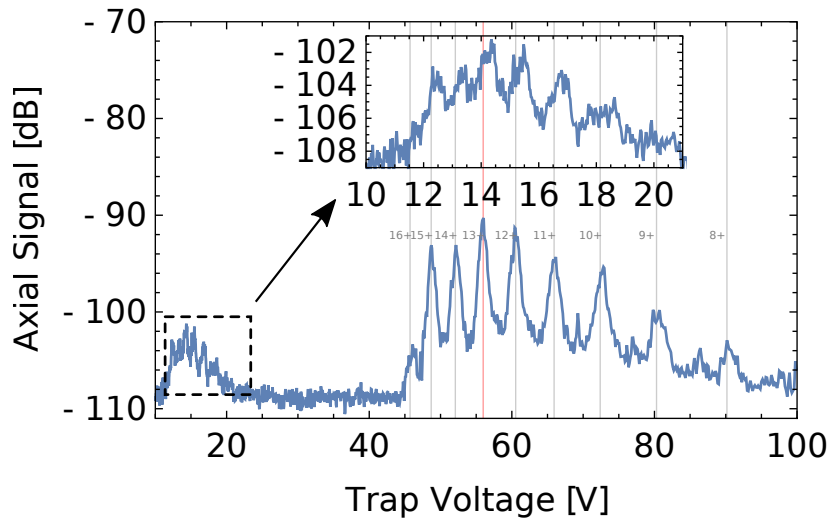


**Figure 5.11:** Charge-to-mass spectrum of an usual  $\text{Ar}^{X+}$  distribution on the right hand side with a structure on the left that can be identified as non-linearities of a non-ideal detection system showing higher order ion motions. Since  $\omega_z \propto \sqrt{U_T}$ , the structure can be four times magnified and shown as the inset with the center of the novel peaks of the structure coincide with the center of the peaks of the argon charge-state distribution. Please note that this figure was recorded by the RIGOL SA. Please note, that for a better identification of the different charge states, the labeled lines are shifted by 1.5 V towards higher voltages compared to the theoretically calculated positions.

### 5.4.3 Ions in the Trap with C12 as a Ring Electrode

When creating ions, all three traps in the creation trap store highly charged ions and therefore, after the electron beam is switched off, a transport procedure is applied in order to collect them in the center trap C14<sup>5</sup> (Fig. 5.12). Figure 5.13(a) shows a schematic of this transport procedure: first the potential of C13, that separates the traps C14 and C12, is lowered, resulting in a long flat potential well; afterwards the potential of C12 is raised followed by raising the potential of C13, hence, closing the trap. This procedure is then repeated for the ions in the C16 trap.

As already mentioned in the previous chapter, ARES CT is connected to electrode C13 and therefore can detect ions in the C14 trap as well as in the C12 trap. This is shown in figure 5.13(b) where the blue curve not only shows the typical pattern, but also different smaller peaks in-between which are caused by the signal of the ions stored in the C12 trap. Hence, in order to only store an ion cloud in the C14 trap, after the concentrating procedure a potential is applied corresponding to the last panel in figure 5.13(a) (*i.e.* lowering C11, C12, C16, C17) which removes all remaining ions in the traps C12 and C16.

Ions can also intentionally be transported into the C12 trap, where one would expect the same signal as when they are stored in the C14 trap due to the symmetry of C14 and C12 around the pickup electrode C13. Nevertheless, it is shown in figure 5.13(c) that this is not the case. On the one hand, this is due to the magnetic field which is not homogeneous in the region of the creation trap, and therefore a shift in the axial frequency occurs (Sec. 3.2). On the other hand, compared to the trap C14, the trap C12 does not have two neighboring traps that can shape its potential and therefore its  $C_4$  coefficient differs from the one of the C14 trap.

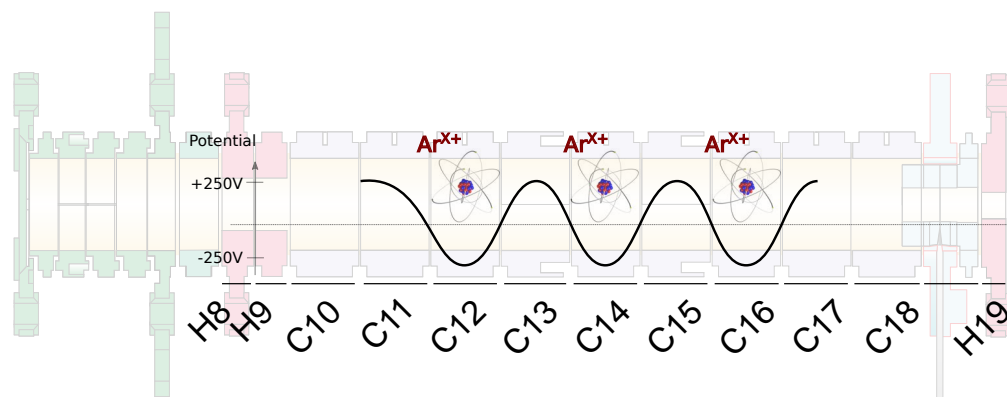


**Figure 5.12:** Scheme of three traps formed in the creation trap with ring electrodes C12, C14, and C16.

<sup>5</sup> Since every electrode in the creation trap can be used as a ring electrode with its neighboring electrodes as the corresponding endcaps, the ‘trap C14’ depicts a trap where the electrode C14 represents the ring electrode. Similar would ‘trap C12’ depict the trap where the electrode C12 represents the ring electrode and the electrodes C13 and C15 represent the endcap electrodes.

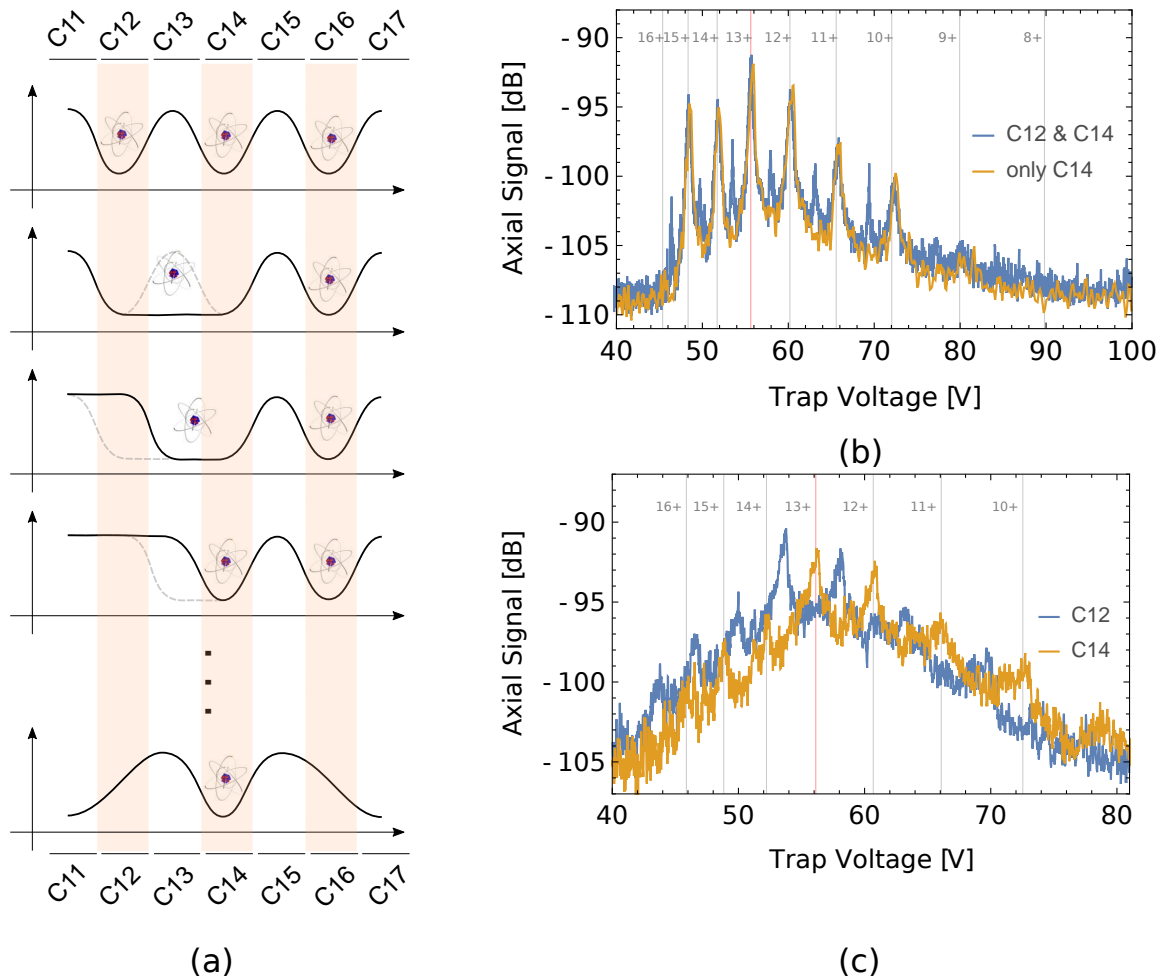


**Figure 5.13:** (a) Schematic of the ion concentration procedure applied after creation. After the ions from the C12 trap are merged with the ions in the trap C14 as shown in the first four panels, a similar procedure is applied to combine the ions in the trap C16 with the ions in the C14 trap. Finally, the potential is set according to the last panel, such that all remaining ions in the traps C12 and C16 are removed. (b) The blue ramp shows the signal of the ARES CT that is connected to electrode C13 and therefore can detect the ion motions in the trap C14 and additionally in the trap C12 where the peaks are shifted due to different  $C_4$  coefficients of the two traps. The yellow curve shows the ion signal after removing all remaining ions from C12, according to the last panel of the previous figure. (c) The ions are transported between the two traps C12 and C14 and although the shape of the ion cloud is similar, a frequency shift occurs due to the different  $C_4$  coefficients of the two traps and due to the inhomogeneous magnetic field in the CT. Please note that (b) and (c) were recorded by the RIGOL SA. The lines in the figures give the theoretical positions of a single argon ion with the corresponding charge state.

## 5.5 Ion Transport

After creating and cooling  $\text{Ar}^{X+}$  ions in the creation trap, they are transported into the spectroscopy trap in order to perform double-resonance spectroscopy. Although the transport into the spectroscopy trap is functioning, as it is shown in the next section (Sec. 5.6), transporting the ions back into the CT failed and was therefore investigated in more detail. Figure 5.14 shows a scheme of the transport procedure: the potential of electrode C13, the neighboring electrode to C14, is lowered, such that a flat potential well is formed with C13 and C14 being the ring electrodes. Afterwards electrode C14 is lifted, with the lifting is always carried out slowly. Since the filterboards do not allow switching times shorter than a few milliseconds, it is always slowly compared to the hundreds of kilohertz of the ion oscillation frequency. Finally the ions are stored in the trap C13 and similar procedures are repeated consecutively until the ions reach their destination.

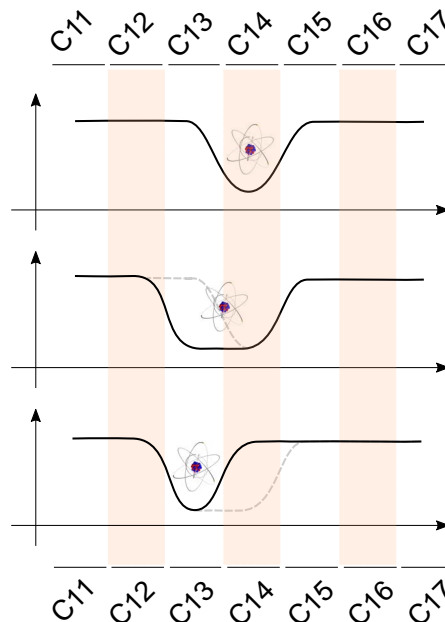


**Figure 5.14:** Scheme of one step of the transport procedure. The ions are stored in the trap C14 when the potential well ergo electrode C13 is lowered and a flat potential well is formed, afterwards, by raising the potential of electrode C14, the ions are stored in the trap C13. This procedure can be consecutively applied until the ions reach the desired trap.

To investigate some properties of the transport procedure, various measurements were conducted *e.g.* a cooled ion cloud was transported into the neighboring trap C12 and with a spectrum ramp it was assured that the signal originates from the ions in the trap C12 and the transport was successful. Afterwards the ions were transported back into C14 and another spectrum ramp was recorded. This was done consecutively and in figure 5.15(a) the total signal of the ramps in the trap C14 is plotted versus the number of transports. While after each transport the ions get heated,



every ramp applies additional cooling. Due to the broadening of the axial motional frequencies for higher motional energies (Eqn. 3.11), this cooling gets more efficient, the hotter the ion cloud gets, since the amount of voltage steps where the motional frequencies are in resonance with the ARES CT increases. Thus, an exponential function is fit to the data that indicates a saturation after around 50 transports.

In order to investigate multiple transports without applying too much additional cooling, additional multiple transports as shown in figure 5.15(b) were conducted. The ion cloud was transported another five times and afterwards a spectrum ramp was recorded – the argon ion charge states are still distinguishable. Subsequently, the ion cloud was transported another 1000 times and the corresponding spectrum ramp shows that the ions are still in the trap but much hotter and the signal therefore more blurred. Finally, after additional 10 000 transports to the trap C12 and back another spectrum was recorded and yet still some lower charge states like  $\text{Ar}^{10+}$ ,  $\text{Ar}^{9+}$  and  $\text{Ar}^{8+}$  remained in the trap. Since the transport was performed with the maximal voltage of  $\pm 250\text{V}$  applied to the electrodes, the ions are strongly bound axially and the only possibility a huge amount of ions can be lost is due to widening of the magnetron motion which is even enhanced compared to the ST, as the magnetic field gradient in the CT is quite large. Nevertheless, a significant loss of ions took place after the ion cloud was transported to the trap C12 and back in total 11025 times. After 1025 transports in total the ion cloud was hot, but no severe ion loss was encountered. Therefore it can be assumed that a single or only a few transports to the ST and back should not result in ion loss due to widening of the magnetron motion.

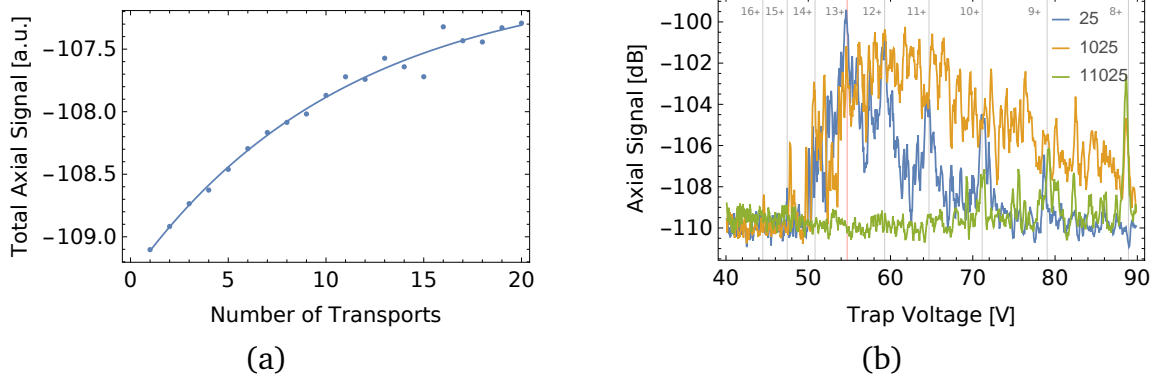


**Figure 5.15:** (a) An ion cloud is consecutively transported to the trap C12 and back to the trap C14. After each transport a spectrum ramp is recorded and the total signal of this spectrum is plotted versus the number of transports. Additionally, an exponential fit is applied to the data points. (b) Afterwards, the same ion cloud is transported additional 5 times, 1000 times and another 10 000 times to trap C12 and back to trap C14 and after each of the three sets of transports a spectrum ramp is recorded. The lines in the figures give the theoretical positions of a single argon ion with the corresponding charge state.



---

## 5.6 Ions in the Spectroscopy Trap

---

With a transport procedure similar to the one in figure 5.14, an ion cloud, created in the creation trap, was transported to the spectroscopy trap<sup>6</sup>. Figure 5.16 shows the charge-to-mass spectrum for such a transported ion cloud in blue after the transport. After a time of 100 minutes and 7 cooling ramps, another spectrum was recorded which is shown in yellow. Please note that in this figure the voltage applied to the ring electrode S3 is given, as it resembles the total trap voltage  $U_T$  since the ITO coated endcap electrode (S1) is grounded.

This measurement demonstrates that transporting  $\text{Ar}^{13+}$  ions into the spectroscopy trap is possible and therefore proves the functionality of the ITO-coated window as an endcap electrode. Unfortunately, the resonator in the spectroscopy trap broke shortly after recording this figure, so no further investigations of ions in the spectroscopy trap could be carried out.

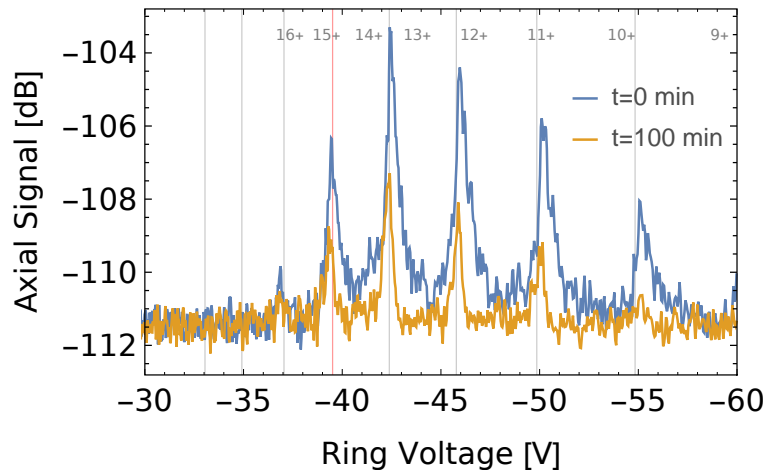


**Figure 5.16:** Signal of an ion cloud, after it was transported to the ST. The signal was recorded with the ARES ST and is shown by the blue curve, the yellow curve shows the ion signal after a time of 100 min had passed and 7 cooling cycles were applied. This figure was recorded by the RIGOL SA. The lines in the figures give the theoretical positions of a single argon ion with the corresponding charge state.

---

## 5.7 Cyclotron Frequency

---

Since the cyclotron resonator is connected to the spectroscopy trap, it is not possible to measure the modified cyclotron frequency  $\omega_+$  of the ions directly in the creation trap. Nevertheless, due to the ion clouds extent and the non-homogeneous magnetic

<sup>6</sup> This transport was carried out with the transport procedure ‘transport E14 to E3 extreme’: for the transport the voltages applied to all electrodes in the CT and the high voltage electrodes (C18-H8) are  $\pm 250$  V, but since the ST only allows voltages up to  $\pm 30$  V, the procedure is performed with this maximum voltage for the electrodes T7-S2.

field in the creation trap, the three different ion motions are coupled and this can be exploited to conduct a first measurement of the modified cyclotron frequency. Therefore, the ions were cooled and  $\text{Ar}^{13+}$  was brought into resonance with the ARES CT. A stepwise swept frequency scan near the expected modified cyclotron frequency was irradiated for a duration of 100 ms each step and after each step a ‘direct LABVIEW fit’ ramp was recorded. Figure 5.17 shows a typical ramp, the frequency is swept from lower to higher frequencies, where in the beginning a decrease of the axial signal occurs due to cooling the axial motion. After some frequency steps, at  $x$ -position 0 the ions’ modified cyclotron frequency  $\omega_+$  gets excited and once some thermalization time has passed (which in [101] is estimated to be under 10 ms), a part of the energy is also transferred into the axial motion and therefore, the signal rises. With rising axial amplitude, the magnetic field the ions are exposed to, changes due to the high magnetic field gradient at the position of C14. Therefore, the distribution of the modified cyclotron frequency of the ions gets broader and the acceptance of the RF-signal gets wider, until, after roughly  $2\pi \times 1.5$  kilohertz, they are not in resonance anymore and cooling takes place again.

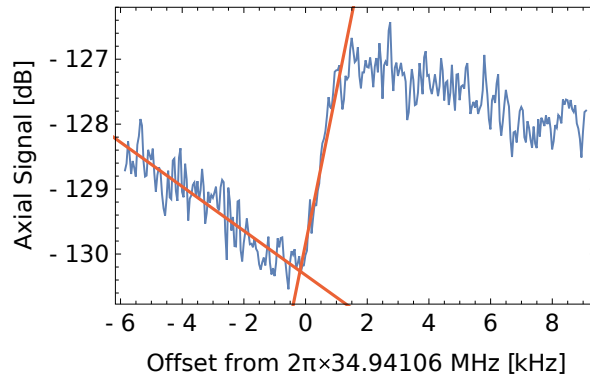


**Figure 5.17:** Typical data for the measurement of the modified cyclotron frequency  $\omega_+$  with the excitation method. A swept RF-signal is irradiated and the axial ion signal is detected. When the excitation frequency comes in resonance with the ions modified cyclotron motion some energy is transferred to the axial motion and can therefore be detected. The two red lines show two fitted linear functions and their intersection is considered the most likely value for  $\omega_+$ .

Around 20 of these ramps were taken and evaluated, with various excitation voltages between 0.06 and  $0.1 V_{pp}$ , various frequency windows and various frequency step sizes. For evaluation, two linear functions are fitted and the intersection is taken as the most probable value for  $\omega_+$  and plotted in figure 5.18(a), where the error bars result from the error of the line of best fit. From figure 5.18(a) the modified cyclotron frequency is determined to  $\omega_+ = 2\pi \times 34.94106(24)_{stat}(11)_{sm}$  MHz, with the first value for the error from the statistical distribution and the second error from the combined error in determining a single measurement. With the Brown-Gabrielse invariance theorem and the values  $\omega_z = 2\pi \times 729.2$  kHz (the axial frequency corresponding to the potential that was applied to the trap), and  $\omega_- = 2\pi \times 7.6$  kHz, the

accordingly calculated magnetron frequency, this results in a cyclotron frequency  $\omega_c = 34.948\,66(24)_{\text{stat}}(11)_{\text{sm}}$  MHz and thus in a magnetic field strength of

$$B = 7.000\,60(4)_{\text{stat}}(2)_{\text{sm}} \text{ T}, \quad (5.8)$$

which is plotted in figure 5.18(b) with the distance of electrode C14 from the trap center being 11 cm. Due to uncertainties in alignment and thermal contraction, for example temperature gradients in components connecting the 300 kelvin warm parts with the parts at a temperature of 4 kelvin, an additional horizontal error in the position of the ion cloud of  $\pm 3$  mm is assumed. Figure 5.18(b) shows the estimated value together with the theoretical and measured magnetic field data from VARIAN, the company that set up the magnet (Sec. 4.3) and although it looks like the value with its small error bars might suffer from a systematic effect that has not been taken into account, it should be stated that the magnetic field homogeneity in the region of the spectroscopy trap comes at the price of various shim-coils that are set around the field center and therefore, one cannot simply interpolate the measured field points by a straight line.

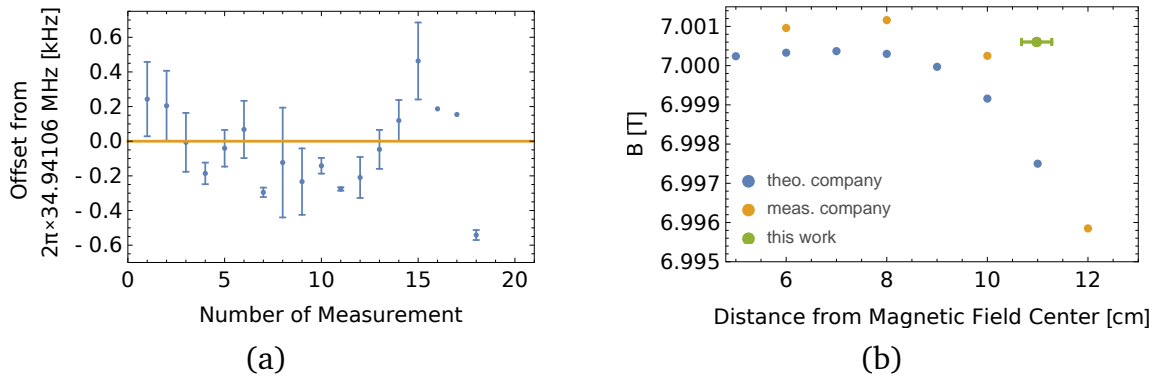


**Figure 5.18:** (a) Values for the modified cyclotron frequency for various data sets where the error bars account for the systematic uncertainty. From this figure the value for the cyclotron frequency was evaluated to be  $\omega_+ = 2\pi \times 34.941\,06$  MHz. (b) The determined value for the magnetic field strength at the position of the C14 electrode,  $B = 7.0006$  T, is plotted together with the theoretical and measured data from the company that set up the magnet. However, the vertical error bar is too small to be shown, whereas the horizontal error bar is due to uncertainties in alignment and thermal contraction and is in the order of  $\pm 3$  mm.

## 5.8 SWIFT

With selective excitation of different charge states it is possible to remove unwanted ion species from the trap via the so-called ‘SWIFT’ method. SWIFT stands for *Stored Waveform Inverse Fourier Transform* and is widely used in the community to ‘clean’ traps. The technique uses a fast Fourier transform to transfer a signal in the time

domain into the frequency domain. With the theory given in [102], this was implemented by M. Kiffer [101] into the LABVIEW program of ARTEMIS such that in the program various parameters can be set, for example the specific ion species or a frequency band and the program solves the integral relating the time domain with the frequency domain numerically and generates sample points of the corresponding signal. These points are then forwarded to the arbitrary waveform generator KEYSIGHT 33611A that can irradiate this signal into the trap. An example of such a signal, in this case a broadband excitation in the modified cyclotron domain, is given in figure 5.19.

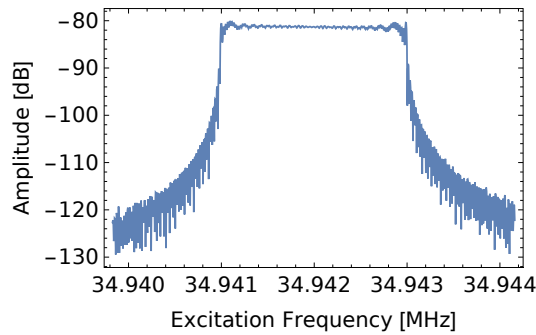


**Figure 5.19:** Broadband excitation signal, produced by the arbitrary waveform generator, which is irradiated into the trap via the electrode C15. In order to prevent strong overshooting, the so-called Gibbs-oscillations, the edges are rounded; also note that the flat top is intended and not an artifact such as, for example, saturation.

Two electrodes can be chosen for irradiating an excitation signal into the CT, the split electrode C15 for quadrupole (radial) excitation or the ring electrode C16 for dipole (axial) excitation. Since C15 is closer to the position of the ions which are in the trap C14, better results can be achieved by choosing one half of the split electrode C15 for axial excitation as well. To selectively remove ions, the desired ion species is excited, either radially or axially, and due to the coupling of the motions, parts of the energy is transferred into the axial motion. By lowering the potential to a value where the excited ions can overcome the potential walls, while the other ions are still confined, only the hot ions will be removed.

Due to Coulomb collisions, ion-ion interaction takes place and therefore energy is also transferred to the non-selected ions. This process is called thermalization and occurs with a time constant  $\tau_T$ , a complex relation of many parameters which, for a single ion species, can be calculated with the Spitzer self-collision formula:

$$\tau_T \approx (4\pi\epsilon_0)^2 \frac{3\sqrt{M}(k_B T)^{3/2}}{4\sqrt{\pi} n Q^4 \ln\Lambda} \text{ s}, \quad (5.9)$$

where  $\epsilon_0$  is the vacuum permittivity,  $M$  the mass of the ion,  $Q$  its charge,  $T$  the ions' temperature,  $n$  the ion number density and  $\Lambda$  is the Coulomb logarithm, a quantity from plasma physics representing the ratio between the maximum and minimum of all collision parameters possible [98].

An estimation for the lower limit of this thermalization time is carried out in [101] and yields  $\tau_T = 6.7$  ms. Since the filterboards have a time constant of 1 millisecond, it takes approximately 4 milliseconds to switch from trapping potential to the desired potential. Since this switching time is in the same order of magnitude as  $\tau_T$  and thus, the not excited ions might escape too, a fast switch is deployed that switches the voltage of electrode C14 from  $-250$  V to  $+250$  V which gives a much steeper rise in potential (Fig. 5.20(a)). Additionally, in order not to lose all ions due to a too shallow trap, once the desired trap depth is reached, the potential on C14 is switched back. Figure 5.20(a) shows a schematic of the SWIFT procedure with fast switching: the SWIFT signal is irradiated for a time  $t_{\text{signal}}$  and afterwards the applied voltage at C14 is switched to  $+250$  V until the time  $t_{\text{switch}}$  has passed, then the applied voltage is switched back to  $-250$  V. Figure 5.20(b) shows the corresponding potential wells; the voltages of the neighboring electrodes C13 and C15 are set to a voltage of  $+10$  V such that the removed ions, which overcome this barrier, will not be halted by stray potentials but either fly into the grounded ITO-coated window or are lost at the lower end of the trap chamber. During irradiation, the trap voltage is always set to  $-250$  V at C14 and  $+10$  V at C13 and C15. The other electrodes in the creation trap are set to the corresponding alternating voltages to create a harmonic trap in C14 with a trapping voltage of  $U_T = 260$  V.

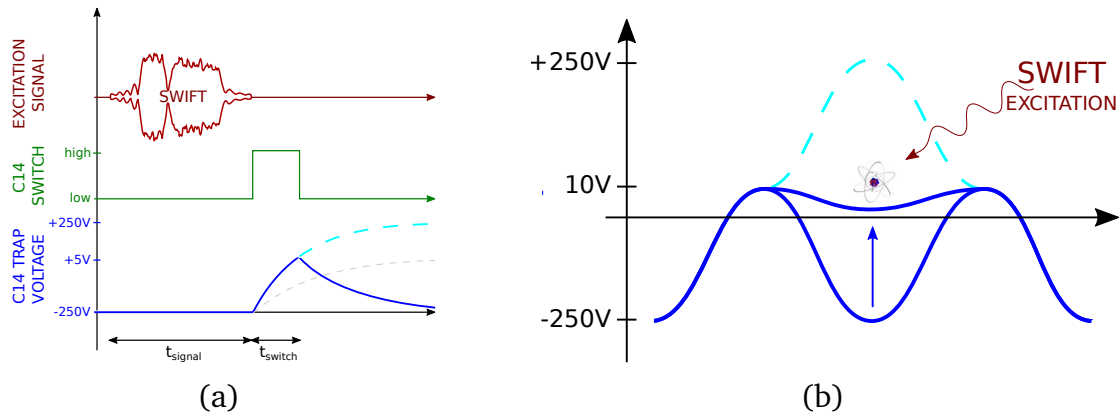


**Figure 5.20:** (a) Schematic of the SWIFT procedure with fast switching in order to bypass the 1 ms filterboard time constant. After irradiating the excitation signal, the potential applied to the ring electrode is switched to  $+250$  V, resulting in a faster rise in the trap voltage (blue) than it would be the case by usual switching (gray). (b) The corresponding potential wells are shown, where after the time  $t_{\text{switch}}$  a shallow trap is formed where the previously excited ions can escape before thermalizing with the other ions.

To find the optimal switching time  $t_{\text{switch}}$ , a measurement was conducted where an ion cloud was stored in the trap C14 and the potential well was switched to  $+250$  V with switching times that gradually became longer and after each step a spectrum was recorded. Figure 5.21 shows the total axial signal versus the different switching times  $t_{\text{switch}}$ . In the beginning, for short switching times where the trap is still sufficiently deep, no ions can escape, the ion cloud is solely heated up, until the

potential well gets shallow enough so parts of the cloud escape. This measurement was carried out for differently cooled ion clouds. An optimum switching time of  $t_{\text{switch}} = 600 \mu\text{s}$  was found.

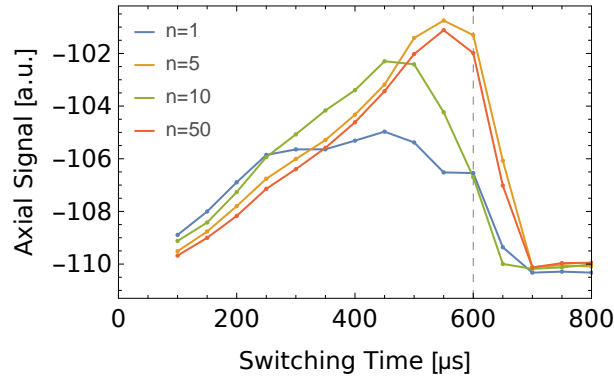


**Figure 5.21:** Measurement to get the best value for  $t_{\text{switch}}$ . By increasing the switching time from 0 to 800  $\mu\text{s}$  consecutively, the switching time is found where the potential well gets too shallow and all ions can escape. This is performed with different ion clouds with a different amount  $n$  of cooling cycles beforehand.

According to [101] the excitation voltages should be in the order of  $100 V_{\text{pp}}$ . However, the voltage limit of the filterboards limits the signal strength to  $10 V_{\text{pp}}$  and therefore, for each measurement, a large number of cycles of signal irradiation and fast potential change have to be repeated. Thus, a set of good parameters for removing ions in an ion cloud by axial excitation in ARTEMIS was found to be 1000 bursts of 1 ms excitation time with an excitation voltage of  $8 V_{\text{pp}}$  and 600  $\mu\text{s}$  switching time.

Although the SWIFT technique is perfectly suited to address ion species directly by tailored signals, in the case of ARTEMIS it is utilized to create signals for a broadband excitation with sharp edges, since selective excitation works better with smaller or sufficiently cooled ion clouds where the axial frequency is better defined.

Nevertheless, it is beneficial to perform magnetron centering occasionally, since it makes the ion signals narrower and therefore reduces the risk of false ion excitation. Additionally, removing all unwanted ion species to obtain a pure  $\text{Ar}^{13+}$  ion cloud can be achieved for an ion cloud created by the ‘hot’ creation; with long breeding times, high FEP currents and sufficient cooling afterwards which can take up to one day. This method has the advantage that  $\text{Ar}^{13+}$  will be the most abundant species and therefore, the overall number of  $\text{Ar}^{13+}$  ions is the highest. Alternatively, by producing ions via the ‘cold’ ion creation, an ion cloud is created that is fast to cool, thus, after a few cooling cycles, the first excitation can take place. This turned out to be more time efficient and since the different ion species are additionally more distinguishable, easier selection of the target charge states, that should be removed, is possible.

Figure 5.22 shows a typical procedure where an ion cloud was produced by the ‘cold’ ion creation and all ion species except of  $\text{Ar}^{13+}$  are successively removed. Please note that in this figure the red squares depict the voltage window to be se-

lected after the respective ramp for the spectrum which was then translated into the corresponding excitation frequency for the ions being stored at a trap voltage of  $U_T = 260$  V. Additionally, between the different spectra, before the spectrum ramp was recorded, several cooling ramps took place.

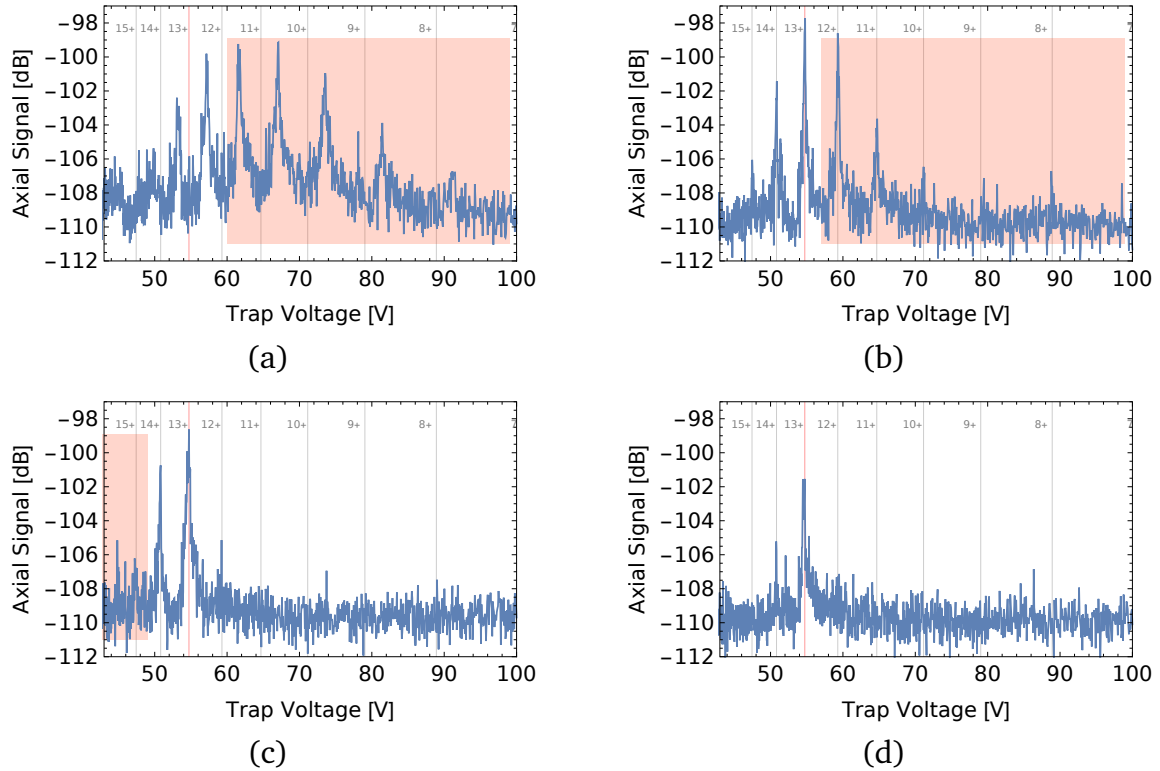


**Figure 5.22:** Typical sequence of the SWIFT cleaning technique to get a pure  $\text{Ar}^{13+}$  ion cloud, where the red squares depict the chosen voltage window which was translated into the corresponding excitation frequency for the SWIFT broadband excitation. The excitation took place after the respective spectrum was recorded. More information is given in the text. The lines in the figures give the theoretical positions of a single argon ion with the corresponding charge state.

- (a) Figure 5.22(a) shows the initial ion cloud after previous cooling, where the ions are still shifted with respect to the theoretical values and therefore a first broadband excitation far off of the  $\text{Ar}^{13+}$  frequency ions was irradiated with a frequency span from  $2\pi \times 487$  kHz to  $2\pi \times 377$  kHz which corresponds to a window in the voltage picture from 60 to 100 V.
- (b) Figure 5.22(b) shows that ions with lower charge states,  $\text{Ar}^{8+}$ ,  $\text{Ar}^{9+}$ ,  $\text{Ar}^{10+}$  and already plenty of  $\text{Ar}^{11+}$ , were removed from the trap, however,  $\text{Ar}^{12+}$  remained: during excitation, when the ion cloud got hotter, the axial oscillation frequencies of all ions increased, which, in the voltage picture, led to a shift to lower voltages, and therefore the  $\text{Ar}^{12+}$  ions were not excited by the previously chosen frequency window. Additionally, after the ions were removed, the positions

---

of the remaining ions shifted more to their theoretical values and therefore another broadband signal from  $2\pi \times 499$  kHz to  $2\pi \times 377$  kHz was irradiated, corresponding to a window from 57 to 100 V in the voltage picture, which due to the narrower, easier to distinguish peaks could be much closer to the right slope of the  $\text{Ar}^{13+}$  peak.

- (c) In figure 5.22(c) it is shown that all charge states lower than  $\text{Ar}^{13+}$  were removed, nevertheless, exciting the higher charge states is more complicated due to the aforementioned frequency shift, since there is a chance of exciting the wrong ion species when choosing an excitation frequency too close to  $\text{Ar}^{13+}$ . Therefore a frequency window from  $2\pi \times 687$  kHz to  $2\pi \times 538$  kHz, that translates in the voltage picture to 30 to 49 V, is irradiated which, although it does not cover the  $\text{Ar}^{14+}$  peak in the figure, is able to excite and remove the  $\text{Ar}^{14+}$  ions.
- (d) The last figure, Fig. 5.22(d), shows the end result of the SWIFT technique with fast potential switching: almost all higher- and lower-charged ions were removed from the trap, and although some  $\text{Ar}^{13+}$  ions were lost compared to the signal in figure 5.22(a), a cold, pure  $\text{Ar}^{13+}$  ion cloud was created.



---

## 6 Summary, Improvements and Outlook

During this work, the ARTEMIS apparatus was assembled and preliminary studies for the later  $g$ -factor measurements were conducted, which led to the preparation of a cold, pure  $\text{Ar}^{13+}$  ion cloud (Sec. 5.8). Together with the demonstrated successful transport to the spectroscopy trap (Sec. 5.5), the foundations were laid in order to perform the double-resonance spectroscopy. Two measurement times were carried out: the first one, in 2015, is reported in [18], whereas the second one, in 2016, is reported in this thesis. Between the two measurement times, the apparatus was disassembled and improvements were implemented as summarized in the beginning of chapter 5.

For the laser excitation, several improvements were made, improving the fluorescence light efficiency. Together with A. Martin, the optics holder was redesigned and with the new bare-fiber holder, less fluorescence light gets blocked ([50], Sec. 4.3.3). Another major change was the replacement of the mesh of the S1 endcap electrode by the ITO-coated window, which led to an improvement in transmissibility of at least 17% (Sec. 4.5.1). Additionally, the ITO-coated window will also decrease the anharmonicities due to its more planar structure. It represents a novel concept for Penning traps and gives the possibility of providing closed endcaps with high optical transmission. Therefore, a ring electrode consisting of ITO-coated glass could also be envisaged, for example for radial detection of fluorescence light as in the SPECTRAP-experiment [103].

Since the laser system built by A. Martin was already operational [50], preliminary measurements were conducted in order to detect fluorescence light, but without showing a significant signal. Nevertheless, these measurements were performed on a not yet sufficiently prepared ion cloud and therefore, for the next measurement time, the premises should be according to the following list:

- With the SWIFT-technique the ion cloud should be purified, such that  $\text{Ar}^{13+}$  is by far the most abundant charge state and a large amount of them should be compiled in the ST by repeated ‘stacking’<sup>1</sup>.

---

<sup>1</sup> Stacking describes the technique, where an ion cloud, that is produced in the CT, is transported into the ST and then another ion cloud is produced, transported and combined with the first cloud. This was already performed by the author in the 2015 measurement time with  $\text{O}^{5+}$  and  $\text{O}^{6+}$  with up to 8 ‘stacks’, which means this technique was repeated until 8 ion clouds were combined [18].

- The ion cloud needs to be sufficiently cooled in the ST and the correction electrodes need to be tuned, such that the shape of the ion signal gets symmetric ( $C_4 = 0$ , Sec. 3.2.1) and therefore the ST is harmonic.
- By applying the technique of rotating wall, the density of the ion cloud can be maximized, thus, increasing the amount of ions that are excited.

Unfortunately, since the ARES ST broke shortly after a few successful transports into the ST were reported, it was not possible to accomplish these requirements in the 2016 measurement time. After the failure of the ARES ST, in order to optimize the transport, several attempts were made to transport the ions into the ST and back – since there was no direct detection of the ions in the ST. However, this was not possible since no ion signal could be detected after the transport back to trap centered at the electrode C14. Therefore, the transport from the C14 trap in the next trap at C12 (Sec. 5.5) was investigated which ruled out the widening of the magnetron motion as the cause of the malfunctioning transport. One cause of the failing transport might be the electrodes H8/9 which have a smaller diameter than the rest of the trap. Tapering their edges or widening their diameter might yield a solution. Nevertheless, the transport *into* the ST works and the cause of the malfunctioning back-transport can be investigated more analytically with a detector in the ST.

Once the laser spectroscopy has been carried out successfully, in order to perform the double-resonance spectroscopy, a tunable microwave field at the position of the ions is needed. Therefore, a microwave system for microwaves with a frequency of around 65 gigahertz was built and tested, resulting in a power of the microwaves of at least 50 microwatt (Sec. 4.4). Nevertheless, for the complete measurement of the higher-order Zeeman effect, also a system that provides microwaves with a frequency of 130 gigahertz is needed. Due to the usage of the cryogenic coaxial cable in the microwave design at 65 gigahertz, it was possible to connect the room-temperature warm environment with the cryogenic temperatures cold detection housing without creating too much heat load (Sec. 4.4.4). However, since coaxial cables are not available for the high frequencies of 130 gigahertz, a waveguide needs to be deployed that combines low thermal conductivity with high electrical conductivity, such as silver coated stainless steel. Nevertheless, due to the difficult geometry on the top of the magnet, the waveguide has to be bend multiple times and then threaded into this geometry. However, another approach might be to double the microwaves in the cryogenic environment, for example, by developing a frequency-doubling stage on the basis of local heated semi-conductors as it is deployed in the varactor-diode board by STAHL ELECTRONICS.

In the measurement time of 2015 a vacuum of  $4 \times 10^{-13}$  mbar was estimated from the lifetime of the  $\text{Ar}^{16+}$  charge state. This value was improved to  $9 \times 10^{-16}$  mbar (Sec. 5.4.1) by decreasing the leak rate of the gas inlet system. Therefore, much longer storage times of HCIs are reached and this sufficiently proves the validity of the concept of the cryovalve ([51], Sec. 4.5.2), where a quasi-open connection between two vacua can separate them by cooling the open connection to cryogenic

---

temperatures. Thus, this gives impetus to the idea of replacing the fast opening valve (FOV) by a design with a cryogenically cooled cylinder that is filled with several plates, parallel to the endcaps and with a hole in their middle, thus shaping a baffled structure with a tube-like hole for a direct path for the ion beam. According to the simulations performed in [54], a cryogenic tube is already sufficient to separate two vacua by at least 5 orders of magnitude. The baffled structure and a piezo-driven shutter should increase this by far, thus, representing an alternative to the FOV. However, the FOV was assembled and tested (Sec. 4.6) and in room-temperature its functionality was proven. Nevertheless, improvements, such as stronger magnets, have to be implemented since reliability was not given all the time. Additionally, a cryogenic test would be needed in order to test the general mechanical functionality as well as the performance in separating the two vacua at low temperatures.

Since the eigenfrequency of the CRES was at a too high value in the 2015 measurement time, an additional board was implemented in this work with a varactor diode with which, at room-temperature, it was possible to shift the frequency over a range of a few megahertz and therefore also shifting it to the desired frequency of 35 megahertz. Nevertheless, after cooling the board down to cryogenic temperatures, the shifting-range decreased severely. Additional test experiments in the HILITE experiment showed that the combination of temperatures under 10 kelvin and high magnetic fields of a few tesla causes a problem in the varactor diodes (Sec. 4.3.2). Both influences had been tested separately beforehand, but the effect on the varactor diode with a strong magnetic field and cryogenic temperatures combined was observed for the first time. Therefore, for the upcoming measurement time, a varactor-diode board from STAHL ELECTRONICS was installed and thus, the varactor diode can be heated locally over the critical temperature without heating all other cryogenic parts. Thus, a direct measurement of the modified cyclotron frequency in the ST should be possible.

Since measuring the modified cyclotron frequency directly in the ST with the CRES was not possible, another method was deployed with which this frequency,  $\omega_+$ , was measured indirectly in the creation trap (Sec. 5.7). The irradiated modified cyclotron frequency was swept and, since some of the energy absorbed by the ion was also transferred into the axial motion, measuring the axial frequency yielded a value for  $\omega_+$ . Therefore, a magnetic field in the CT at the position of electrode C14 of  $B = 7.000\,60(4)_{\text{stat}}(2)_{\text{sm}}\text{ T}$  was estimated. Although this method represents a more imprecise alternative to the measurement with the cyclotron resonator, it is also used in other experiments for determining the strength of the magnetic field gradient [47].

Most mechanical parts of ARTEMIS were designed in the course of this work and the complete setup was drawn in a CAD program. The cryogenic concept from the author's diploma thesis [52] with the vibration isolation due to the stranded copper wires was implemented (Sec. 4.2) and preliminary tests of the complete cryogenic setup were carried out. The apparatus was completely assembled and in the measurement time of 2015 first ions were created [18]. In the beginning of the 2016 measurement time a systematic analysis of the creation parameters was conducted,

---

yielding two sets of parameters for the production of an applicable argon ion cloud (Sec. 5.2). Additionally, measurements were recorded to investigate the ion cooling which yielded an exponential decay with a cooling time constant of several tens of seconds, which was found to be too high and thus, more detailed investigation has to be carried out. The shifting of the axial frequencies was also studied and a non-linear behavior was found after some time, when an ion cloud was cooled (Sec. 5.3).

Since it was shown that the FEP current is not only dependent on the accelerator voltage, but also changes over time, the FEP current should be the dominant parameter with the accelerator voltage depending on it. As an improvement, to make the ion production more reproducible, the HV-FEP should be modified according to this by the company.

The next steps for the ARTEMIS project should include the repeating of the preparation of a cooled, pure  $\text{Ar}^{13+}$  cloud and its transport into the ST in order to perform the laser-spectroscopic measurement of the finestructure transition. Afterwards, the double-resonance spectroscopy should be carried out and with the CRES a precise measurement of the magnetic field in the ST should be executed. The setup should then be improved and the microwave system for the 130 gigahertz implemented. With this system the  $g$ -factor as well as the higher-order Zeeman shifts of boron-like argon can be measured.

Meanwhile the connection to the HITRAP beamline will be finished and therefore, either the FOV or a cryogenic alternative should be tested and deployed. Concurrently, the UMF and the trap chamber should be redesigned. With the EBIT on the HITRAP platform preliminary tests for the beamline, the injection into the trap, and the valve separating the trap vacuum from the beam vacuum can be performed. Finally, the GSI accelerator facility will deliver hydrogen-like heavy ions, such as  $^{209}\text{Bi}^{82+}$ . Their electron and nuclear magnetic moment can be measured and hereby, more stringent tests of the bound-state QED in extreme fields will be accessible.

---

# A Appendix

---

## A.1 Damping of Cryocooler Vibrations

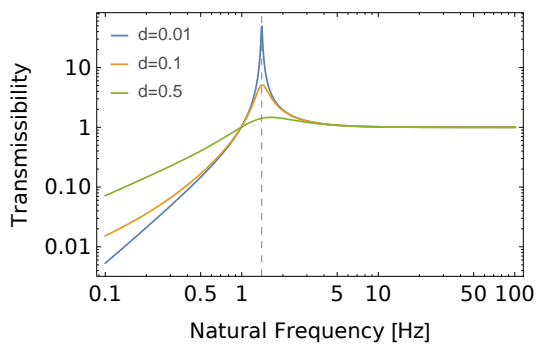
---

If it turns out that measurements suffer from too strong vibrations, maybe some additional improvement in the current vibration isolation system has to be implemented. The isolation is currently performed at three points. The first point is the connection of the cryogenic parts via the stranded copper wires described in 4.2. These stranded wires need to be long and loose enough to provide a decent vibration isolation, which should be the case. The other two points might be more severe: the rubber granulate mat and the edge welded bellows. During a research stay at Harvard University in the group of Gerald Gabrielse some thoughts about the vibration isolation with edge welded bellows were conceived. These thoughts were about the reliquifier at the  $g$ -2 measurement, which consists of a cryocooler that, by a special design, receives the boiled off helium of the experiment and liquifies it again in order to reinsert it into the dewar. The cryocooler for that experiment suffers from the same vibrations with a frequency of 1.4 Hz as the cryocooler of ARTEMIS does. These very low frequency vibrations are hard to decouple. The transmissibility  $T$  gives the percentage (amplitude ratio) of the transmitted vibrations between an object that is vibrating with a driving frequency  $f_d$ , through a connection with damping  $d$  and natural frequency  $f_n$ :

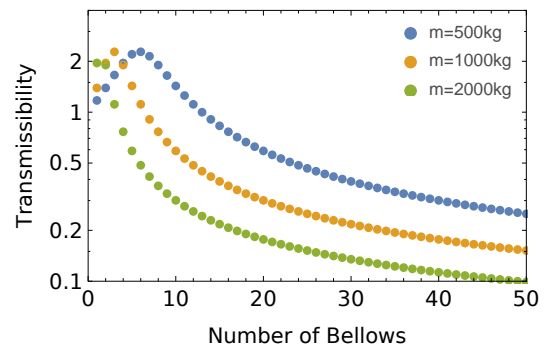
$$T = \sqrt{\frac{1 + \left(2d\frac{f_d}{f_n}\right)^2}{\left(1 - \left(\frac{f_d}{f_n}\right)^2\right)^2 + \left(2d\frac{f_d}{f_n}\right)^2}}. \quad (\text{A.1})$$

In figure A.1(a) this is shown for different damping constants. It can be seen that the natural frequency needs to be lower than the driving frequency.

The natural frequency of an object with mass  $m$  is directly related to the spring constant that connects the object with the source of vibration  $2\pi \times f_n = \sqrt{\frac{k}{m}}$ . So either smaller spring constants or larger masses help to minimize the transmissibility. For example, for edge welded bellows the spring constant decreases with increasing number of bellows (see formula for adding springs in series) and therefore, the transmissibility decreases. This can be seen in A.1(b) with a spring constant of one edge welded bellows of 40 N/mm and a typical damping constant of 0.1.



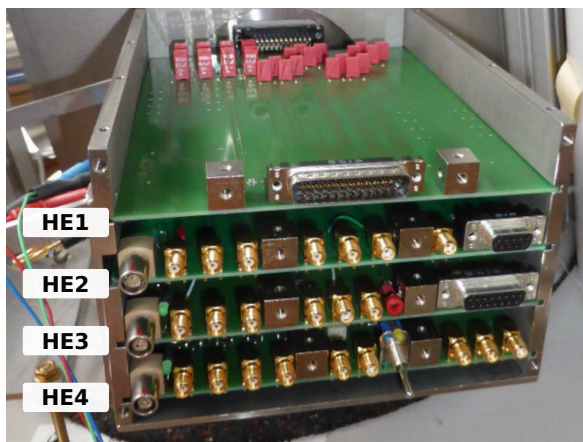
(a)



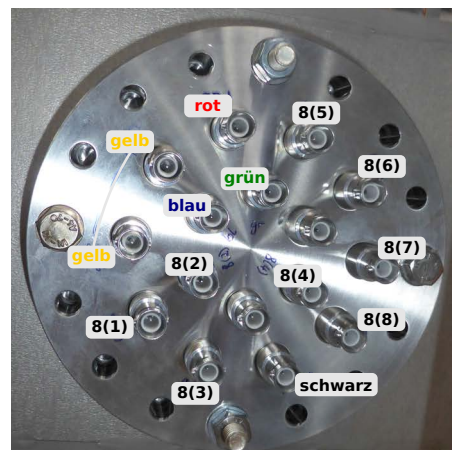
(b)

**Figure A.1:** (a) Transmissibility plotted against the natural frequency of an object. The drive frequency is 1.4 Hz, which is the most prominent value for a typical cryocooler. (b) The transmissibility for edge welded bellows connecting the drive frequency to the object with mass  $m$ . The value of 40 N/mm is taken from the COMVAT website.

## A.2 ARTEMIS Wiring



(a)



(b)

**Figure A.2:** (a) Photograph of the opened housing of the room-temperature filterboards that are directly connected to the D-Sub feedthroughs flange. (b) Photograph with labeling of the HV feedthrough flange.

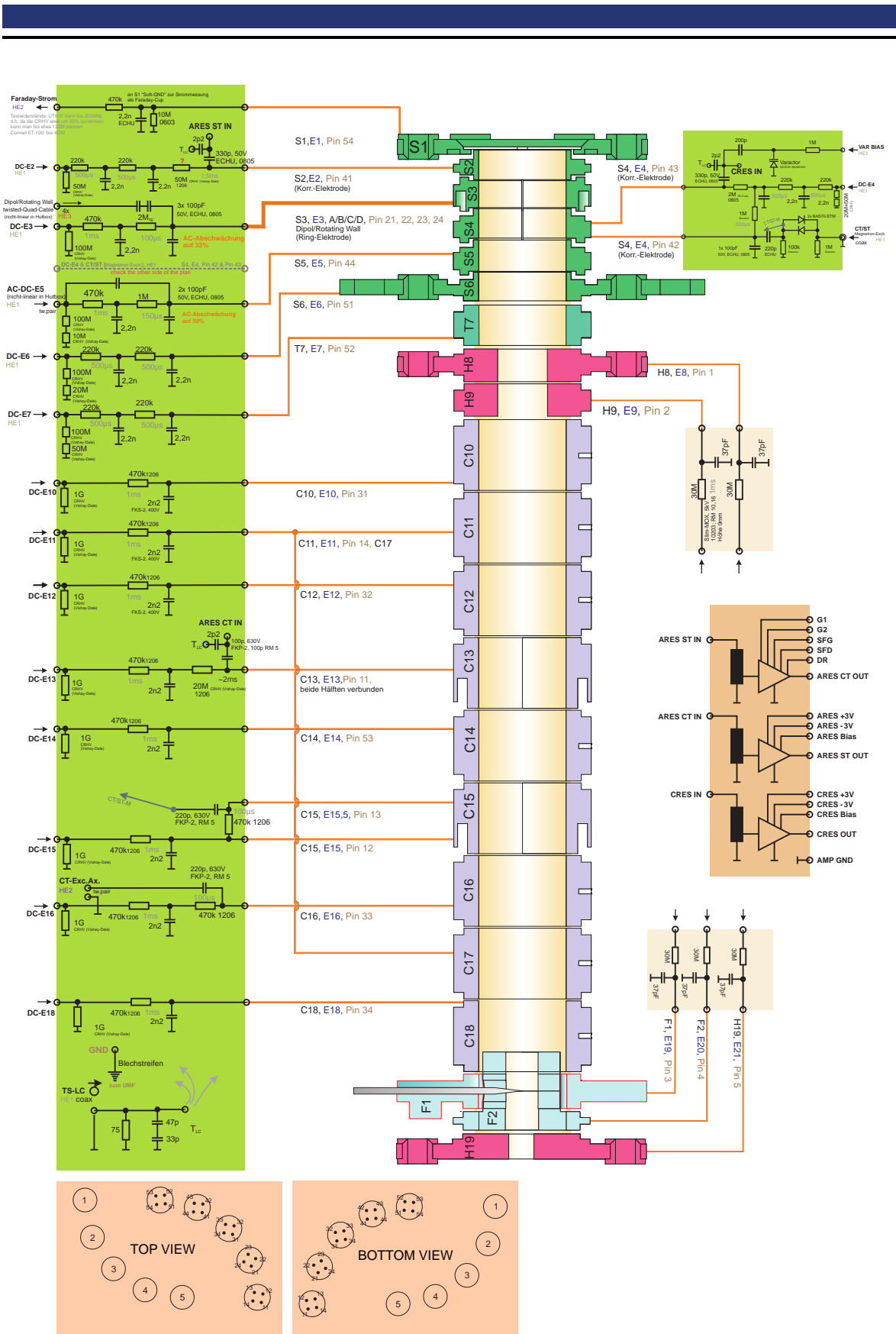


Figure A.3: Updated trap wiring with cryogenic filterboards and UMF wiring.



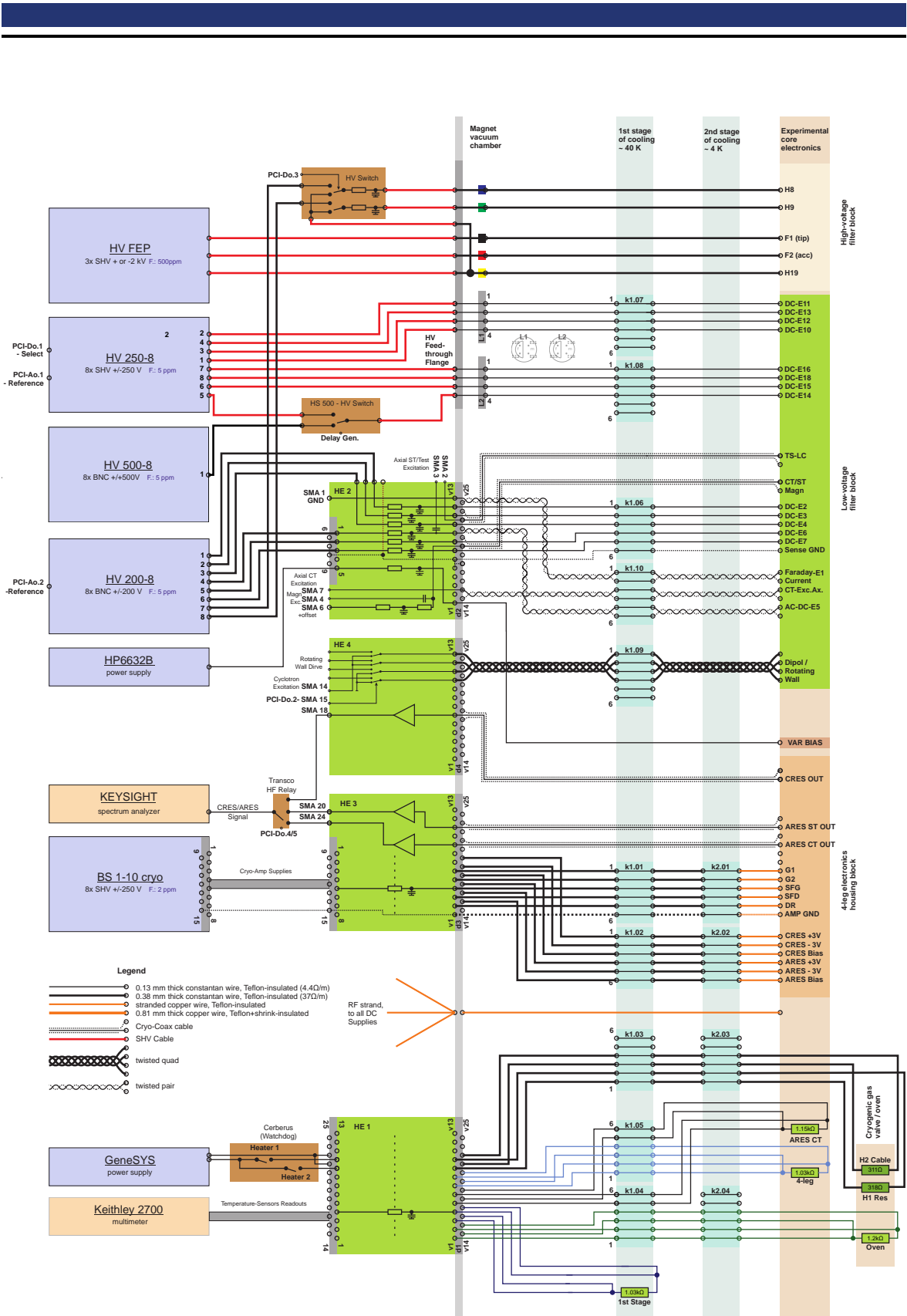
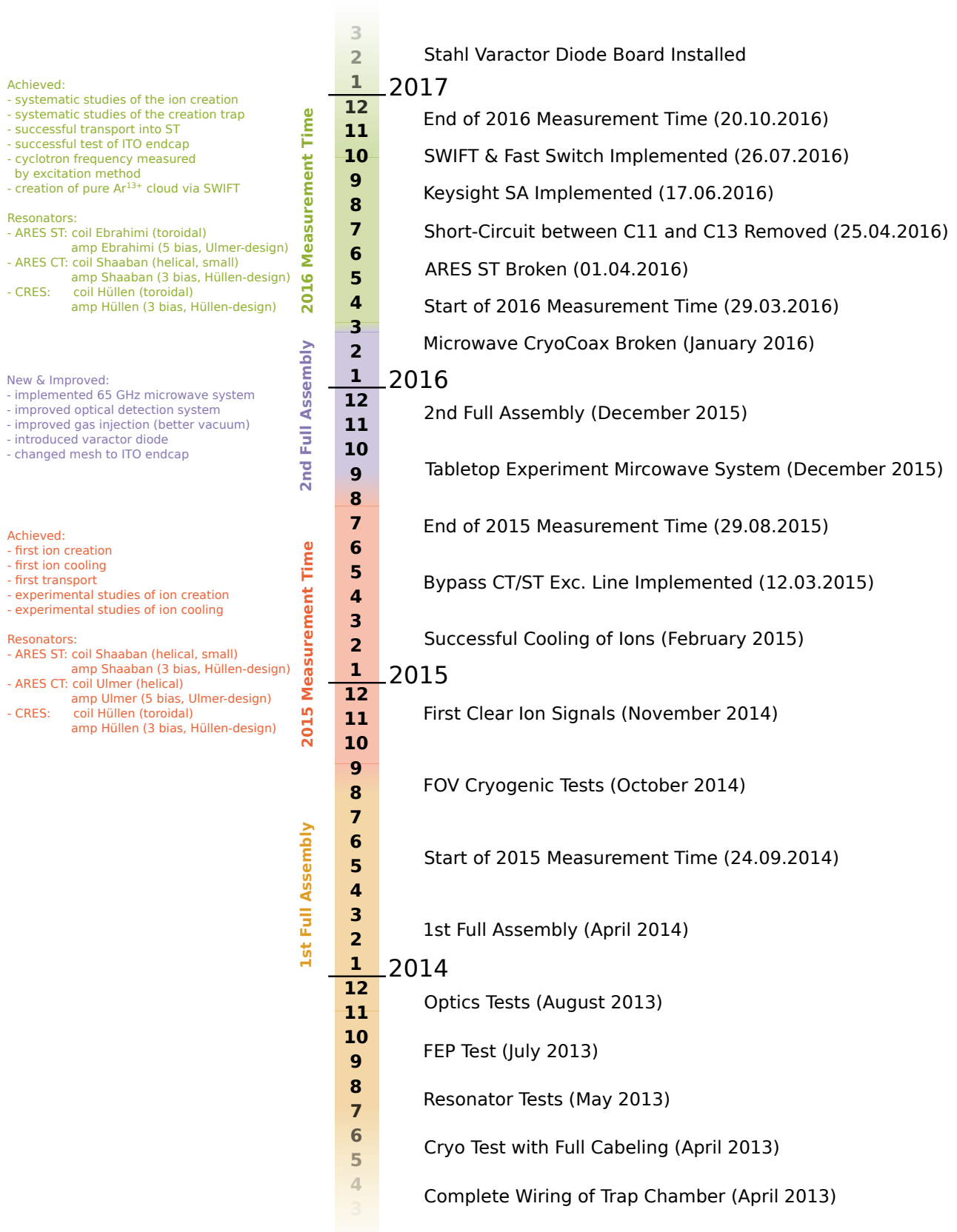


Figure A.4: Updated setup wiring.





## A.3 Timeline of ARTEMIS



---

## B List of Abbreviations

<b>a.u.</b>	arbitrary units
<b>AOM</b>	acousto-optical modulator
<b>AR</b>	anti reflection (coating)
<b>ARES</b>	axial resonator
<b>ARES CT</b>	axial resonator in the creation trap
<b>ARES ST</b>	axial resonator in the spectroscopy trap
<b>ARTEMIS</b>	asymmetric trap for the measurement of electron magnetic moments in ions
<b>BS-QED</b>	bound-state quantum electrodynamics
<b>CAD</b>	computer-aided design
<b>CF</b>	conflat (flange standard)
<b>CPM</b>	channeltron photo-multiplier
<b>CRES</b>	cyclotron resonator
<b>CT</b>	creation trap
<b>D-Sub</b>	D-subminiature (connector)
<b>EBIS</b>	electron beam ion source
<b>EBIT</b>	electron beam ion trap
<b>FEP</b>	field-emission point
<b>FFT</b>	fast Fourier transform
<b>FM</b>	frequency modulation
<b>FOV</b>	fast-opening valve
<b>FS</b>	fine structure
<b>GND</b>	ground
<b>GSI</b>	Gesellschaft für Schwerionenforschung

---

<b>HCI</b>	highly charged ions
<b>HE</b>	Huteinheit = hat unit
<b>HFS</b>	hyperfine structure
<b>HILITE</b>	high intensity laser ion trap experiment
<b>HITRAP</b>	heavy highly charged ion trap
<b>HV</b>	high voltage
<b>ITO</b>	indium tin oxide
<b>LNA</b>	low-noise amplifier
<b>LV</b>	low voltage
<b>MMIC</b>	monolithic microwave integrated circuit
<b>OFHC</b>	oxygen-free high thermal conductivity
<b>PA</b>	power amplifier
<b>PEEK</b>	polyether ether ketone
<b>PTFE</b>	polytetrafluoroethylene ('Teflon')
<b>ppb</b>	parts per billion ( $10^{-9}$ )
<b>ppm</b>	parts per million ( $10^{-6}$ )
<b>QED</b>	quantum electrodynamics
<b>RF</b>	radio frequency
<b>SA</b>	spectrum analyzer
<b>SHV</b>	safe high voltage (connector)
<b>SIS18</b>	Schwerionensynchrotron = heavy ion synchrotron
<b>SMA</b>	subminiature version A (connector)
<b>ST</b>	spectroscopy trap
<b>SWIFT</b>	stored waveform inverse Fourier transform
<b>UNILAC</b>	universal linear accelerator
<b>UMF</b>	Unterer Montageflansch
<b>VSWR</b>	voltage standing wave ratio
<b>YIG</b>	yttrium iron garnet

---

# Bibliography

- [1] P. Kusch and H. M. Foley, *Precision measurement of the ratio of the atomic  $g$  values in the  $^2P_{3/2}$  and  $^2P_{1/2}$  states of gallium*, Phys. Rev. **72** (1947).
- [2] H. M. Foley and P. Kusch, *On the Intrinsic Moment of the Electron*, Phys. Rev. **73**, 412 (1948).
- [3] W. E. Lamb and R. C. Retherford, *Fine Structure of the Hydrogen Atom by a Microwave Method*, Phys. Rev. **72**, 241 (1947).
- [4] F. J. Dyson, *Divergence of Perturbation Theory in Quantum Electrodynamics*, Phys. Rev. **85**, 631 (1952).
- [5] Nobelprize.org, *The official website of the Nobelprize*, <http://www.nobelprize.org/>, 2017.
- [6] R. S. van Dyck, P. B. Schwinberg and H. G. Dehmelt, *Electron magnetic moment from geonium spectra: Early experiments and background concepts*, Phys. Rev. D **34**, 722 (1986).
- [7] D. Hanneke, S. Fogwell Hoogerheide and G. Gabrielse, *Cavity control of a single-electron quantum cyclotron: Measuring the electron magnetic moment*, Phys. Rev. A **83** (2011).
- [8] S. G. Karshenboim, *Precision physics of simple atoms: QED tests, nuclear structure and fundamental constants*, Physics Reports **422**, 1 (2005).
- [9] T. Aoyama, M. Hayakawa, T. Kinoshita and M. Nio, *Tenth-Order QED Contribution to the Electron  $g-2$  and an Improved Value of the Fine Structure Constant*, Phys. Rev. Lett. **109** (2012).
- [10] S. Sturm, F. Köhler, J. Zatorski, A. Wagner, Z. Harman, G. Werth, W. Quint, C. H. Keitel and K. Blaum, *High-precision measurement of the atomic mass of the electron*, Nature **506**, 467 (2014).
- [11] V. M. Shabaev, D. A. Glazov, N. S. Oreshkina, A. V. Volotka, G. Plunien, H. J. Kluge and W. Quint,  *$g$ -Factor of Heavy Ions: A New Access to the Fine Structure Constant*, Phys. Rev. Lett. **96**, 253002 (2006).
- [12] T. Beier, *The  $g_j$  factor of a bound electron and the hyperfine structure splitting in hydrogenlike ions*, Physics Reports **339**, 79 (2000).

- 
- [13] F. Herfurth, Z. Andelkovic, W. Barth, W. Chen, L. A. Dahl, S. Fedotova, P. Gerhard, M. Kaiser, O. K. Kester, H. J. Kluge, N. Kotovskiy, M. Maier, B. Maaß, D. Neidherr, W. Quint, U. Ratzinger, A. Reiter, A. Schempp, T. Stöhlker, H. Vormann, G. Vorobjev and S. Yaramyshev, *The HITRAP facility for slow highly charged ions*, Phys. Scr. **T166**, 014065 (2015).
- [14] R. Soria Orts, J. R. Crespo López-Urrutia, H. Bruhns, A. J. Gonzalez Martinez, Z. Harman, U. D. Jentschura, C. H. Keitel, A. Lapierre, H. Tawara, I. I. Tupitsyn, J. Ullrich and A. V. Volotka, *Zeeman splitting and g factor of the  $1s^2 2s^2 2p^2 P_{3/2}$  and  $^2 P_{1/2}$  levels in  $Ar^{13+}$* , Phys. Rev. A **76**, 052501 (2007).
- [15] D. von Lindenfels, N. P. M. Brantjes, G. Birkl, W. Quint and M. Vogel, *Bound electron g-factor measurement by double-resonance spectroscopy on a fine-structure transition*, Can. J. Phys. **89**, 79 (2011).
- [16] D. von Lindenfels, M. Wiesel, D. A. Glazov, A. V. Volotka, M. M. Sokolov, V. M. Shabaev, G. Plunien, W. Quint, G. Birkl, A. Martin and M. Vogel, *Experimental access to higher-order Zeeman effects by precision spectroscopy of highly charged ions in a Penning trap*, Phys. Rev. A **87**, 023412 (2013).
- [17] W. Quint, D. L. Moskovkhin, V. M. Shabaev and M. Vogel, *Laser-mirowave double-resonance technique for g-factor measurements in highly charged ions*, Phys. Rev. A **78** (2008).
- [18] D. von Lindenfels, *Experimental Studies of Highly Charged Ions in a Penning Trap for the Measurement of Electron Magnetic Moments by Double-Resonance Spectroscopy*, PhD Thesis, Ruprecht-Karls-Universität Heidelberg, (2015).
- [19] R. P. Feynman, *Space-Time Approach to Quantum Electrodynamics*, Phys. Rev. **76**, 769 (1949).
- [20] P. Schmüser, *Feynman - Graphen und Eichtheorien für Experimentalphysiker* (Springer-Verlag GmbH, 1995).
- [21] *Fundamental Physics in Particle Traps*, No. volume 256 in *Springer tracts in modern physics*, W. Quint and M. Vogel, eds., (Springer, Heidelberg; New York, 2014).
- [22] A. V. Volotka, D. A. Glazov, G. Plunien and V. M. Shabaev, *Progress in quantum electrodynamics theory of highly charged ions*, Annalen der Physik **525**, 636 (2013).
- [23] V. M. Shabaev, D. A. Glazov, M. B. Shabaeva, V. A. Yerokhin, G. Plunien and G. Soff, *g-factor of high-Z lithiumlike ions*, Phys. Rev. A **65** (2002).
- [24] A. V. Nefiodov, G. Plunien and G. Soff, *Nuclear-Polarization Correction to the Bound-Electron g Factor in Heavy Hydrogenlike Ions*, Phys. Rev. Lett. **89**, 081802 (2002).

- 
- [25] D. A. Glazov, A. V. Volotka, A. A. Schepetnov, M. M. Sokolov, V. M. Shabaev, I. I. Tupitsyn and G. Plunien, *g factor of boron-like ions: ground and excited states*, Physica Scripta **2013**, 014014 (2013).
- [26] A. A. Shchepetnov, D. A. Glazov, A. V. Volotka, V. M. Shabaev, I. I. Tupitsyn and G. Plunien, *Nuclear recoil correction to the g factor of boron-like argon*, J. Phys. Conf. Ser. **583**, 012001 (2015).
- [27] H. F. Beyer, *Introduction to the Physics of Highly Charged Ions* (Taylor & Francis Ltd, 2002).
- [28] V. Mäckel, R. Klawitter, G. Brenner, J. R. Crespo López-Urrutia and J. Ullrich, *Laser spectroscopy of highly charged argon at the Heidelberg electron beam ion trap*, Phys. Scr. **T156**, 014004 (2013).
- [29] A. Lapiere, U. D. Jentschura, J. R. Crespo López-Urrutia, J. Braun, G. Brenner, H. Bruhns, D. Fischer, A. J. González Martínez, Z. Harman, W. R. Johnson, C. H. Keitel, V. Mironov, C. J. Osborne, G. Sikler, R. Soria Orts, V. M. Shabaev, H. Tawara, I. I. Tupitsyn, J. Ullrich and A. V. Volotka, *Relativistic Electron Correlation, Quantum Electrodynamics, and the Lifetime of the  $1s^2 2s^2 2p^2 P_{3/2}$  Level in Boronlike Argon*, Phys. Rev. Lett. **95** (2005).
- [30] A. Mooser, S. Bräuninger, K. Franke, H. Kracke, C. Leiteritz, C. C. Rodegheri, H. Nagahama, G. Schneider, C. Smorra, K. Blaum, Y. Matsuda, W. Quint, J. Walz, Y. Yamazaki and S. Ulmer, *Demonstration of the double Penning Trap technique with a single proton*, Phys. Lett. B **723**, 78 (2013).
- [31] J. Brossel and F. Bitter, *A New ‘Double Resonance’ Method for Investigating Atomic Energy Levels. Application to  $Hg\ ^3P_1$* , Phys. Rev. **86**, 308 (1952).
- [32] *Laser Spectroscopy of Atoms and Molecules (Topics in Applied Physics)*, H. Walther, ed., (Springer, 1976).
- [33] G. Gabrielse, L. Haarsma and S. L. Rolston, *Open-endcap Penning traps for high precision experiments*, Int. J. Mass Spectrom. Ion Processes **88**, 319 (1989).
- [34] G. Gabrielse and F. Mackintosh, *Cylindrical Penning traps with orthogonalized anharmonicity compensation*, Int. J. Mass Spectrom. Ion Processes **57**, 1 (1984).
- [35] H. Häffner, T. Beier, S. Djekić, N. Hermanspahn, H. J. Kluge, W. Quint, S. Stahl, J. Verdú, T. Valenzuela and G. Werth, *Double Penning trap technique for precise g factor determinations in highly charged ions*, EPJ D **22**, 163 (2003).
- [36] J. Verdú, S. Kreim, K. Blaum, H. Kracke, W. Quint, S. Ulmer and J. Walz, *Calculation of electrostatic fields using quasi-Green’s functions: application to the hybrid Penning trap*, New J. Phys. **10**, 103009 (2008).

- 
- [37] S. Stahl, F. Galve, J. Alonso, S. Djekić, W. Quint, T. Valenzuela, J. Verdú, M. Vogel and G. Werth, *A planar Penning trap*, EPJ D **32**, 139 (2005).
- [38] J. Goldman and G. Gabrielse, *Optimized planar Penning traps for quantum-information studies*, Phys. Rev. A **81**, 052335 (2010).
- [39] G. Werth, V. N. Gheorghe and F. G. Major, *Charged Particle Traps II* (Springer Berlin Heidelberg, 2009).
- [40] L. S. Brown and G. Gabrielse, *Precision spectroscopy of a charged particle in an imperfect Penning trap*, Phys. Rev. A **25**, 2423 (1982).
- [41] W. Nolting, *Grundkurs Theoretische Physik 6: Statistische Physik* (Springer, 2007).
- [42] G. J. Ketter, *Theoretical treatment of miscellaneous frequency-shifts in Penning traps with classical perturbation theory*, PhD Thesis, Ruprecht-Karls-Universität Heidelberg, (2015).
- [43] M. Vogel, W. Quint and W. Nörtershäuser, *Trapped Ion Oscillation Frequencies as Sensors for Spectroscopy*, Sensors **10**, 2169 (2010).
- [44] J. Yu, M. Desaintfuscien and F. Plumelle, *Ion density limitation in a Penning trap due to the combined effect of asymmetry and space charge*, Appl. Phys. B **48**, 51 (1989).
- [45] S. Bharadia, M. Vogel, D. M. Segal and R. C. Thompson, *Dynamics of laser-cooled Ca<sup>+</sup> ions in a Penning trap with a rotating wall*, Appl. Phys. B **107**, 1105 (2012).
- [46] L. S. Brown and G. Gabrielse, *Physics of a single electron or ion in a Penning trap*, Rev. Mod. Phys. **58** (1986).
- [47] S. Ulmer, *First Observation of Spin Flips with a Single Proton Stored in a Cryogenic Penning Trap*, PhD Thesis, Ruprecht-Karls-Universität Heidelberg, (2011).
- [48] D. J. Wineland and H. G. Dehmelt, *Principles of the stored ion calorimeter*, J. Appl. Phys. **46**, 919 (1975).
- [49] S. Stahl, *Aufbau eines Experiments zur Bestimmung elektronischer g-Faktoren einzelner wasserstoffähnlicher Ionen*, PhD Thesis, Johannes Gutenberg-Universität Mainz, (1998).
- [50] A. Martin, *Laser Spectroscopy Investigations of Exotic States in Noble Gases*, PhD Thesis, Technische Universität Darmstadt, (2017).
- [51] D. von Lindenfels, *Development of an Ion Trap Experiment for the Measurement of the Electron Magnetic Moment by Double-Resonance Spectroscopy*, Diploma Thesis, Ruprecht-Karls-Universität Heidelberg, (2010).



- 
- [52] M. Wiesel, *Cryotechnical Setup of ARTEMIS - an Experiment for Precision Spectroscopy on Highly Charged Ions in a Penning Trap*, Diploma Thesis, Ruprecht-Karls-Universität Heidelberg, (2012).
- [53] T. Gassner, *High Precision X-Ray Spectroscopy of Highly Charged Heavy Ions*, PhD Thesis, Friedrich-Schiller-Universität Jena, (2016).
- [54] C. Vogel, *Aufbau und Charakterisierung eines Kaltventils fuer Penning-Fallen Experimente*, Bachelor Thesis, Technische Universität Darmstadt, (2014).
- [55] J. Ekin, *Experimental Techniques for Low Temperature Measurements* (Oxford University Press, 2006).
- [56] RUAG, *Coolcat 2 Datasheet*, <https://www.ruag.com/>, 2017.
- [57] Stahl Electronics, *Electronic Solutions for Science and Research*, <http://www.stahl-electronics.com/>, 2017.
- [58] H. Nagahama, G. Schneider, A. Mooser, C. Smorra, S. Sellner, J. Harrington, T. Higuchi, M. Borchert, T. Tanaka, M. Besirli, K. Blaum, Y. Matsuda, C. Ospelkaus, W. Quint, J. Walz, Y. Yamazaki and S. Ulmer, *Highly sensitive superconducting circuits at 700 kHz with tunable quality factors for image-current detection of single trapped antiprotons*, Rev. Sci. Instrum. **87**, 113305 (2016).
- [59] M. S. Ebrahimi, N. Stallkamp, W. Quint, M. Wiesel, M. Vogel, A. Martin and G. Birkl, *Superconducting radio-frequency resonator in magnetic fields up to 6 T*, Rev. Sci. Instrum. **87**, 075110 (2016).
- [60] M. Hüllen, *Entwicklung und Test eines elektronischen Nachweissystems für hoch geladene Ionen in einer Penning-Falle*, Bachelor Thesis, Hochschule Karlsruhe, (2011).
- [61] S. Ringleb, M. Vogel, S. Kumar, W. Quint, G. G. Paulus and T. Stöhlker, *HILITE-ions in intense photon fields*, Phys. Scr. **2015**, 014067 (2015).
- [62] N. P. M. Brantjes, *The g-Factor of Hydrogen-Like Heavy Ions as a Test for QED*, PhD Thesis, Ruprecht-Karls-Universität Heidelberg, (2012).
- [63] P. Horowitz and W. Hill, *The Art of Electronics* (Cambridge University Press, New York, NY, USA, 1989).
- [64] E. Hering, K. Bressler and J. Gutekunst, *Elektronik für Ingenieure und Naturwissenschaftler* (Springer Berlin Heidelberg, 2014).
- [65] MACOM, *MA46H202-Datasheet*, <https://www.macom.com/products/product-detail/MA46H202-1056>, 2017.
- [66] P. Baus, *Characterization of a Wide Tunable, Robust, Multi Application Diode Laser for Spectroscopy*, Master Thesis, Technische Universität Darmstadt, (2014).

- 
- [67] S. Albrecht, S. Altenburg, C. Siegel, N. Herschbach and G. Birkel, *A Laser System for the Spectroscopy of Highly Charged Bismuth Ions*, Appl. Phys. B (2011).
- [68] *Giga-tronics GT9000 Microwave Synthesizer*, 1998.
- [69] Agilent Technologies, *Solutions for Reducing Phase Noise at RF and Microwave Frequencies*, <http://cp.literature.agilent.com/litweb/pdf/5990-7529EN.pdf>, 2016.
- [70] W. Demtröder, *Elektrizität und Optik* (Springer, 2006).
- [71] D. M. Pozar, *Microwave Engineering*, 4th ed. (Wiley, Hoboken, NJ, 2005).
- [72] Flann Microwave Ltd., *FMI Catalogue*, <http://www.flann.com>, 2015.
- [73] M. Tönges, *Aufbau einer Mikrowellen-Anlage zur Spektroskopie an wasserstoff-fähnlichen Ionen in einem Penningkäfig*, Diploma Thesis, Johannes Gutenberg-Universität Mainz, (1996).
- [74] SHF Communication Technologies AG, *Datasheet Cryo Cables*, <https://www.shf.de/products/rf-connectors-adapters-cables/>, 2017.
- [75] G. A. Ediss, N. Horner, F. Johnson, D. Koller and A. R. Kerr, *WR-10 Waveguide Vacuum Feedthrough for the ALMA Band-6 Cartridge*, Technical report, National Radio Astronomy Observatory (2005) .
- [76] D. J. Hucknall, *Vacuum Technology and Applications* (Elsevier Science, 2013).
- [77] D. K. Linkhart, *Microwave Circulator Design* (Artech House Publishers, 2014).
- [78] SAGE Millimeter Inc., *Datasheet: WR-15 Pyramidal Horn Antenna, 25 dBi Gain*, <http://www.sagemillimeter.com/pyramidal-horn-antennas>, 2017.
- [79] D. von Lindenfels, M. Vogel, W. Quint, G. Birkel and M. Wiesel, *Half-open Penning trap with efficient light collection for precision laser spectroscopy of highly charged ions*, Hyperfine Interact. **227**, 197 (2014).
- [80] R. L. Weiher and R. P. Ley, *Optical Properties of Indium Oxide*, J. Appl. Phys. **37**, 299 (1966).
- [81] R. Groth, *Untersuchungen an halbleitenden Indiumoxydschichten*, Phys. Stat. Sol. **14**, 69 (1966).
- [82] M. Mizuhashi, *Electrical Properties of Vacuum-deposited Indium Oxide and Indium Tin Oxide Films*, Thin Solid Films **70**, 91 (1980).
- [83] R. Bel Hadj Tahar, T. Ban, Y. Ohya and Y. Takahashi, *Tin doped indium oxide thin films: Electrical properties*, J. Appl. Phys. **83**, 2631 (1998).

- 
- [84] A. M. Eltony, S. X. Wang, G. M. Akselrod, P. F. Herskind and I. L. Chuang, *Transparent ion trap with integrated photodetector*, Appl. Phys. Lett. **102**, 054106 (2013).
- [85] Thorlabs, *WTSQ11050-A Datasheet*, <https://www.thorlabs.de/>, 2017.
- [86] J. G. Webster and H. Eren, *Measurement, Instrumentation, and Sensors Handbook, Second Edition* (CRC Press, 2014).
- [87] B.-T. Lin, Y.-F. Chen, J.-J. Lin and C.-Y. Wu, *Temperature dependence of resistance and thermopower of thin indium tin oxide films*, Thin Solid Films **518**, 6997 (2010).
- [88] H. J. Kluge, T. Beier, K. Blaum, L. A. Dahl, S. Eliseev, F. Herfurth, B. Hofmann, O. K. Kester, S. Koszudowski and C. Kozhuharov, *HITRAP: A facility at GSI for highly charged ions.*, Adv. Quantum Chem., **53**, 83-98. (2007).
- [89] Z. Andelkovic, F. Herfurth, N. Kotovski, K. König, B. Maaß, T. Murböck, D. Neidherr, S. Schmidt, J. Steinmann, M. Vogel and G. Vorobjev, *Beamline for low-energy transport of highly charged ions at HITRAP*, Nucl. Instrum. Methods Phys. Res., Sect. A **795**, 109 (2015).
- [90] K. König, *Inbetriebnahme der Niederenergiestrecke bei HITRAP und erstmaliger Einfang hochgeladener Ionen in der SpecTrap Penningfalle*, Master Thesis, Technische Universität Darmstadt, (2014).
- [91] C. Vogel, *Design of the beamline for ARTEMIS*, Master Thesis, Technische Universität Darmstadt, (2016).
- [92] P. Beiersdorfer, A. Osterheld, S. R. Elliott, M. H. Chen, D. Knapp and K. Reed, *Structure and Lamb shift of  $2s_{1/2}$ - $2p_{3/2}$  levels in lithiumlike  $\text{Th}^{87+}$  through neonlike  $\text{Th}^{80+}$* , Phys. Rev. A **52**, 2693 (1995).
- [93] *CRC Handbook of Chemistry and Physics, 84th Edition* (CRC Press, 2003).
- [94] R. Becker, O. K. Kester and T. Stöhlker, *Simulation of Charge Breeding for Trapped Ions*, HCI (2006).
- [95] A. E. Kramida and J. Reader, *Ionization energies of tungsten ions:  $\text{W}^{2+}$  through  $\text{W}^{71+}$* , At. Data Nucl. Data Tables **92**, 457 (2006).
- [96] T. Murböck, *Preparation and cooling of magnesium ion crystals for sympathetic cooling of highly charged ions in a Penning trap*, PhD Thesis, Technische Universität Darmstadt, (2016).
- [97] J. Steinmann, *Modellierung und Simulation der Widerstandskühlung von hochgeladenen Ionen*, PhD Thesis, Universität Erlangen-Nürnberg, (2016).

- 
- [98] M. Vogel, H. Häffner, K. Hermanspahn, S. Stahl, J. Steinmann and W. Quint, *Resistive and sympathetic cooling of highly-charged-ion clouds in a Penning trap*, Phys. Rev. A **90** (2014).
- [99] D. J. Wineland and H. G. Dehmelt, *Line shifts and widths of axial, cyclotron and g-2 resonances in tailored, stored electron (ion) cloud*, Int. J. Mass Spectrom. Ion Phys. **16**, 338 (1975).
- [100] S. Bliman, S. Dousson, B. Jacquot and D. Van Houtte, *Charge exchange cross sections of argon ions colliding with rare gas targets at keV energies*, Journal de Physique **42**, 1387 (1981).
- [101] M. Kiffer, *Selektive Breitbandanregung von Ionen in einer Penningfalle*, Bachelor Thesis, Friedrich-Schiller-Universität Jena, (2016).
- [102] E. O. Brigham, *The Fast Fourier Transform: An Introduction to Its Theory and Application* (Prentice Hall, 1973).
- [103] T. Murböck, S. Schmidt, G. Birkl, W. Nörtershäuser, R. C. Thompson and M. Vogel, *Rapid crystallization of externally produced ions in a Penning trap*, Phys. Rev. A **94**, 043410 (2016).

---

# Curriculum Vitae

---

## Personal Details

Name **Marco Wiesel**  
Date of Birth **28.03.1987 in Neustadt a.d. Weinstraße**  
Nationality **German**

## Education

- 10/2012- **Ph.D. Thesis**, *Technische Universität Darmstadt*, Darmstadt  
05/2017 Supervisor: Prof. Dr. Gerhard Birkel,  
»Preparation and Investigation of Highly Charged Ions in a Penning Trap for the Determination of Atomic Magnetic Moments«.  
Conducted at the GSI Helmholtzzentrum für Schwerionenforschung, Darmstadt
- 09/2012 **Physics Diploma.**
- 09/2011- **Diploma Thesis**, *Ruprecht-Karls-Universität Heidelberg*, Heidelberg  
09/2012 Supervisor: PD Dr. Wolfgang Quint,  
»Cryotechnical Setup of ARTEMIS - an Experiment for Precision Spectroscopy on Highly Charged Ions in a Penning Trap«.  
Conducted at GSI Helmholtzzentrum für Schwerionenforschung, Darmstadt
- 10/2006- **Physic Studies**, *Ruprecht-Karls-Universität Heidelberg*, Heidelberg.  
09/2012 Elective: atomic and molecular physics
- 2006 **Allgemeine Hochschulreife (Abitur)**, *Käthe-Kollwitz-Gymnasium*, Neustadt a.d. Weinstraße.
- 1997-2006 **Gymnasium**, *Käthe-Kollwitz-Gymnasium*, Neustadt a.d. Weinstraße.

## Research Internships

- 06-09/2014 **Visiting Researcher**, *Harvard University*, Cambridge, MA.  
»Design of a vibration decoupling stage for a dilution refrigerator of the free electron magnetic moment experiment«
- 03/2009 **Miniforschung**, *GSI Helmholtzzentrum für Schwerionenforschung*, Darmstadt.  
»Microwave Intensity Distribution in Ion Traps«

Darmstadt, 18.04.2017

Marco Wiesel



---

# List of Publications

Some of the research leading to this thesis has appeared previously in the following publications.

---

## Publications in Peer-Reviewed Journals

---

- M.S. Ebrahimi, N. Stallkamp, W. Quint, M. Wiesel, M. Vogel, A. Martin, and G. Birkl  
*Superconducting radio-frequency resonator in magnetic fields up to 6 T*, Review of Scientific Instruments, **87**, 075110 (2016)
- M. Vogel, G. Birkl, W. Quint, D. von Lindenfels, and M. Wiesel  
*Switchable magnetic bottles and field gradients for particle traps*, Applied Physics B, **114**, 63–74 (2014)
- D. von Lindenfels, M. Wiesel, D.A. Glazov, A.V. Volotka, M.M. Sokolov, V.M. Shabaev, G. Plunien, W. Quint, G. Birkl, A. Martin, and M. Vogel  
*Experimental access to higher-order Zeeman effects by precision spectroscopy of highly charged ions in a Penning trap*, Physical Review A, **87**, 023412 (2013)

---

## Conference Proceedings

---

- M. Vogel, G. Birkl, M.S. Ebrahimi, D. von Lindenfels, A. Martin, G.G. Paulus, W. Quint, S. Ringleb, Th. Stöhlker, and M. Wiesel  
*Extreme-field physics in Penning traps: The ARTEMIS and HILITE experiments*, Hyperfine Interactions, **236**, 65–71 (2015)
- M. Vogel, Z. Andelkovic, G. Birkl, M.S. Ebrahimi, V. Hannen, D. von Lindenfels, A. Martin, T. Murböck, W. Nörtershäuser, W. Quint, S. Schmidt, D.M. Segal, R.C. Thompson, J. Vollbrecht, Ch. Weinheimer, and M. Wiesel  
*Penning-trap experiments for spectroscopy of highly-charged ions at HITRAP*, Physica Scripta, **T166**, 014066 (2015)
- D. von Lindenfels, M. Vogel, W. Quint, G. Birkl, and M. Wiesel  
*Half-open Penning trap with efficient light collection for precision laser spectroscopy of highly charged ions*, Hyperfine Interactions, **227**, 197—207 (2014)





---

# Danksagung

Die vergangenen Jahre waren eine spannende und abwechslungsreiche Zeit, mit vielen Erfolgen und Herausforderungen, sie waren eine Zeit in der ich viel lernen und erleben durfte. Viele Menschen haben mich dabei unterstützt, dafür möchte ich meinen Dank aussprechen.

In erster Linie möchte ich meinem Betreuer Herrn Prof. Dr. Gerhard Birkl für die Möglichkeit danken, meine Arbeit am ARTEMIS Projekt fortzusetzen. In abwechslungsreichen Diskussionen haben Sie mit Ihren gezielten Nachfragen das eigene Verständnis immer kritisch hinterfragt und so neue Gedankengänge angestoßen.

Ein großer Teil meines Dankes gilt Herrn PD Dr. Wolfgang Quint, der mich mit seiner Begeisterung und seinem wissenschaftlichen Interesse nicht nur in die Welt der Hochpräzisionsmessungen eingeführt hat, sondern mir auf dem Weg hierher auch so vieles ermöglicht hat. Danke Wolfgang, dass Deine Tür immer offen steht für spannende wissenschaftliche Diskussionen oder auch Fragen persönlicher Art.

Des Weiteren danke ich Dr. Manuel Vogel für seinen Einsatz für ARTEMIS in theoretischer, praktischer und organisatorischer Weise. Vielen Dank auch für Deine anregenden Gespräche über die Wissenschaft und darüber hinaus.

Prof. Dr. Thomas Stöhlker und Prof. Dr. Klaus Blaum danke ich für Ihren Einsatz für ARTEMIS.

I want to thank Professor Gerald Gabrielse for giving me the opportunity to work in his group on the most precise experiment in physics. During my time at Harvard University I learned from you how to systematically challenge the own knowledge in order to perform more targeted experiments.

Dr. David von Lindenfels, Sadegh Ebrahimi, Alexander Martin, Zhexi Guo und Dr. Klaas Brantjes danke ich für die vorausgehende, gemeinsame und zukünftige Arbeit, die sie an ARTEMIS geleistet haben und leisten werden. Ich freue mich auf weitere tolle Ergebnisse!

Christian Vogel, Rubain Sateu, Mouwafak Shaaban, Patrick Baus, Florian Vollrath, Stefan Ringleb, Markus Kiffer und Dr. Wolfgang Schott danke ich für die vielen kleineren und größeren Projekte, die alle den Aufbau und die Durchführung von Experimenten an ARTEMIS unterstützt haben.

---

---

Mein Dank gilt auch der Mittagessensgruppe, die sich zwar trotz einiger Konstanten über die Jahre stets verändert hat, aber welche ich hoffentlich bei vielen Gelegenheiten wieder treffen werde: Dr. Benjamin Botermann, Dr. Rodolfo Sánchez, Dr. Zoran Anđelković, Dr. Matthias Lochmann, Dr. Tobias Murböck und Dr. Stefan Schmidt.

Dr. Gerhard Baur und Dr. Sascha Vogel danke ich für die Organisation und ihren Einsatz in den zahlreichen Weiterbildungsmöglichkeiten der Helmholtz Graduate School for Hadron and Ion Research (HGS-HIRE).

I want to thank the various collaborators and friends around the world: Dr. Stefan Ulmer, Dr. K.T. Sathyajith, and especially Sugam Kumar from the HILITE experiment, for the active exchange in expertise. Additionally, I want to thank the St. Petersburg group around Prof. Dr. Vladimir Shabaev for their theoretical work and especially Dr. Dmitry Glazov for his thoughtful discussions over the years.

Many thanks to the colleagues from Harvard University, especially Maryrose Barrios, Ronald Alexander, Elise Novitski, and Cris Panda. I want to thank you for the nice and interesting time we spent together.

Ein ganz besonderer Dank gilt Dr. Stefan Stahl von STAHL ELECTRONICS, der sich über alle Maßen der Kundenbetreuung mit unermüdlichem Einsatz immer wieder bei ARTEMIS eingebracht hat.

In einer Großforschungseinrichtung wie der GSI geht nichts ohne eine gute Zusammenarbeit zwischen den einzelnen Abteilungen. Die Arbeitsatmosphäre ist immer sehr freundlich und man hilft sich gerne. Daher danke ich vielen Mitarbeiterinnen und Mitarbeitern. Besonderer Dank gilt überdies: Herrn Müller und Herrn Kammer von der Technologiewerkstatt, Herrn Romig und seinen Mitarbeitern von der Mechanischen Werkstatt, Claus Schröder von der Kryophysik, Harald Hahn von der Elektronik und Davide Racarno.

Dr. Tobias Gaßner und Nils Stallkamp danke ich für das Korrekturlesen dieser Arbeit, die tiefe Freundschaft und die schöne Zeit an der GSI, bei Konferenzen und in der Freizeit.

Ich danke meinem besten Freund Ralf König, der mir seit der Schulzeit immer Kraft und Selbstbewusstsein gab. Ralf, leider wurdest Du so kurz vor Vollendung dieser Arbeit so schrecklich aus meinem Leben gerissen. Ich danke Dir so sehr für die schöne gemeinsame Zeit!

Mein allergrößter Dank gilt überdies meinen Eltern, Uta und Peter, die mir das Studium ermöglicht haben und mich zusammen mit meiner Schwester Jasmin immer über alle Maßen unterstützen. Zudem danke ich meiner Freundin Valesca: Danke für Deine liebevolle Art und dass Du immer an meiner Seite bist.

---

# Erklärung zur Dissertation

Hiermit versichere ich, die vorliegende Dissertation ohne Hilfe Dritter nur mit den angegebenen Quellen und Hilfsmitteln angefertigt zu haben. Alle Stellen, die aus Quellen entnommen wurden, sind als solche kenntlich gemacht. Diese Arbeit hat in gleicher oder ähnlicher Form noch keiner Prüfungsbehörde vorgelegen.

Darmstadt, den June 8, 2017

---

(Marco Wiesel)